DEVELOPMENT OF A 6-DEGREE-OF-FREEDOM MAGNETICALLY

LEVITATED INSTRUMENT WITH NANOMETER PRECISION

A Thesis

by

JIE GU

Submitted to the Office of Graduate Studies of
Texas A&M University
in partial fulfillment of the requirements for the degree of

MASTER OF SCIENCE

May 2003

Major Subject: Mechanical Engineering

DEVELOPMENT OF A 6-DEGREE-OF-FREEDOM MAGNETICALLY

LEVITATED INSTRUMENT WITH NANOMETER PRECISION

A Thesis

by

JIE GU

Submitted to Texas A&M University
in partial fulfillment of the requirements
for the degree of

MASTER OF SCIENCE

Approved as to style and content by:

Won-jong Kim	Suhada Jayasuriya
(Chair of Committee)	(Member)
Andrew K. Chan	John Weese
(Member)	(Interim Head of Department)

May 2003

Major Subject: Mechanical Engineering

ABSTRACT

Development of a 6-Degree-of-Freedom Magnetically Levitated Instrument with
Nanometer Precision. (May 2003)

Jie Gu,

B.E., Tsinghua University, Beijing, China

Chair of Advisory Committee: Dr. Won-jong Kim

This thesis presents the design and fabrication of a novel magnetically levitated (maglev) device with 6-degree-of-freedom motion capability at nanometer precision. The applications of this device are manufacture of nanoscale structures, assembly of microparts, vibration isolation of delicate instrumentation, and telerobotics. In this thesis, a single-moving stage is levitated by six maglev actuators. The total mass of the moving stage is 0.2126 kg. Three laser interferometers and three capacitance sensors are used to gather the position information. User interface and real-time control routines are implemented digitally on a VME PC and a digital-signal-processor (DSP) board. The underlying mechanical design and fabrication, electrical system setup, control system design, noise analysis, and test results are presented in this thesis. Test results show a quick step response in all six axes and a resolution of 2.5 nm rms in horizontal motion and 25 nm rms in vertical motion.

To my father and mother.

ACKNOWLEDGEMENTS

TABLE OF CONTENTS

LIST OF FIGURES

FIGURE   Page

LIST OF TABLES

CHAPTER I

INTRODUCTION

1.1 Nanotechnology and Nanomanipulation

Nanotechnology has become one of the most popular technical fields in the last decade. It is defined as the fabrication of functional materials, devices and systems through control of matter at the scale of 1 to 100 nanometers, and exploitation of novel properties and phenomena at the same scale [1]. For example, in engineering, items are constructed with materials that could have microscopic flaws, which can affect the structural or operational integrity of a system. By using nanotechnology, material flaws would be eliminated because the construction of materials is monitored atom by atom and the chemical process could be completely controlled. The basic research in nanotechnology can be classified as learning the special properties of materials or devices at nanometer scale and building the device which can harness the advantages of nanoscale dimension and the particular properties in this size.

One key challenge area in nanotechnology is nanomanipulation. Nanomanipulation enables to control and fabricate nanoscale objects in high precision. The nanomanipulation system must be actuated to load, position, and orient nanoscale objects. Significant requirements for the actuators in nanomanipulation include accuracy, range of motion, degrees of freedom, bandwidth [2]. However, research in nanomanipulation is immature with both theoretical and practical problems to be solved. For example, the dynamic behavier of nanoparticles has not been completely understood, intelligent automatic precision manipulation strategies are not well

---

This thesis follows the style and format of *IEEE Transactions on Automatic Control.*

developed, and the specific tools for the specific applications need to be defined clearly [3].

The most widely used manipulation systems are scanning tunneling microscopes (STMs) and atomic force microscopes (AFMs). The STM has also become a common interface for many manipulation systems [4–6]. Nanoparticles and nanorods can be reliably positioned on a surface by pushing them using the tip of an AFM. However, the typical travel range of STMs and AFMs is only on the order of 100 μm, and the motion is limited in the x-y plane. Also there are many sources of uncertainty to influence the performance of an AFM. (1) The accuracy is greatly influenced by thermal drift of the tip under different temperature; (2) The hysteresis from piezoelectric actuators reduces the repeatability of measurement; (3) A large voltage step can produce a rapid displacement of the tip followed by a slow creeping motion which may input a significant positioning error [7].

On the other hand, self-assembly is a possible solution for nanomanipulation. It is basically the same way that life has developed. Self-assembly is a bottom-up approach which is different from the conventional up-bottom approach used in photolithography and micromachining. Self-assembly will be important for some of the building blocks, but it seems unlikely that we could get interesting structures, such as bearings, from self-assembly [8].

Some different kinds of nanomanipulation systems were developed by other researchers. For example, a high-speed precision stage system with 0.69-nm resolution was made by Egshira, *et al.* by using a non-resonant type ultrasonic motor [9]. However, a downside of this system is that it can only realize one-axis movement. An integrated-circuit (IC) probe stage with 10-nm resolution in 6-axis motion was built by Heason Technology Group [10]. However, its travel range with this resolution is only 40 μm. As a summary, a new-generation nanomanipulation system should be developed to meet the ever-increasing demanding specifications in large travel range and multi-axis motion generation.

1.2 Magnetic Levitation Technology

Magnetic levitation (maglev) technology has been successfully implemented for many applications, such as high-speed train suspension, vibration isolation systems, magnetic bearings, rocket-guiding projects, superconductor rotor suspension of gyroscopes, and high-precision positioning stages. Magnetic levitation refers to support and propulsion of objects or vehicles by the use of magnetic field generated by permanent magnets or electromagnets. The magnets provide support without contact or friction, allowing for fast, quiet operation [11].

There are three basic types of maglev technology: (1) permanent-magnet suspension in either the attractive or the repulsive mode; (2) the electrodynamic system (EDS) which relies on the relative motion between high-field (usually superconducting) magnets on the vehicle and a normal conducting metal on the guideway to generate the repulsion levitation forces; (3) the electromagnetic attraction system (EMS) which relies on feedback control to maintain the position of the vehicle or objects [12]. The electromagnetic attraction system has the advantages of levitation at all speeds from standstill, low power consumption, and fit with conventional engineering technology. In contrast to the electromagnetic controlled levitation, the electrodynamic system makes possible a stable and resilient suspension analogous to a magnetic spring. Within these two systems are a variety of design choices and technologies. For example, which type of magnet is used—superconductive, permanent, or resistive; which control system determines and monitors the levitation and propulsive forces; and how those propulsive forces are achieved along the guideway. As cases of the current development of maglev transportation, Germany is using an EMS system and Japan is using superconductive EDS [13].

Advantages of maglev technology include: (1) Since there is no friction, no surface bearings and lubricant are needed to the operation of the system. As a result, the fabrication cost can be significantly reduced. Without friction, the dynamic model of the system is simple and eventually the system repeatability and reliability can be improved.

(2) The complexity of the mechanical structure can be much smaller than the conventional multi-axis manipulation system because one single maglev moving part can easily realize 6-axis motion so that no additional linkage is needed. This structural simplicity of a maglev system increases the system natural frequency. The small inertia leads to the reduction of power consumption. Also without joined parts, position errors are not accumulated. (3) Since no lubricants are required and no wear particles are generated, it is suited for the operation in a clean-room or vacuum environment which is required in the IC industry.

The maglev technology has been successfully applied in precision motion control. Hajjaji, *et al.* built a nonlinear control model for long-range movement of a maglev system and tested it by real-time control implementation [14]. Hollis and Salcudean have demonstrated the applicability of maglev instruments in teleoperation, haptic interface devices, and vibration isolation [15]. A six-degree-of-freedom (6-DOF) planar maglev stage with large planar motion capability was built and demonstrated by Kim with 5-nm rms positioning noise and 100-Hz control bandwidth [16, 17]. Shan, et al. applied robust nonlinear control to their multiple-DOF magnetic suspension stage and demonstrated its nanopositioning capability [18]. Instead of floating in the air, Holmes floated his stage in oil. He developed a long-range scanning stage and achieved subnanometer position resolution at the expense of bandwidth [19, 20].

There are inherent technical challenges in any maglev positioning stages. (1) According to Earnshaw theorem, stable levitation or suspension is impossible for a body placed in a repulsive or attractive static force field in which force and distance are related by inverse square law [21]. Therefore, a fine feedback controller need to be applied to stabilize the levitation of the system. (2) A high speed dignital-signal-processor (DSP) is required to complete real-time control of multi-axis motions. However, with the rapid development of computer science and modern control theory, these problems are no longer critical to us.

1.3 Proposed 6-DOF Maglev Device

The research objective of this thesis is to develop a 6-DOF maglev device which can achieve nanopositioning capability. This research is based on Dr. Won-jong Kim's NSF project and pending US patents [22,23]. The design was conceptualized by Dr. Won-jong Kim. Figure 1-1 shows the prototype of this maglev device. Six actuators are placed on the sides and bottom of the moving stage. They can generate desired forces for 6-axis motion. Two kinds of sensors, capacitance sensors and laser interferometers are used to gather the position information of the moving stage. A DSP takes care of real-time control. Besides the advantages of common magnetic levitation stages, some other advantages of this novel maglev device includes: (1) single
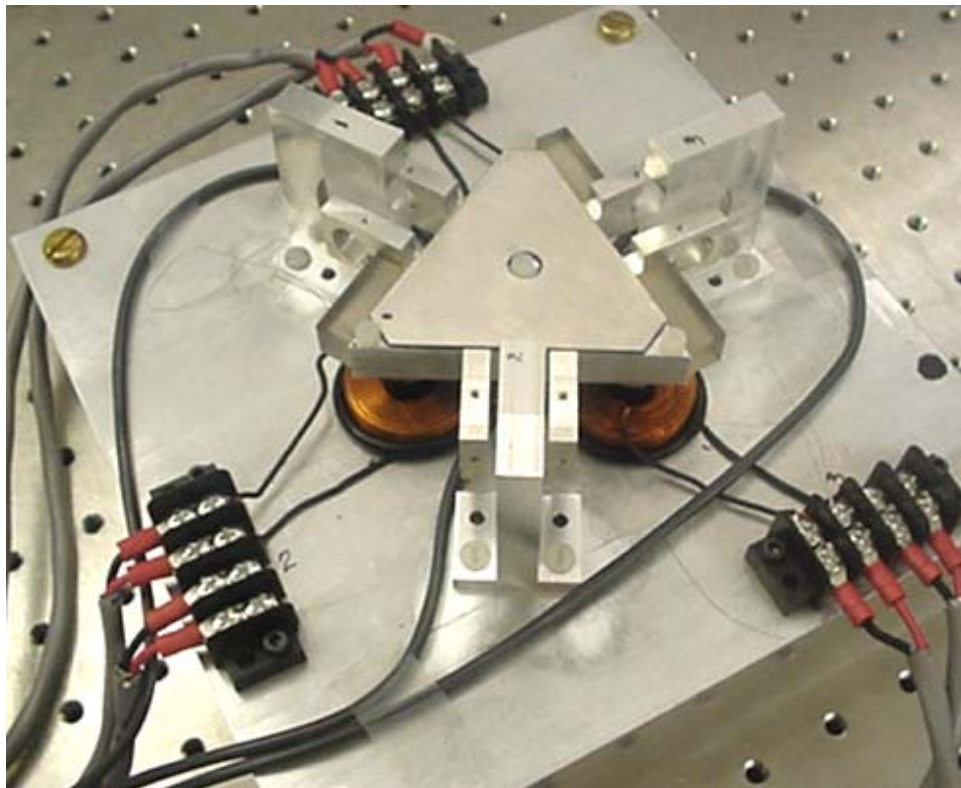
Figure 1-1: Photograph of a 6-DOF maglev device

compact moving stage with high natural frequency, (2) six-axis motion with high resolution and relative large travel range, (3) light weight, and (4) low power consumption. The specification and goal of this device is shown in Table 1-1.

Figure 1-2 shows the generation of six-axis forces by the six actuators. The six-axis forces shown in the figure refer to the center of mass of the moving stage. The values of the actuator forces are calculated by applying six equilibrium conditions around the center of mass. The transform matrix for this calculation is given in (4.22) in Chapter IV.

Table 1-1: Specifications and goals of the maglev device

Linear travel range	500 μm
Angular travel range	3 mrad
Linear resolution	2.5 nm
Angular resolution	100 nrad
Moving platen mass	0.2126 kg
Maximum payload	0.6 kg
Maximum acceleration	10 m/s^2 (1 g)
Nominal current for vertical actuator	0.83 A
Nominal power consumption per horizontal actuator	0 mW
Nominal power consumption per vertical actuator	344 mW
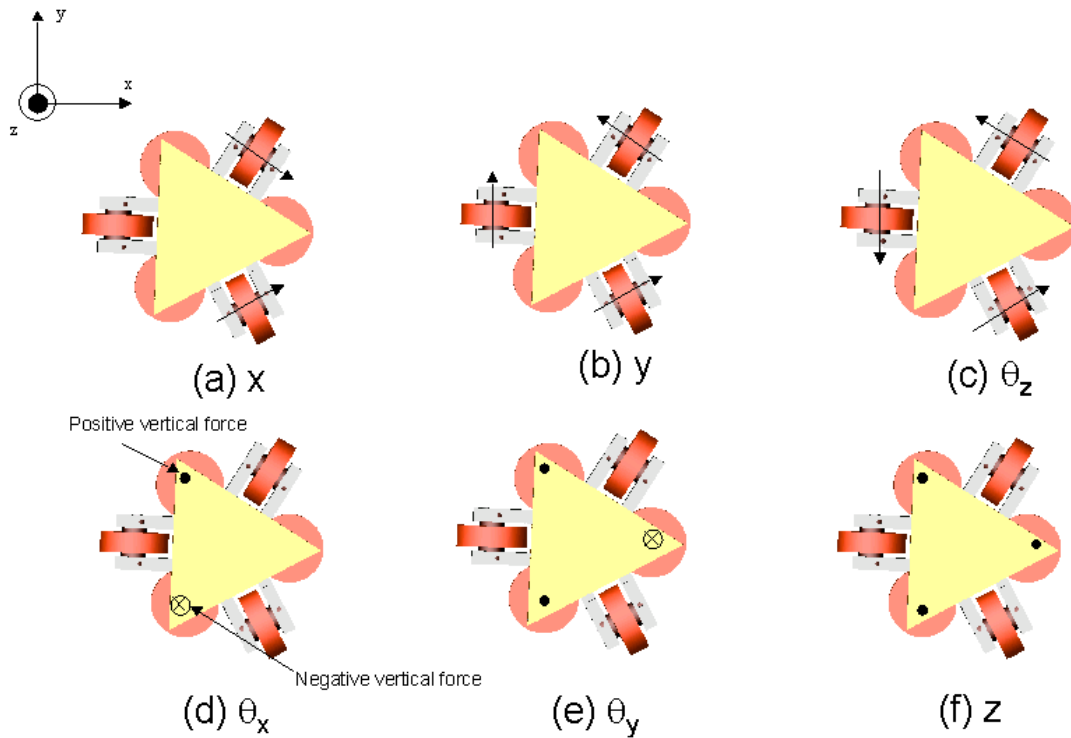
Figure 1-2: Six-axis force generation

1.4 Review of Research on Single-Axis Linear Actuator

The actuators used in this project are based on the research of single-axis maglev actuator by Himanshu Maheshwari [24]. The single-axis maglev actuator is as shown in Figure 1-3. Two magnet pieces are placed with the same (south) poles facing against each other. Between the two magnet pieces is a non-magnetic placeholder, which separates them. This magnet assembly focuses magnetic flux on the current-carrying coil, which is placed concentric to the assembly. The coil generates north and south poles governed by the right-hand rule. With a pole arrangement depicted in Figure 1-3, upward axial force can be generated for the magnets with respect to the stationary coil.

Changing the magnitude of current flowing through the coil controls the magnitude of the force. Reversing the direction of the coil current reverses the direction of the force.
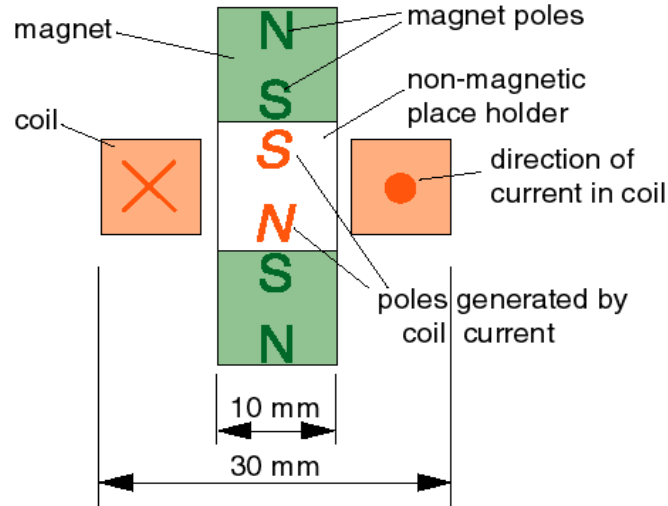
Figure 1-3: Prototype of the maglev linear actuator

The actuator structure comprises two cylindrical neodymium-iron-boron (NdFeB) magnets with energy product (BH_{max}) of 50 MGOe. The magnet is of 10 mm diameter and 9.5 mm length. The two magnets and the non-magnetic placeholder are packaged into a thin-walled brass tube with inside diameter of 10.76 mm and 0.3556 mm wall thickness. The coil is made of AWG #21 wire with an inner diameter of 12.192 mm and 9.5 mm length. Coil resistance and inductance are approximately 0.552 Ω and 0.500 mH.

The Lorentz force between the assembly of permanent magnets and the current-carrying coil can be calculated using the equation: $f = \int (J \times B) \, dV$. The magnetic scalar potential (Ψ) was calculated using superposition integral, which in turn was used to obtain the magnetic flux density (B). The length of the non-magnetic spacer or the distance between the two magnets was optimized, to operate the actuator at its maximum force range. The thickness of the non-magnetic placeholder is 3.975 mm.
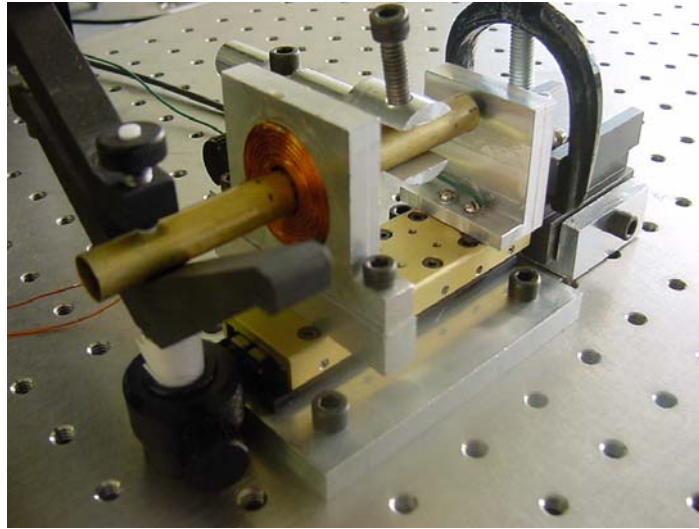
Figure 1-4: Photograph of the experimental setup for the linear actuator

For the current density (J) of 3.5×10^6 A/m^2, the force in the axial direction is 2.37 N at equilibrium position. Experimentally, this force is measured to be 2.34 N with a load cell. This is a difference of 1.26% from the theoretical value. This error can be attributed to the resolution and drift present in the load cell and the friction between the tube and the post-holder.

Figure 1-4 shows Maheshwari's experimental setup to implement a closed-loop controller for the maglev linear actuator. As shown, a magnet assembly is packaged into a 0.355-mm-thick brass tube. The tube is suspended with two bar holders. The coil, packaged in the coil holder, is mounted on a low-friction slider. Thus, in this case, magnets are held stationary and the current-carrying coil is the moving part. A capacitance sensor is used to measure the position of the moving part. The testing results have shown nanopositioning capability of the maglev linear actuator. The detailed design and experimental data can be found from Maheshuwari's thesis [24].

The research on this single-axis maglev actuator contributes to the 6-DOF maglev system in the following aspects: (1) The research provided a theoretical analysis

on the magnetic force generated by the maglev actuator and experimentally proved the accuracy of the theoretical calculation. (2) It proved the nanopositioning capability of the maglev actuator. (3) It provided with much valuable experience in noise reduction to the maglev actuator.

The dimension and structure of the maglev actuator used in the 6-DOF maglev device is slightly different from the above single-axis actuator. Detailed design on the actuator will be shown in the following chapter.

1.5 Thesis Overview

This thesis consists of six chapters. Chapter I presents a review of current development of nanomanipulation and magnetic levitation technology. A review of previous research on the single-axis actuator is provided. The working principle and overview of the new 6-DOF maglev device are explained. Chapter II presents mechanical design and fabrication of the maglev device. An error analysis is provided to show the tolerance of the fabrication and assembly. Chapter III covers the electrical instrumentation of the maglev system. Both hardware construction and software structure are included. Some issues in low-level bus programming such as byte swapping, data format change are also discussed in this chapter. Chapter IV concentrates on the dynamic modeling and control system design for the magnetic levitation. The test results of 6-DOF maglev device are also given in this chapter. Chapter V provides signal analysis for noise prediction and reduction. A stochastic noise/disturbance model is applied to analyze the contribution to the overall noise level from all potential noise resources, such as A/D quantification, floor vibration, electronic noise, etc. In Chapter VI, conclusions and suggestions for future work are given.

The Appendices include the C code of real-time control implemented on DSP and engineering drawings of mechanical parts.

1.6 Thesis Contribution

This thesis shows a novel design of a 6-DOF magnetically levitated device with nanopositioning capability. The potential application of this maglev device includes integrated circuit fabrication, nanoscale manipulation, robotics, remote control, and virtual reality. This 6-DOF maglev device will be a good sample for research in nanoengineering and control theory. It can serve as instrument for the development of more complicated devices for scanning and manufacturing in nanotechnology. Various advanced controllers can be applied to this device.

The work in this thesis is an important part of a three-year project being supported by National Science Foundation under Grant No. CMS-0116642 through Dr. Won-jong Kim. Specifically the contributions of this thesis includes: (1) design and construction of the mechanical system and electrical instrumentation of the maglev device, (2) development of a primary dynamic model and design and implementation of basic controllers to the 6-DOF motion of the maglev system, and (3) analysis and reduction of noise.

CHAPTER II
MECHANICAL DESIGN

The nanometer resolution and 500-μm travel range of this maglev device bring strict requirements to the precision in mechanical design, fabrication, and assembly. With the limitation of available machining condition, we set our machining tolerance goal to be one milliinch which is 25.4 μm. However, errors can be accumulated during the assembly. In the first section of this chapter, an overview of the system is presented. In the next section, detailed designs of some important parts are discussed. Then, the designs of vertical and horizontal actuators are presented. Finally, error analyses are presented to estimate the tolerance from our assembly.

2.1 Overview of the Mechanical Setup

Figure 2-1 shows a perspective view of the whole mechanical setup. Figure 2-2 shows a 3D Solidworks[1] drawing of the 6-DOF maglev device. The lightweight (0.2126 kg) triangular platen with six pairs of single-axis unit actuators on the sides and the bottom is the single moving part of the device. Three horizontal coils are glued in the coil holders which are stationary and fastened on the base plate. Three vertical coils are fixed directly on the base plate. These six coils generate forces to drive the 6-DOF motion of the moving part. A shear-damping layer and a constraint layer are applied to the top surface of the platen to damp out the vibration of the platen. As a result, the mechanical energy due to the relative motion from the constraint layer with respect to the platen is dissipated as heat energy. For the purpose of nanomanipulation, a specimen under inspection or fabrication can be mounted on top of the constraint layer. Finally, the whole system is placed on an optical table which reduces vibration transmitted from the

---

[1] SolidWorks Corporation, 300 Baker Avenue, Concord, Massachusetts 01742
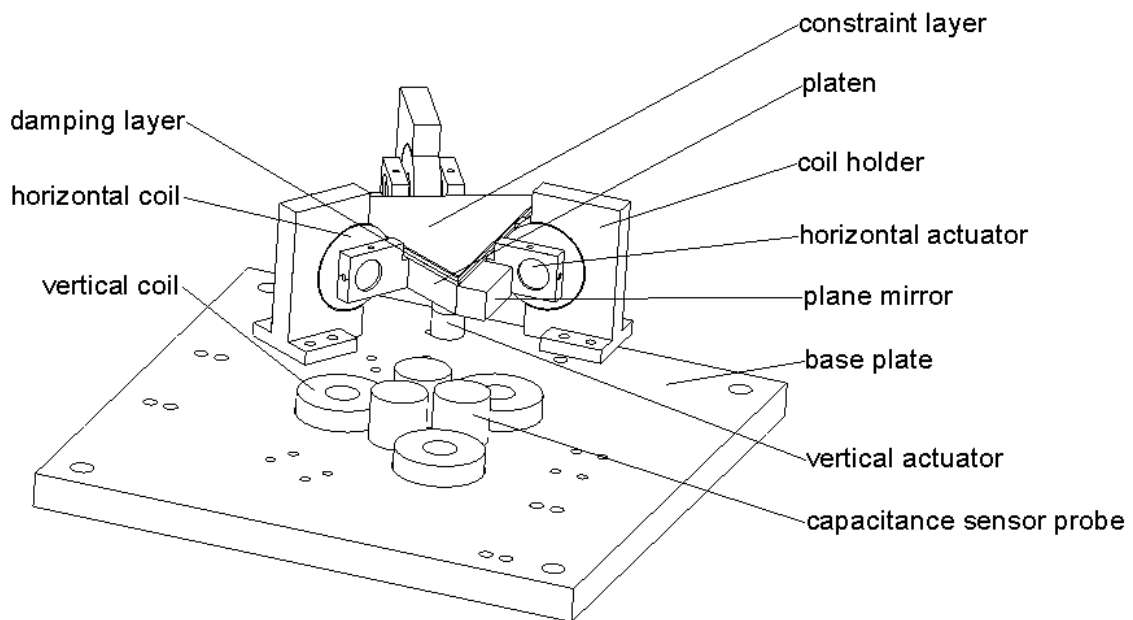
Figure 2-1: Perspective view of mechanical setup
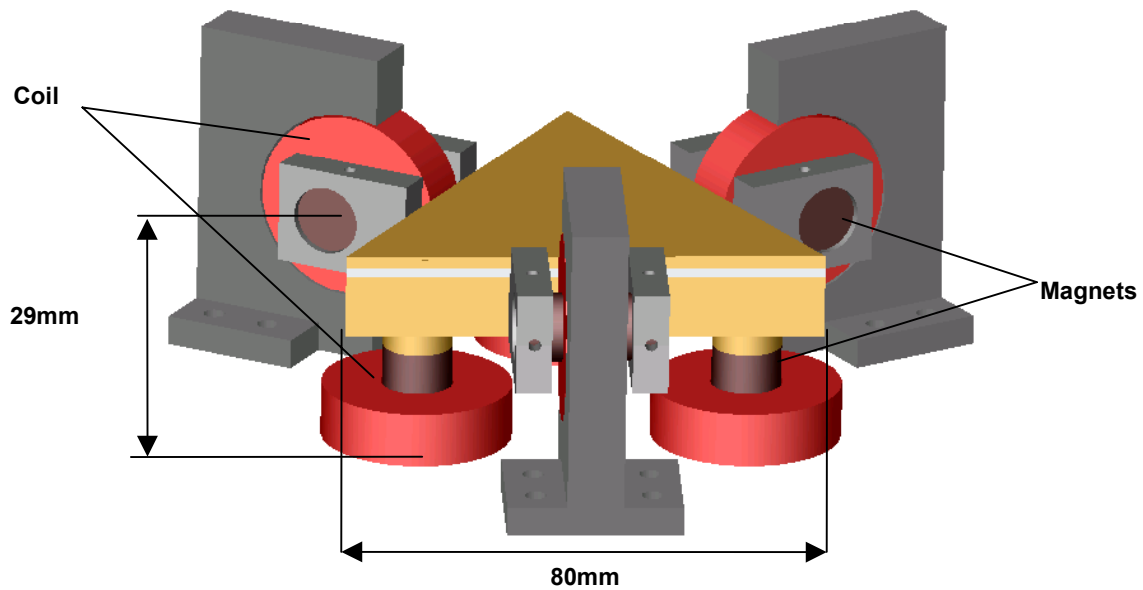
Figure 2-2: 3D view of the maglev device

lab floor.

      The position information referring to three translatory motions and three rotational motions is obtained from three sets of laser interferometers (10706B from Agilent[2]) and three capacitance sensors (Model 2810 gauge and Model 3800 electronics from ADE[3]). Three square mirrors[4] with dimension of 25 × 11 × 11 mm are attached on the two sides of the platen by using double-sided tape. Three capacitance sensor probes are placed on the base plate and use the bottom surface of the platen as their targets.

2.2 Mechanical Design

2.2.1 Platen

      The platen as shown in Figure 2-3 is the only moving part in this levitation system. The material of the platen is aluminum. It was made by Accurate Machine Works[5]. Three pockets on top of the platen are cut out to reduce the weight. The extrusive arms are used for assembling the horizontal magnets. The nine holes on the bottom are left for assembling the three vertical magnets. As the target of capacitance sensors, the bottom surface of the platen is ground to a surface roughness of 25.4 μm (0.001"). Three plane mirrors are mounted to the triangular sides by 127 μm-thick double-sided tape. Four screw holes on top surface of the platen are left for an aluminum top surface. A 1.52 mm-thick C1002 shear damping sheet by E-A-R[6] and a stainless steel constraint layer are bonded on top of the top surface by double-sided tape. Figure 2-4 shows the exploded view of the platen.

---

[2] Agilent Technologies, 395 Page Mill Rd., Palo Alto, California 94303

[3] ADE Corp., 77 Rowe Street, Newton, Massachusetts 12166

[4] Bond Optics, Etna Road, Dept. 60H Lebanon, New Hampshire 03766

[5] Accurate Machine Works, 4400 Pate Road, College Station, Texas 77845

[6] E-A-R Specialty Composites, 7911 Zionville Road, Indianapolis, Indiana 46268
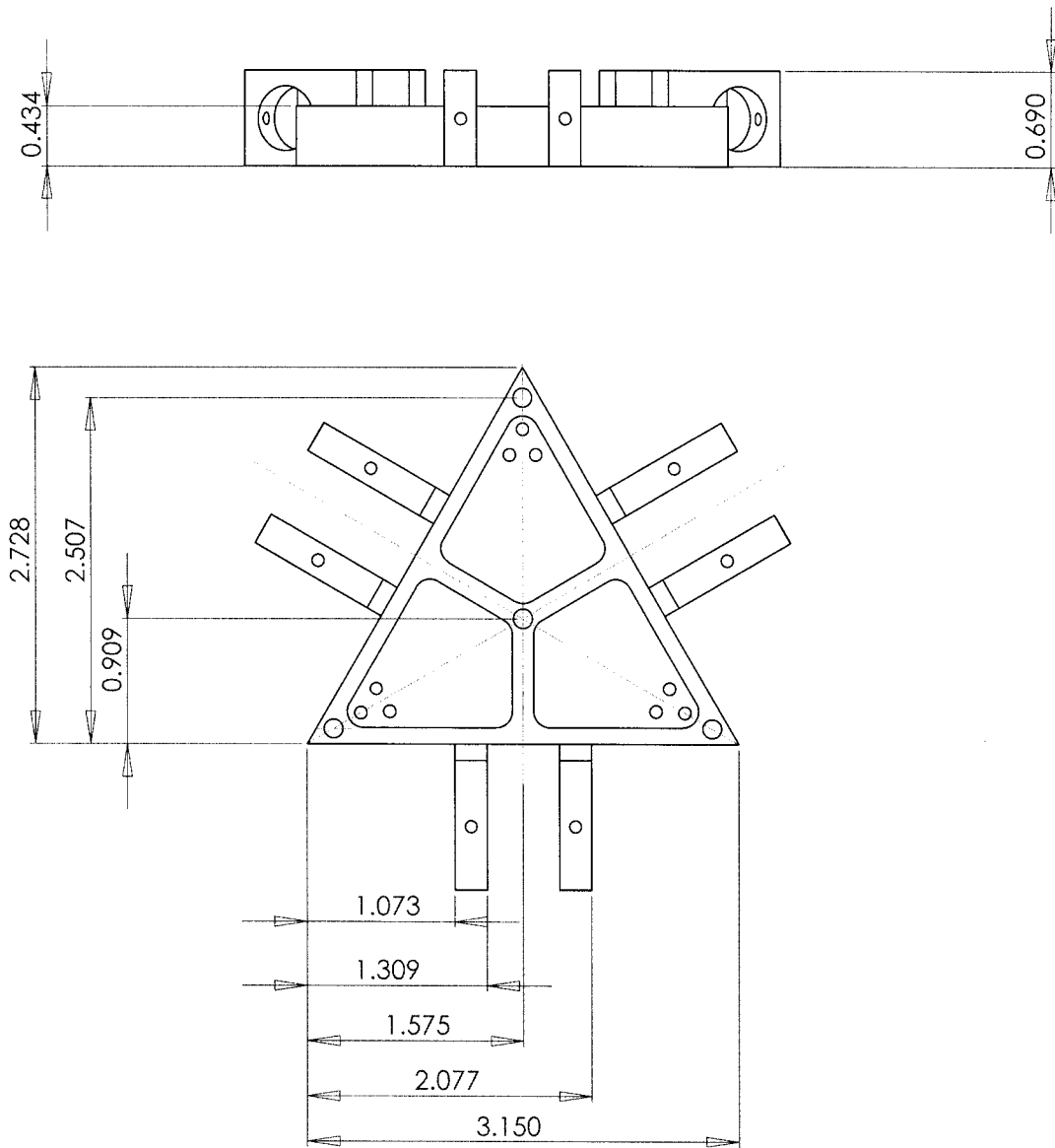
Figure 2-3: Side and top view of the platen
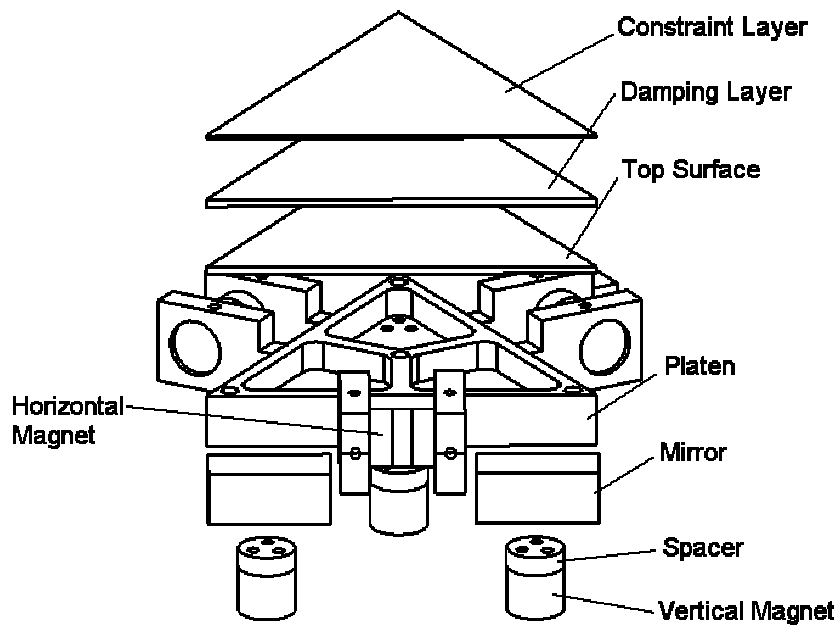
Figure 2-4: Exploded view of the assembly of platen

2.2.2 Coil Assembly

The coils used for actuators are made up of single-build AWG#21 copper magnet wire (diameter = 0.724 mm), and has 179 turns. The coil resistance and inductance are 0.552 Ω and 0.5 mH. The manufacturer[7] has ensured the inner diameter geometric tolerance of the coil better than ±0.001". The coils must be properly placed to provide six-axis forces to the magnets mounted on the platen. Shobhit Verma, another graduate student in our laboratory contributed the idea and performed most of the work for the coil assembly. The assembly of vertical coils is shown in Figure 2-5. Vertical

---

[7] WireWinders, Inc., 121 Mount Vernon Road, Milford, New Hampshire 02055

coils are glued with PC-7 Epoxy[8] on small spacers which have the same dimension of the inner diameter of the coils. Then the spacers are fastened to the base plate. The purpose of using the spacers is to make the coils removable so that we can simply replace the coils if some damages happen to them. Cautions need to be taken when gluing the spacers to the coil. If the coil coating is scratched, the coil will be electrically shorted to the spacer, and further shorted to the base place. This can significantly increase the noise on the capacitance sensor because the sensor probes are installed on the base plate.
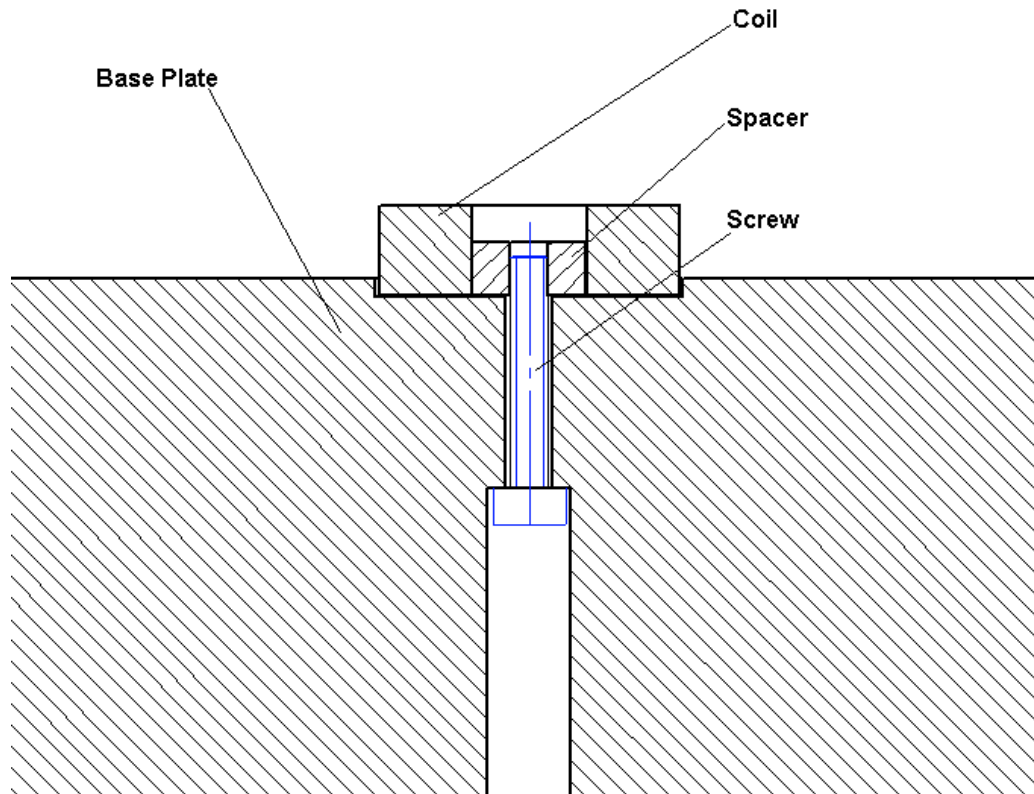
Figure 2-5: Vertical coil assembly

---

[8] PC-Products™ Protective Coating Co., Allentown, Pennsylvania 18102

Differently from vertical coils, horizontal coils are first glued to the coil holders by using a fixture to maintain the precise position of the coil. Verma fabricated the fixture. Next, the coil holder is fastened on the base plate. Since the outer diameter of the coil has large tolerance which makes the outer surface unreliable, we made a fixture to hold the coil by relying on the inner surface of it. Figure 2-6 shows a view of the coil holder and the fixture for gluing.

Assembly Fixture   Coil Holder
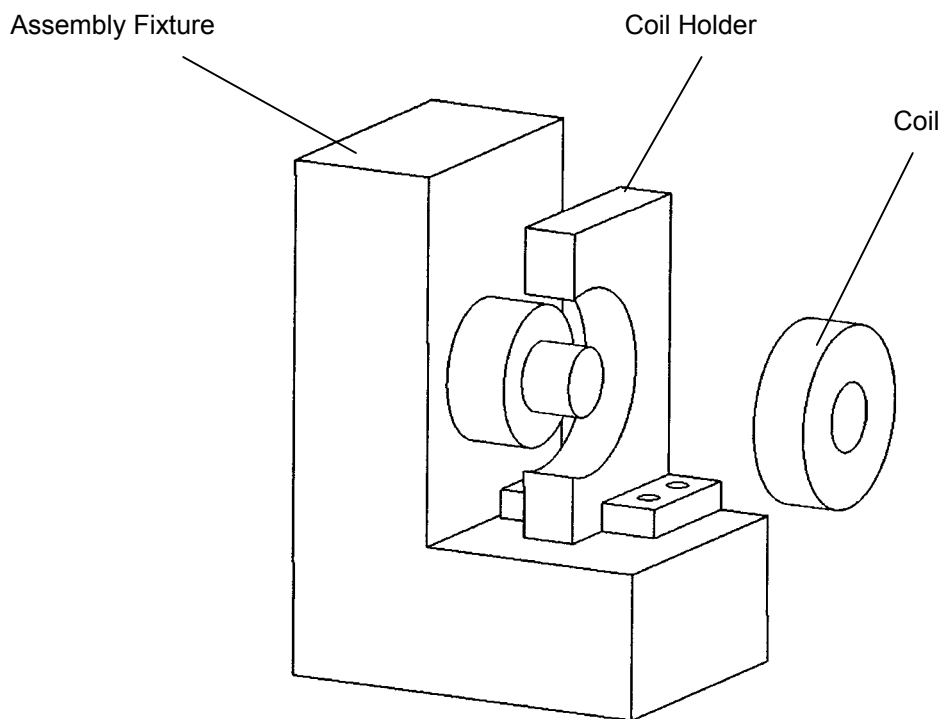
Coil

Figure 2-6 Assembly of horizontal coil

2.2.3 Base Plate

Base plate is where the whole system is set up. Appendix B gives the engineering drawing of the base plate. Verma fabricated the base plate using the machines in our department's machine shop. The parts directly mounted on the base plate include horizontal coil holders, vertical coils, capacitance sensor probes, and terminal blocks for lead wires.

The height of the base plate is designed to match the height of laser beams which come from laser head. The position of all screw holes must have tolerance as small as possible to maintain the precision of the assembled parts. The material of the base plate is aluminum. Experiments show that the optical table can transmit electronic noise (such as 60 Hz power noise) to the base plate. This noise can influence the performance of the capacitance sensors. In this case, a 254-μm plastic isolation shim is placed between the base plate and optical table.

2.3 Vertical and Horizontal Actuators

The magnet mounts are designed to be removable so that we can easily adjust and replace the magnets on the actuators. For the assembly of horizontal actuators, two magnets are glued to an aluminum spacer whose length is calculated to maintain the maximum force between the magnets and the coil. Next, the assembled magnets are inserted into the holes on the extrusive parts on the platen and are orientated by the inner surface of the hole with two pairs of screws. Basically, we only use two screws to fasten the magnet to the inner surface of the hole. In case we need to adjust the magnets precisely, we can make use of a different pair of the three screws. The assembly of the vertical magnets is simpler than that of horizontal magnets. The magnet is glued on a

3.84-mm-thick aluminum spacer with three tapped holes on it. Then, the spacer is fastened to the bottom surface of the platen by three 2-56 screws.

Figure 2-7 shows the horizontal and vertical actuator assembly. Verma helped me for assemble the actuators. The maximum magnetic force from each actuator depends on the dimension of magnets and coil. Based upon the experiment on our single-axis actuator, we use magnets with 11.684-mm diameter and 9.525-mm height from Magnetic Component Engineering[9]. The neodymium-iron-boron (NeFeB) magnets have phenolic resin coating to prevent corrosion. The theoretical force with a 1-A nominal current is 1.68 N from each horizontal actuator and 0.84 N from each vertical actuator. As a result, the total force with the 1-A nominal current from three vertical actuators is 2.52 N which is sufficient to levitate the moving-stage mass of 0.2126 kg.
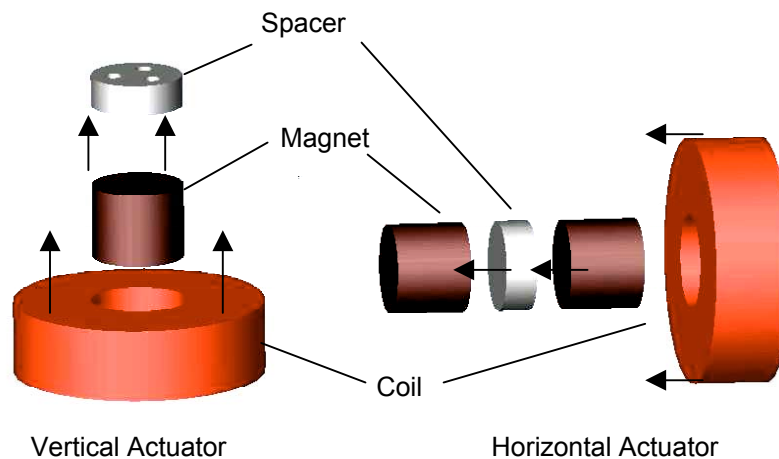
Figure 2-7: Vertical and horizontal actuator assembly. The arrows indicate the direction of assembling

[9] Magnetic Component Engineering, Inc., 23145 Kashiwa Court, Torrance, CA 90505

2.4 Error Analysis

The relative position of the magnet and the coil will limit the travel range. Thus, we need to maintain a high precision of the position of each actuator. The clearance between coil and magnet is 508 μm. This value is set to prevent the platen from travelling beyond the sensing range of the capacitance probes. The error analysis can help us estimate the errors and the clearance we need to compensate these errors.
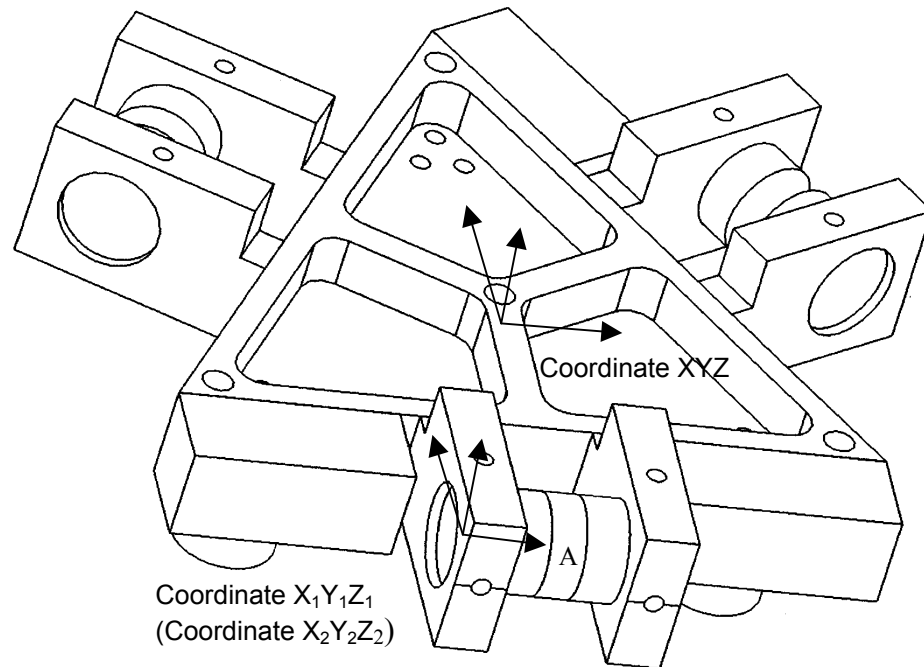
Figure 2-8: Coordinate setting for error analysis of horizontal actuator

The errors can be accumulated or amplified at the place where two or more parts are connected. Coordinate transformation matrix is used to display the coordinate of a point in a different coordinate system. Coordinate transformation can also be used to record the effects of error sources. We set a coordinate system at the individual part where the error can be involved. The error values are estimated based on fabrication and assembly accuracy. By using coordinate transformation sequentially along the assembled parts, the accumulation and amplification of errors can be evaluated by comparing the ideal coordinate of a point and the calculated coordinate after coordinate transformations. Following are the notations used in coordinate transformation.

δ_x : Translational error in the X axis;

δ_y : Translational error in the Y axis;

δ_z : Translational error in the Z axis;

ε_x : Rotational error around the X axis;

ε_y : Rotational error around the Y axis;

ε_z : Rotational error around the Z axis;

2.4.1 Error in Horizontal Actuator

The origin of the initial coordinate XYZ is set at the center of mass of our platen. Then a second coordinate system $X_1Y_1Z_1$ shown in Figure 2-8 is set at the center of the hole for horizontal actuator on the platen. The transformation from the coordinate systems $X_1Y_1Z_1$ to XYZ is

$$R_1 = \begin{bmatrix} 1 & -\varepsilon_{1z} & \varepsilon_{1y} & X_{01} + \delta_{1x} \\ \varepsilon_{1z} & 1 & \varepsilon_{1x} & Y_{01} + \delta_{1y} \\ -\varepsilon_{1Y} & \varepsilon_{1x} & 1 & Z_{01} + \delta_{1z} \\ 0 & 0 & 0 & 1 \end{bmatrix} \quad , \tag{2.1}$$

where $(X_{01}, Y_{01}, Z_{01}) = (27.07746, -15.15852, -5.61615)$ in mm. $\delta_{1x}, \delta_{1y}, \delta_{1z}, \varepsilon_{1x}, \varepsilon_{1y},$

and ε_{1z} come from the fabrication tolerance of the hole. Therefore,

$\delta_{1x} = \pm 0.001" = \pm 0.0254 \text{ mm}, \delta_{1y} = \pm 0.0254 \text{ mm}, \delta_{1z} = \pm 0.0254 \text{ mm},$

$\varepsilon_{1x} = \pm 0.0001 \text{ rad}, \varepsilon_{1y} = \pm 0.0001 \text{ rad}, \varepsilon_{1z} = \pm 0.0001 \text{ rad}.$

Then a third coordinate system $X_2Y_2Z_2$ is set at the body of the magnet. It is at the same point as $X_1Y_1Z_1$, but it is located on the magnet and the X_1 axis is aligned with the symmetric axis of magnets instead of the symmetric axis of the hole. Therefore, the second transformation matrix is

$$R_2 = \begin{bmatrix} 1 & -\varepsilon_{2z} & \varepsilon_{2y} & X_{02} + \delta_{2x} \\ \varepsilon_{2z} & 1 & \varepsilon_{2x} & Y_{02} + \delta_{2y} \\ -\varepsilon_{2y} & \varepsilon_{2x} & 1 & Z_{02} + \delta_{2z} \\ 0 & 0 & 0 & 1 \end{bmatrix}, \tag{2.2}$$

where $(X_{02}, Y_{02}, Z_{02}) = (0, 0, 0)$. $\delta_{2x} = \pm 0.0254$ mm because of the assembly tolerance in the X axis. $\delta_{2y} = \delta_{2z} = \pm 0.0127 \text{ mm}/2 = \pm 0.0064$ mm which comes from 0.0005" outer diameter tolerance of the magnets. $\varepsilon_{2x} = 0$, because of the symmetry of the cylinder. By referring to Figure 2-9, we get the values of ε_{2y} and ε_{2z} shown below:

$$\varepsilon_{2y} = \varepsilon_{2z} = \pm \frac{0.0127 \text{ mm}}{19.5 \text{ mm}} = \pm 0.00065 \text{ rad}.$$

The center of the actuator A has coordinate of $A_2 = (9.75, 0, 0)^T$ in $X_2Y_2Z_2$. The ideal position of A in XYZ coordinate is $A = (-0.4189, -40.3861, 3.1469)$ in mm. Then, we can get the real position of point A in the coordinate system XYZ. It is $A_0 = R_1R_2A_2$ $= (-0.3681, -40.3523, 3.186)$ in mm. Finally we get the possible tolerance of point A which is $EA = A_0 - A = \pm(50.8, 33.8, 39.1)$ in μm.

Next, we want to estimate the tolerance of the same point on the corresponding coil at the same horizontal actuator. We use the same original coordinate system XYZ

which is located at the center of mass of the platen. Referring to Figure 2-9, the coordinate system $X_1Y_1Z_1$ is set at the bottom center of the coil holder. The transformation from the coordinate systems $X_1Y_1Z_1$ to XYZ is

$$R_1 = \begin{bmatrix} 1 & -\varepsilon_{1z} & \varepsilon_{1y} & X_{01}+\delta_{1x} \\ \varepsilon_{1z} & 1 & \varepsilon_{1x} & Y_{01}+\delta_{1y} \\ -\varepsilon_{1Y} & \varepsilon_{1x} & 1 & Z_{01}+\delta_{1z} \\ 0 & 0 & 0 & 1 \end{bmatrix}, \tag{2.3}$$

where $(X_{01}, Y_{01}, Z_{01}) = (-0.4189, \ -68.3515, \ -24.1032)$ in mm. $\delta_{1x}, \delta_{1y}, \delta_{1z}, \varepsilon_{1x}, \varepsilon_{1y},$

and ε_{1z} come from the clearance and fabrication tolerance of the screw holes. Therefore,

$$\delta_{1x} = \pm 0.0762\,\text{mm}, \delta_{1y} = \pm 0.0762\,\text{mm}, \delta_{1z} \cong 0,$$
$$\varepsilon_{1x} \cong 0\,\text{rad}, \varepsilon_{1y} \cong 0\,\text{rad},$$
$$\varepsilon_{1z} = \pm \frac{\dfrac{0.006 \times 25.4}{2}}{18.7} = \pm 0.0041\,\text{rad}.$$

Since the coil is assembled by using the fixture. The coordinate $X_2Y_2Z_2$ is set at the point on the fixture where the coil center is located. So the second transformation matrix is

$$R_2 = \begin{bmatrix} 1 & -\varepsilon_{2z} & \varepsilon_{2y} & X_{02}+\delta_{2x} \\ \varepsilon_{2z} & 1 & \varepsilon_{2x} & Y_{02}+\delta_{2y} \\ -\varepsilon_{2y} & \varepsilon_{2x} & 1 & Z_{02}+\delta_{2z} \\ 0 & 0 & 0 & 1 \end{bmatrix}, \tag{2.4}$$

where $(X_{02}, Y_{02}, Z_{02}) = (0, \ 27.9654, \ 27.2491)$ in mm.

$\delta_{2x} = \delta_{2y} = \delta_{2z} = \pm 0.0254\,\text{mm}$ which come from the fabrication tolerance; $\varepsilon_{2x} = 0$ because

of the symmetry of the cylindrical inner surface of coil; $\varepsilon_{2y} = \varepsilon_{2z} = \pm0.0001$ rad from the fabrication tolerance.

The center of the coil B has coordinate of $B_2 = (0, 0, 0)^T$ in $X_2Y_2Z_2$. The ideal position of B in the XYZ coordinate system is B=(−0.4189, −40.3861, 3.1469) in mm. Then, we can get the real position of point B in the coordinate system XYZ. It is $B_0 = R_1R_2B_2 =$ (−0.2025, −40.2844, 3.1713) in mm. Finally we get the possible tolerance of point A: EB = $B_0 - B = \pm$(216.4, 101.7, 24.4) in μm.

As a result, the point on the magnet has position tolerance of $\pm$(50.8, 33.8, 39.1) in μm and the corresponding point on the coil has position tolerance of $\pm$(216.4, 101.7, 24.4) in μm. The large tolerance value on the coils in the X axis and the Y axis comes from the 150-μm clearance of the screw holes on coil holder. However, we can adjust the coil holder manually and try to locate the screw at center of holes. In this case, we finally expect the tolerance to be within $\pm$50.8 μm.
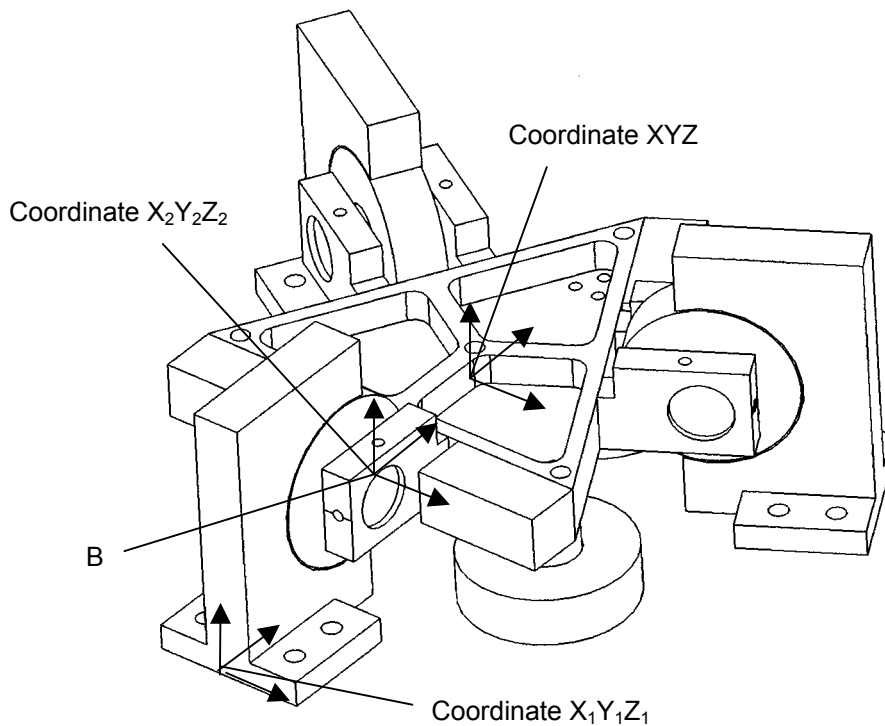
Figure 2-9: Coordinate setting for error analysis of horizontal coil

2.4.2 Error in Vertical Actuator

The origin of the initial coordinate system XYZ is set at the center of mass on our platen. Then, a second coordinate system $X_1Y_1Z_1$ shown in Figure 2-10 is set at the center of the top surface on the spacer of vertical actuator.
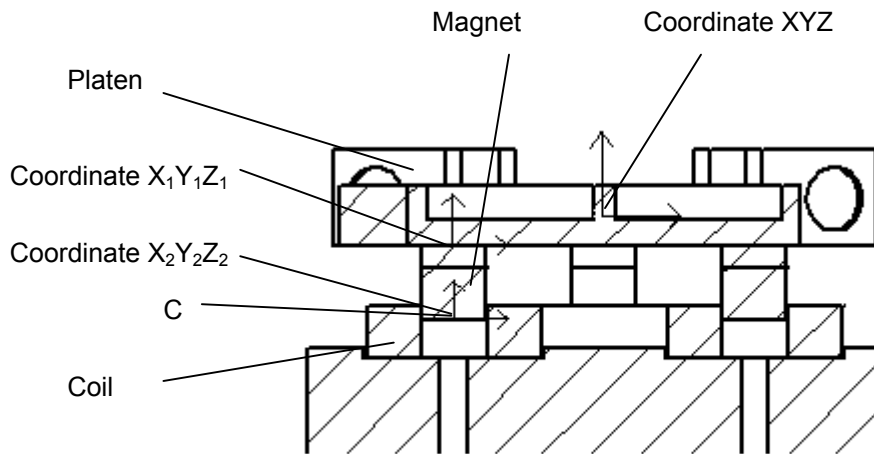
Figure 2-10: Coordinate setting for error analysis of vertical actuator

The transformation from the coordinate systems $X_1Y_1Z_1$ to XYZ is

$$R_1 = \begin{bmatrix} 1 & -\varepsilon_{1z} & \varepsilon_{1y} & X_{01}+\delta_{1x} \\ \varepsilon_{1z} & 1 & \varepsilon_{1x} & Y_{01}+\delta_{1y} \\ -\varepsilon_{1Y} & \varepsilon_{1x} & 1 & Z_{01}+\delta_{1z} \\ 0 & 0 & 0 & 1 \end{bmatrix}, \tag{2.5}$$

where $(X_{01}, Y_{01}, Z_{01}) = (27.07746,\ -15.15852,\ -5.61615)$ in mm. $\delta_{1x}, \delta_{1y}, \delta_{1z}, \varepsilon_{1x}, \varepsilon_{1y},$ and ε_{1z} come from the 0.003" clearance and fabrication tolerance of the screw holes. Thus,

$$\delta_{1x} = \pm0.0381\,\text{mm}, \delta_{1y} = \pm0.0381\,\text{mm}, \delta_{1z} = 0\,\text{mm},$$
$$\varepsilon_{1x} = \pm0.0001\,\text{rad}, \varepsilon_{1y} = \pm0.0001\,\text{rad}, \varepsilon_{1z} = 0\,\text{rad}.$$

Then, a third coordinate system $X_2Y_2Z_2$ is set at the bottom center of the magnet. The second transformation matrix is

$$R_2 = \begin{bmatrix} 1 & -\varepsilon_{2z} & \varepsilon_{2y} & X_{02} + \delta_{2x} \\ \varepsilon_{2z} & 1 & \varepsilon_{2x} & Y_{02} + \delta_{2y} \\ -\varepsilon_{2y} & \varepsilon_{2x} & 1 & Z_{02} + \delta_{2z} \\ 0 & 0 & 0 & 1 \end{bmatrix} , \tag{2.6}$$

where $(X_{02}, Y_{02}, Z_{02}) = (0,\ 0,\ -13.525)$ in mm. $\delta_{2x} = \delta_{2y} = \delta_{2z} = \pm0.0254\,\text{mm}$ because of the assembly tolerance of actuator. $\varepsilon_{2z} = 0$ which comes from the symmetry of the cylinder. $\varepsilon_{2x} = \varepsilon_{2y} = \pm0.0001$ rad which comes from the fabrication tolerance of the assembly fixture.

Finally, the point at the bottom center of the magnet C has desired coordinate of $(27.07746,\ -15.15852,\ -19.14115)$ in mm in the coordinate system XYZ. It has coordinate of $(0,\ 0,\ 0)$ in mm in the coordinate system $X_2Y_2Z_2$. So we get the real position of C as $C_0 = R_1R_2C_2 = (27.1396,\ -15.0964,\ -19.1157)$ in mm. So the tolerance of C point is EC = C-C0 = $\pm(62.2,\ 62.2,\ 25.4)$ in μm.

Next, we calculate the tolerance of the corresponding coil to the same actuator. We use the same original coordinate system XYZ which is located at the center of mass of the platen.

Coordinate XYZ

Coordinate X₁Y₁Z₁

D
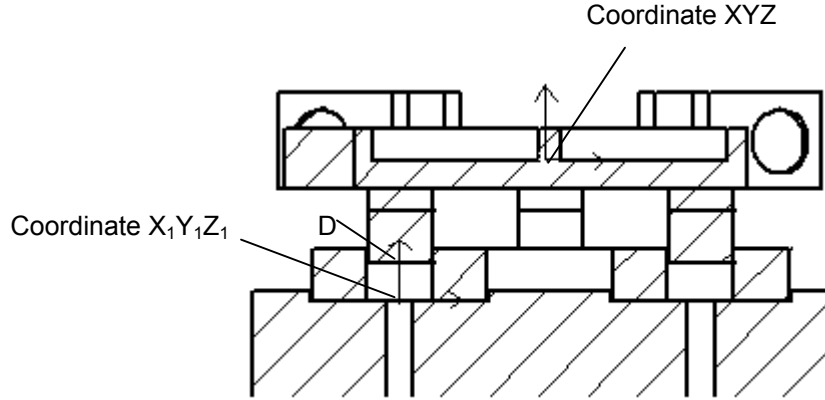
Figure 2-11: Coordinate setting for error analysis of vertical coil

Referring to Figure 2-11, the coordinate system $X_1Y_1Z_1$ is set at the bottom center of the coil. The transformation from the coordinate systems $X_1Y_1Z_1$ to XYZ is

$$
R_1 = \begin{bmatrix}
1 & -\varepsilon_{1z} & \varepsilon_{1y} & X_{01} + \delta_{1x} \\
\varepsilon_{1z} & 1 & \varepsilon_{1x} & Y_{01} + \delta_{1y} \\
-\varepsilon_{1Y} & \varepsilon_{1x} & 1 & Z_{01} + \delta_{1z} \\
0 & 0 & 0 & 1
\end{bmatrix},
\tag{2.7}
$$

where $(X_{01}, Y_{01}, Z_{01}) = (27.07746, \ -15.15852, \ -25.90365)$ in mm. $\delta_{1x}, \delta_{1y}, \delta_{1z}, \varepsilon_{1x}, \varepsilon_{1y}$, and ε_{1z} come from the 0.006" clearance of the screw holes. So

$$\delta_{1x} = \pm 0.0762 \, \text{mm}, \delta_{1y} = \pm 0.0762 \, \text{mm}, \delta_{1z} \cong 0,$$
$$\varepsilon_{1x} \cong 0.0001 \, \text{rad}, \varepsilon_{1y} \cong 0.0001 \, \text{rad}, \varepsilon_{1z} = 0 \, \text{rad}.$$

The point D on the coil has desired coordinate of (27.07746, −15.15852, −19.14115) in mm in the coordinate system XYZ. It has coordinate of (0, 0, 6.76250) in mm in the coordinate system $X_1Y_1Z_1$. So we get the real position of D as $D_0 = R_1D_1 =$ (27.1543, −15.0816, −19.1412) in mm. Thus, the tolerance of D point is

ED = D − D0 = ±(76.9 , 76.9, 0) in μm.

As a result, the point on the magnet has position tolerance of ±(62.2, 62.2, 25.4) in μm and the corresponding point on the coil has position tolerance of ±(76.9, 76.9, 0) in μm. By doing some adjustment with clearance from the screw holes, we finally expect the tolerance to be within 50.8 μm.

CHAPTER III

ELECTRICAL SYSTEM SETUP

This chapter first gives an overview of the instrumentation structure. In the second section, detailed discussion is given to some instrumentation components including VME bus, Digital Signal Processor (DSP), Analog to Digital (A/D) and Digital to Analog (D/A) board and sensors. Design of power amplifiers and anti-aliasing filter are presented in the following section. The last section discusses the control routines and some software issues.

3.1 Instrumentation Structure

The instrumentation structure is shown in Figure 3-1.
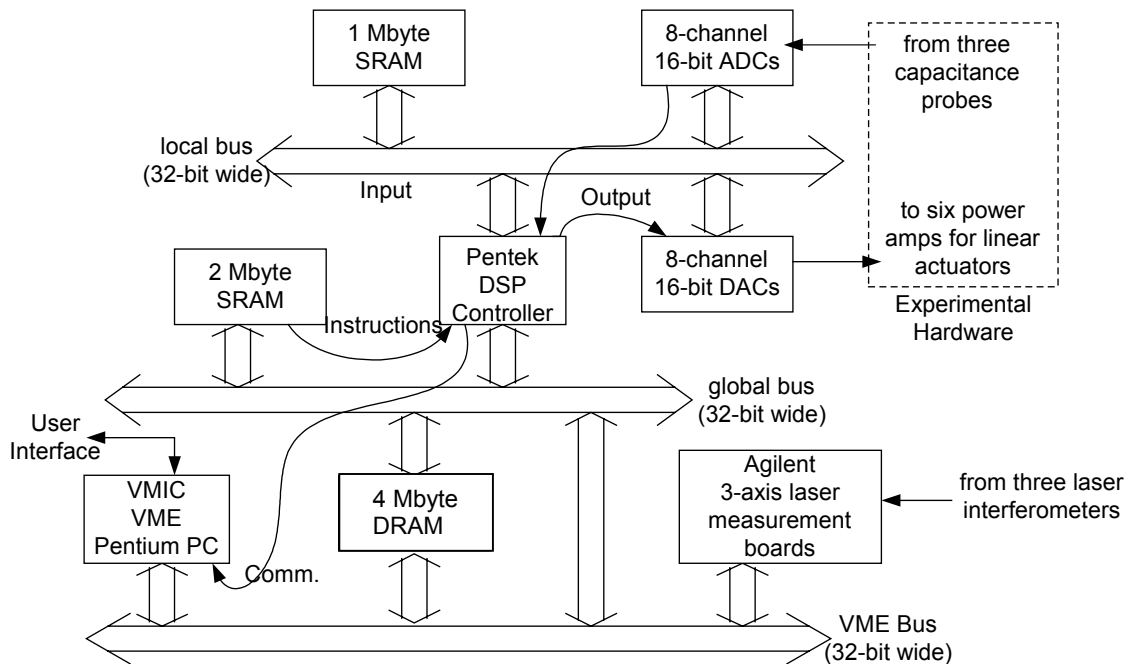
Figure 3-1 Instrumentation structure

The Pentek[10] 4284 TMS320C40 DSP board performs the real-time control while the VMIC[11] VME PC takes care of the user interface and command interpretation. The VME PC and DSP communicate with each other over VME bus through the 4MB dual-port shared RAM residing in the Pentek 4284 board. The laser axis boards which can achieve 0.6-nm position resolution communicate with the DSP board over VME bus. Sixteen-bit A/D converters are employed to receive and convert the data obtained from the capacitance sensors. This Pentek 6102 A/D converter board communicates with DSP via MIX bus. As a result, we can reduce the data traffic over VME bus. The 16-bit D/A converters located on the Pentek 6102 board generate control signals which are fed to six linear power amplifiers to drive six magnetic actuators.

3.2 Digital Signal Processor

Pentek 4284 digital signal processor board takes care of the real-time control in our instrumentation. Pentek 4284 is based on the Texas Instruments[12] TMS320C40 Floating Point Digital Signal Processor. It has 1 MB local SRAM, 1 MB global SRAM, and 4 MB Dual-Access DRAM. It acts as both a VMEbus Master and a MIX bus Master. Since all data-types in Pentek 4284 are 32-bit wide, the 4 MB dual-port DRAM can be used to save 1 Mega data points. In our application, the dual-port DRAM is set to the address from 0x80000000 to 0x800FFFFF. The address from 0x80000000 to 0x8007FFFF is actually used in this project as shared memory with the VMIC VME PC for data exchange.

Attention must be paid to the difference between the dual-port memory address in Pentek 4284 board and that in VMEbus. Since VMEbus has data width of 8 bit, one

---

[10] Pentek, Inc., 55 Walnut Street, Norwood, New Jersey 07648

[11] VMIC, 12090 S. Memorial Pkwy, Huntsville, Alabama 35803

[12] Texas Instruments, Inc., P.O.Box 655303, Dallas, Texas 75265

memory unit in Pentek 4284 refers to 4 memory units in VMEbus. Equation (3.1) gives the translation between these two memory addresses.

$$\text{TMS320C40 address} = \frac{\text{VMEbus address}}{4} + 0xB0000000 \qquad (3.1)$$

Since TMS320C40 uses its unique floating-point format and IBM PC compatibles use the IEEE floating-point format, data conversion must be done when getting data from DSP to the VME PC.

3.3 VMEbus

VMEbus is an abbreviation of Versa Module Enrocard bus. VME began as a unified memory/IO bus for the MC68000 with a 16-bit data path and 24 bit addressing. It was an adaptation of Motorola's Versabus for the MC68000 microprocessor family. It was subsequently standardized in the US as IEEE 1014-1987 and in Europe as IEC 821. As standardized by the IEEE in 1987, the VME data path was asynchronous, with separate 32-bit address and 32-bit data paths, and supported the following transactions: (1) Single Transfer Read/Write, 8, 16, 32 bits; (2) Single Transfer Non-aligned 16, 24 bits (3) Block Transfer Read/Write; (4) Read-Modify-Write, 8, 16, 32 bits; (5) Interrupt Acknowledge (IACK) cycle. A recent version VME64 has capability of 64-bit addressing, 64-bit data path width and 80 megabytes/s data transfer. The advantages of VMEbus include high bandwidth, wide addressing range and data path, multiprocessing support and distributed interrupt handling [25, 26].

The VME PC and other VME electronic boards such as the laser interferometer boards are located in a standard VME chassis. In our VME chassis, slots 1 through 4 are used by the VME PC which has priority of bus request and prevents bus contention. Slot 5 is occupied by Pentek 4284 board while slot 6 is occupied by Pentek 6102 A/D and D/A board. Slots 17 through 20 are used by three laser interferometer boards.

Attention must be paid to the byte ordering in VME communication. There are two systems in byte ordering, big endian and little endian. In big-endian architectures,

the leftmost bytes (those with a lower address) are most significant. In little-endian architecture, the rightmost bytes are most significant. Since our VME PC follows Intel byte ordering convention (little endian) while Pentek DSP and the rest electronic boards in the VMEbus system follow Motorola byte ordering convention (big endian), byte swapping must be done when dealing with the data between these two modules. Fortunately, we do not have to do the byte swapping in our program. The byte swapping can be automatically achieved by Pentek's SwiftNet which is installed in our VME PC. SwiftNet is a software which provides a simple, interrupt-driven, interdevice communication protocol for distributed DSP applications. By properly setting Swiftnet, byte swapping can be automatically done during its running.

3.4 A/D and D/A Converter Board

Pentek 6102 board has a 16-bit 8-channel A/D converter and a 16-bit 8-channel D/A converter. The sampling rate for all 16 channels is up to 250 kHz; the analog input impedance of A/D channel is 100 kΩ. The analog input voltage of A/D channel is ± 5.0 V (differential). The output voltage of D/A channel is ± 5.0 V.

Three A/D channels (Channels A1, B1, and C1) are used to receive the measurement from three capacitance sensors. The output voltages from capacitance sensors are set to be within ± 5.0 V to match the A/D input range. Another A/D channel (Channel D1) is used to generate the VME bus interrupt signal. Pentek 6102 can generate interrupts under many different conditions of its A/D and D/A channels. The sampling rate is set to be 5 kHz. Whenever there is a data available to channel D1 (also available to other channels at the same time), an interrupt signal which refer to the empty condition of channel D1 will be generated to the VMEbus. Then, the program will process the interrupt program, our real-time control routine. In the control routine, the channel D1 is cleared to guarantee the interrupt can happen in the next time. By doing this, we can maintain our control routine working at the 5-kHz sampling rate. Six

D/A channels are used to output control signals to six power amplifiers which will drive the six actuators.

3.5 Power Amplifiers and Anti-aliasing Filters

Six channels of power amplifiers are built to drive the magnetic actuators. The output from D/A channels is ± 5.0 V. We set our maximum current in the coils to 2.5 A. Therefore, the gain of the power amplifiers is set to 0.5. The initial design of the power amplifiers is made by Kim [16]. The differential amplifier, the feedback amplifier, and the power booster are the main parts of the power amplifiers. The differential amplifier is used to remove common-mode noise signals from D/A converters. The feedback amplifier is provided to stabilize the current control loop. A PA12A from Apex[13] serves as the power booster.
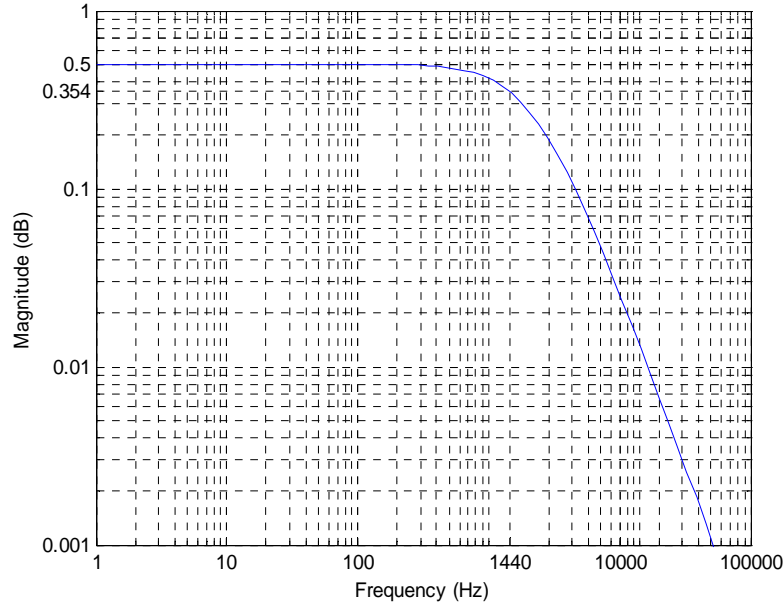
Figure 3-2: Power amplifier frequency response

---

[13] Apex Microtechnology Corp., 5980 N. Shannon Road, Tucson, Arizona 85741

10.0 kΩ

Capacitive Gage

A/D Converter

0.015 µF
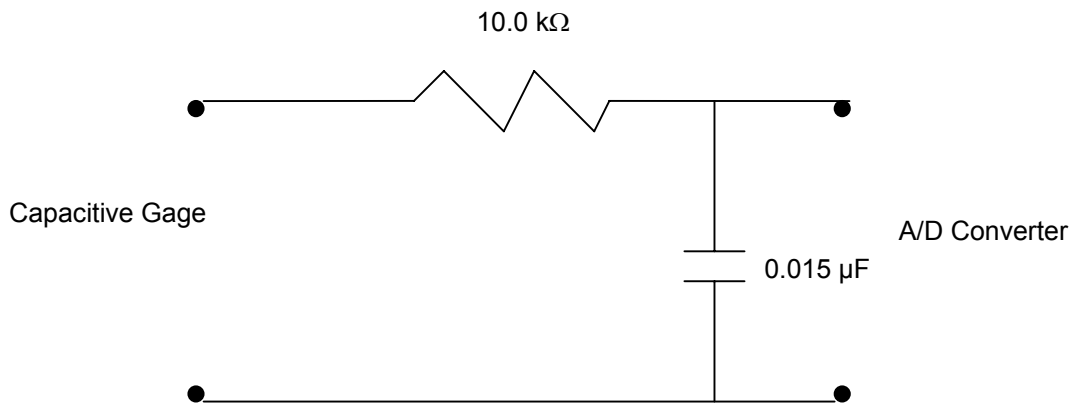
Figure 3-3: Schematic diagram of anti-aliasing filter

I modified the original circuits according to system bandwidth, output gain, the resistance and inductance of our coils. Figure 3-2 shows the Matlab simulation of the frequency response from the power amplifiers. The DC gain is 0.5 and the 3-dB bandwidth is 1440 Hz.
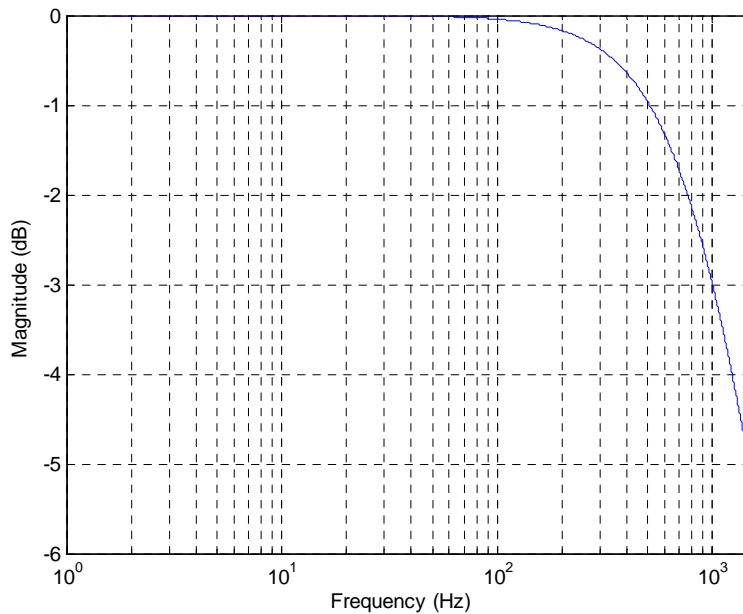
Figure 3-4: Frequency response of the anti-aliasing filter

An anti-aliasing filter was designed and placed before the input of A/D channels to prevent aliasing by sampling. The anti-aliasing filter is a first-order low-pass filter with the cut-off frequency at approximately 1000 Hz. The circuit diagram of this RC filter is shown in Figure 3-3. Figure 3-4 shows the frequency response of this anti-aliasing filter.

3.6 Sensors

3.6.1 Capacitance Sensors

Three capacitance sensors are used to measure the translation in the Z axis and rotation around the X and Y axes. Three ADE 2810 sensor probes are placed under the target—the bottom surface of the platen. The probe has a 10-mm diameter active sensing area. Its outer diameter and length are 20 mm and 18 mm, respectively. A thin wire is connected from the target to the chassis of ADE 3800 electronic board to provide electrical ground. We set the zero point between target and probe to be 500 μm. The minimum and maximum air gap are 250 μm and 750 μm. Limited by the six coils, the platen can not travel beyond this 500 μm travel range. These three sensor probes are then connected to ADE 3800 electronic boards. ADE 3800 electronic board converts the probe-to-target distance to voltage signal. It has a resolution of 3 nm and measurement range of 500 μm. The output range of ADE 3800 is originally ±10.0 V. By changing the jumpers, the output range can be set to ±5.0 V which matches our A/D convert input swing.

3.6.2 Laser Interferometer

Figure 3-5 shows the metrology arrangement of our laser interferometer system. The laser interferometer system consists of laser head, laser interferometer, laser bender,

laser splitter, laser receiver, plane mirrors, and laser axis board. The Agilent 5517D laser head has a HeNe laser source at 632-nm wavelength. It can measure the axis velocity up to 1 m/s. The resolution from the Agilent 10897B laser axis board is 0.6 nm. It gives 35-bit position data at a 10 MHz update rate. It also provides 24-bit velocity data. Pentek 4284 DSP reads the position measurement value from three laser axis boards through VME bus.

These three interferometers can give us 3-DOF information of the platen. They are translation in the X axis, translation in the Y axis and rotation around the Z axis.
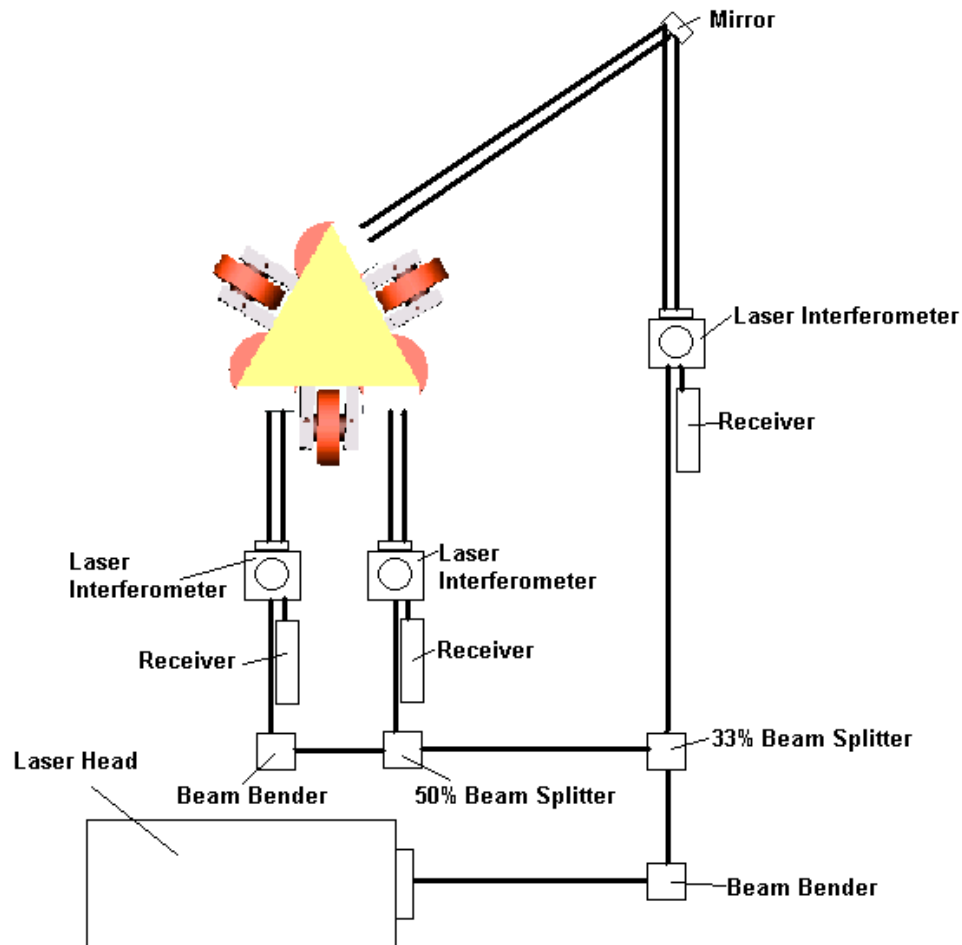
Figure 3-5: Laser interferometery metrology

3.7 Software

3.7.1 Control Routine

The control work includes two separate routines: real-time control in the DSP and user interface in the VME PC. The codes for the DSP were developed in ANSI-C standard language and the codes for the VME PC were developed in Visual C++. I developed these codes based on the skeleton in Kim's thesis [16].

The interrupt service routine (ISR) in the DSP part performs the following tasks:

1. Read all real-time measurement data from capacitance sensors and laser interferometers.

2. Do coordinate transformation to get current position information of our platen.

3. Execute controller to generate desired force.

4. Execute modal-decomposed force transformation.

5. Generate output signals to D/A channels.

6. Clear interrupt and come out from interrupt routine.

During the rest time between two interrupts, the DSP will do the tasks: (1) check if there is a command by VME PC and process that command transfer, (2) save the real-time data to dual-port RAM for display on the user interface.

User interface program is developed on the VMIC VME PC by Visual C++.net. It performs the following tasks: (1) show system information such as position values, measurement data, output currents, etc. on the screen, (2) send user's commands to DSP, (3) if issued, save data on the hard disk for further usage.

The information shown on the screen includes: (1) position variables of the platen, (2) velocity variables of the platen, (3) measurement values from laser interferometers and capacitance sensors, (4) position errors, (5) forces from six actuators, (6) currents through six coils.

The user commands to the DSP includes: (1) enable/disable interrupt, (2) enable/disable D/A output, (3) reset laser interferometers, (4) send desired position values to the DSP, (5) save data on hard disk.

3.7.2 Software List

Following are the software I used for programming:

- Texas Instruments (TI)' TMS320 C3x/C4x-Code Composer: It is used to compile and link the codes running in the Pentek 4284 DSP board. TI's Code Composer is running under Windows environment in the VME PC. With its MS-Visual C++ like environment, Code Composer can edit, build, profile and manage projects developed in C language. After the codes are built up, Code Composer can download them into Pentek 4284 DSP board and run them or debug them in DSP.

- Pentek's Swiftnet: It is a control panel for communication before VME PC and DSP. It can realize byte swapping. It must be running at background when operating DSP.

- VMIC's IOworks: It provides tools to access VMEbus from the VME PC. By using it, we can easily read or write into the memory location in Pentek DSP, the laser axis boards and Pentek 6102 A/D and D/A converters. It also offers a library which can be included in our C codes to access the VMEbus.

- Microsoft Visual C++.net: It is used to develop the user interface program. With the advantages of Windows developing environment and object-oriented programming method, Visual C++ may be the best option for user interface development.

Figure 3-6 is the user interface displayed on the VME PC screen.

Figure 3-6: User interface displayed on the VME PC screen

CHAPTER IV
DYNAMIC MODELING AND CONTROL SYSTEM DESIGN

In this chapter, the dynamics and control of our maglev system are presented. Dynamic analysis and modeling are prerequisite for the realization of control system. The first section gives a dynamic model of the moving part. Some system parameters are shown in this section. Section 4.2 gives the sensor equations that are necessary for system positioning. Force allocation is given in Section 4.3. Force allocation is used to assign forces to six actuators for control. Control system designs for vertical motion and horizontal motion are presented in Section 4.4. The test results are given in Section 4.5

4.1 Dynamic Model and System Parameters

The moving part of the system is modeled as a pure mass because there is no friction in this maglev system. Since the damping layer can be modeled as a spring and dashpot and the single-axis actuators have negative spring constants as well, a more precise model can be a mass-spring-dashpot structure. At this moment, I use the pure mass model to design the control system. Research on a more precise model is being done by Amit Pandey, another graduate student in our lab.

The total mass of the moving part which includes the platen, mirrors, vertical magnets, horizontal magnets, cover layer, damping layer, constraint layer, spacers, and screws is measured to be 0.2126 kg. Therefore, for translation, the system is represented by the differential equation in (4.1).

$$0.2126\frac{d^2x}{dt^2} = f \qquad (4.1)$$

For vertical motion, f refers to the actuator forces subtracted by the platen weight.

Then, the system transfer function is

$$\frac{x(s)}{f(s)} = \frac{1}{0.2126s^2}.$$

(4.2)

For rotation, the system is represented by the differential equation in (4.3). *I* refers to the moment of inertia around the corresponding axis. *T* refers to torque around that axis.

$$I\frac{d^2\theta}{dt^2} = T.$$

(4.3)

Then, the system transfer function is

$$\frac{\theta(s)}{T(s)} = \frac{1}{Is^2}.$$

(4.4)

The system model was built by using Solidworks. After properly assigning materials to all parts of the platen, Solidworks can calculate the moments of inertia taken at the center of mass:

$$I = \begin{bmatrix} I_{xx} & I_{xy} & I_{xz} \\ I_{yx} & I_{yy} & I_{yz} \\ I_{zx} & I_{zy} & I_{zz} \end{bmatrix} = \begin{bmatrix} 0.00013288 & 0.00000314 & 0 \\ 0.00000314 & 0.00012228 & 0 \\ 0 & 0 & 0.00023587 \end{bmatrix} \text{ in kg-m}^2.$$

(4.5)

The definition of each axis is shown in Figure 4.1.

4.2 Sensor Equations

After getting the measurement data from sensors, we need do a transformation to obtain the position information of the center of mass (CM). This transformation comes from the sensor equations. Figure 4-2 shows the definitions of some variables and the numbering of mirrors and sensor probes.
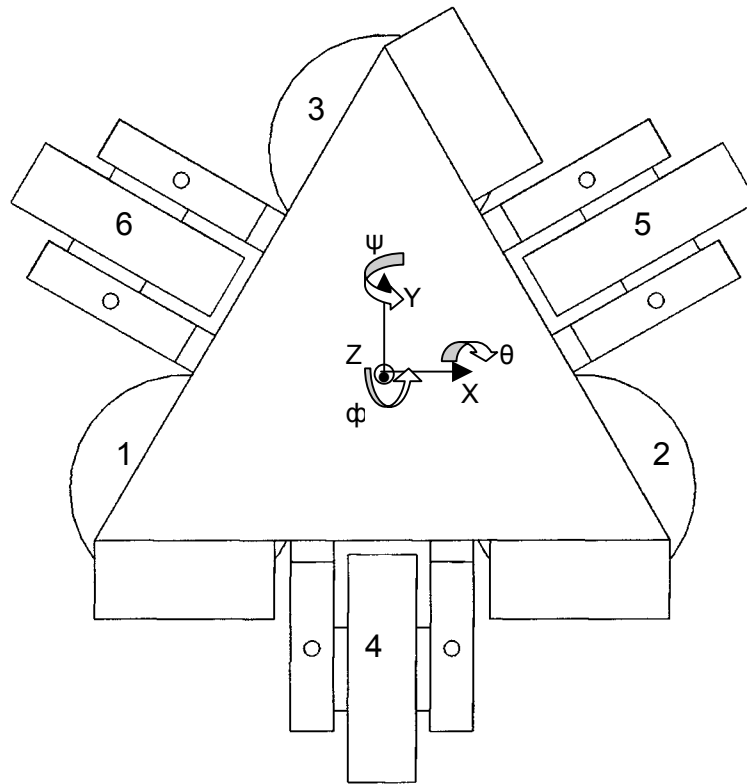

Figure 4-1: Axis definition and actuator numbering

The following is a list of the variables used in sensor equations.

Y_1: distance in the X axis from the CM to the surface of mirror 1

Y_2: distance in the X axis from the CM to the surface of mirror 2

X_1: distance in the Y axis from the CM to the surface of mirror 3

Z_{x1}: distance in the X axis from the CM to the center of capacitance sensor probe 1

Z_{y1}: distance in the Y axis from the CM to the center of capacitance sensor probe 1

Z_{x2}: distance in the X axis from the CM to the center of capacitance sensor probe 2

Z_{y2}: distance in the Y axis from the CM to the center of capacitance sensor probe 2

Z_{x3}: distance in the X axis from the CM to the center of capacitance sensor probe 3

Z_{y3}: distance in the Y axis from the CM to the center of capacitance sensor probe 3

x: displacement of the CM in the X axis

y: displacement of the CM in the Y axis

z: displacement of the CM in the Z axis

ψ: angle around the X axis

θ: angle around the Y axis

ϕ: angle around the Z axis

u: velocity of the CM in the X axis

v: velocity of the CM in the Y axis

r: angular velocity of the CM around z axis

y_1: displacement in the Y axis of the surface of mirror 1; It is the measurement from laser interferometer 1

y_2: displacement in the Y axis of the surface of mirror 2; It is the measurement from laser interferometer 2

x_1: displacement in the X axis of the surface of mirror 3; It is the measurement from laser interferometer 3

u_1: velocity in the Y axis on mirror surface 1; It is the velocity measurement from laser interferometer 1

u_2: velocity in the Y axis on mirror surface 2; It is the velocity measurement from laser interferometer 2

v_1: velocity in the X axis on mirror surface 3; It is the velocity measurement from laser interferometer 3

z_1:   the actual measurement from capacitance probe 1

z_2:   the actual measurement from capacitance probe 2

z_3: the actual measurement from capacitance probe 3

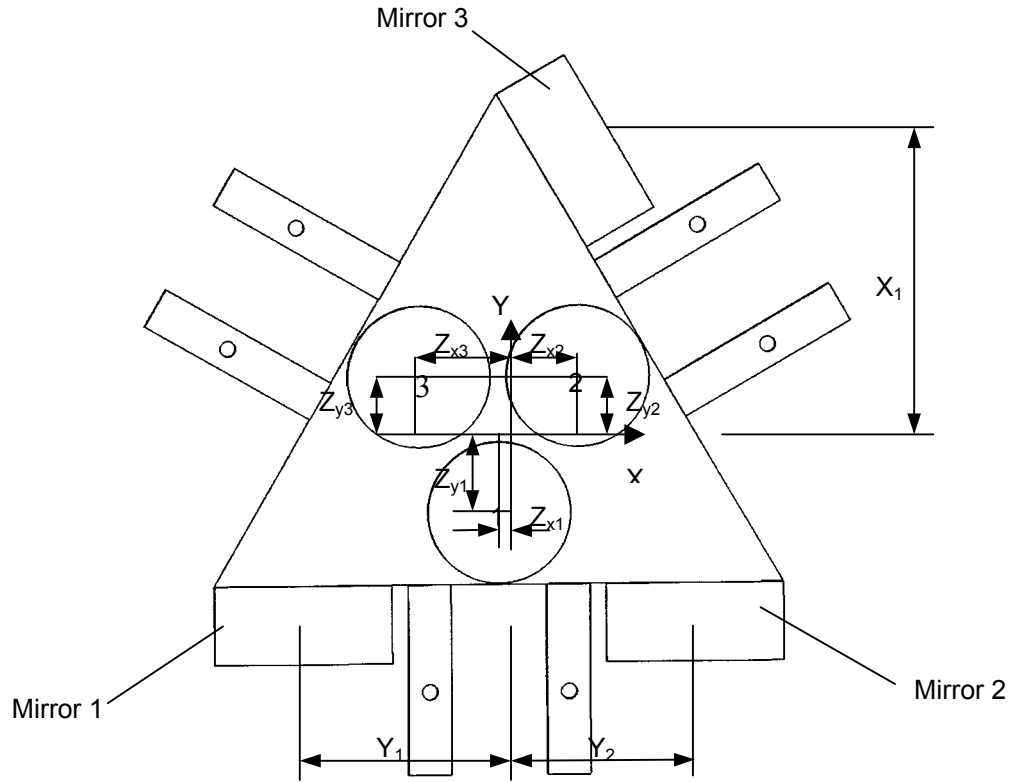Figure 4-2: Definitions of variables and numbering of mirrors and sensors

By geometric analysis, we get the following relationship between the measurement value and position value at center of mass.

$$y_1 = y - Y_1 \cdot \phi \tag{4.6}$$

$$y_2 = y + Y_2 \cdot \phi \tag{4.7}$$

$$x_1 = -x \cdot \cos\ 30^\circ - y \cdot \cos\ 60^\circ + X_1 \cdot \phi \tag{4.8}$$

$$u_1 = u - Y_1 \cdot r \tag{4.9}$$

$$u_2 = u + Y_2 \cdot r \qquad (4.10)$$

$$v_1 = v - X_1 \cdot r \qquad (4.11)$$

$$z_1 = z - Z_{y1} \cdot \psi + Z_{x1} \cdot \theta \qquad (4.12)$$

$$z_2 = z + Z_{y2} \cdot \psi - Z_{x2} \cdot \theta \qquad (4.13)$$

$$z_3 = z + Z_{y3} \cdot \psi + Z_{x3} \cdot \theta \qquad (4.14)$$

We can rewrite the above equations into a matrix:

$$
\begin{bmatrix} y_1 \\ y_2 \\ x_1 \\ u_1 \\ u_2 \\ v_1 \\ z_1 \\ z_2 \\ z_3 \end{bmatrix}
=
\begin{bmatrix}
1 & 0 & -Y_1 & 0 & 0 & 0 & 0 & 0 & 0 \\
1 & 0 & Y_2 & 0 & 0 & 0 & 0 & 0 & 0 \\
-\cos 60^\circ & -\cos 30^\circ & X_1 & 0 & 0 & 0 & 0 & 0 & 0 \\
0 & 0 & 0 & 1 & 0 & -Y_1 & 0 & 0 & 0 \\
0 & 0 & 0 & 1 & 0 & Y_2 & 0 & 0 & 0 \\
0 & 0 & 0 & 0 & 1 & -X_1 & 0 & 0 & 0 \\
0 & 0 & 0 & 0 & 0 & 0 & -Z_{y1} & Z_{x1} & 1 \\
0 & 0 & 0 & 0 & 0 & 0 & Z_{y2} & -Z_{x2} & 1 \\
0 & 0 & 0 & 0 & 0 & 0 & Z_{y3} & Z_{x3} & 1
\end{bmatrix}
\begin{bmatrix} y \\ x \\ \phi \\ u \\ v \\ r \\ \psi \\ \theta \\ z \end{bmatrix}
\qquad (4.15)
$$

4.3 Force Allocation

By combining forces from six actuators, we can generate 6-DOF motion to the platen. Again, we need align the forces to the coordinate axes.

The definition of variables used in this section is given as follows:

f_1: force generated by actuator 1

f_2: force generated by actuator 2

f_3: force generated by actuator 3

f_4: force generated by actuator 4

f_5: force generated by actuator 5

f_6: force generated by actuator 6

f_x: total force in the X axis

f_y: total force in the Y axis

f_z: total force in the Z axis

τ_x: torque around the X axis

τ_y: torque around the Y axis

τ_z: torque around the Z axis

l_{1x}: distance in the X axis from actuator 1 to the Y axis;

l_{1y}: distance in the Y axis from actuator 1 to the X axis;

l_{2x}: distance in the X axis from actuator 2 to the Y axis;

l_{2y}: distance in the Y axis from actuator 2 to the X axis;

l_{3x}: distance in the X axis from actuator 3 to the Y axis;

l_{3y}: distance in the Y axis from actuator 3 to the X axis;

l_{1z}: distance from actuator 4 to the Z axis;

l_{2z}: distance from actuator 5 to the Z axis;

l_{3z}: distance from actuator 6 to the Z axis;

The six actuators are numbered in Figure 4-1. Since the horizontal actuators are located close to the X-Y plane, the coupling between vertical forces and horizontal forces is ignored. The equations for force allocation are:

$$f_z = f_1 + f_2 + f_3 \tag{4.16}$$

$$\tau_y = f_1 \cdot l_{1x} - f_2 \cdot l_{2x} + f_3 \cdot l_{3x} \tag{4.17}$$

$$\tau_x = -f_1 \cdot l_{1y} - f_2 \cdot l_{2y} + f_3 \cdot l_{3y} \tag{4.18}$$

$$f_x = f_4 - \cos\ 60^\circ \cdot f_5 - \cos\ 60^\circ \cdot f_6 \tag{4.19}$$

$$f_y = \cos\ 30^\circ \cdot f_5 - \cos\ 30^\circ \cdot f_6 \tag{4.20}$$

$$\tau_z = f_4 \cdot l_{4z} + f_5 \cdot l_{5z} + f_6 \cdot l_{6z} \tag{4.21}$$

The matrix of force allocation is shown below:

$$
\begin{bmatrix} f_z \\ \tau_y \\ \tau_x \\ f_x \\ f_y \\ \tau_z \end{bmatrix} = \begin{bmatrix} 1 & 1 & 1 & 0 & 0 & 0 \\ l_{1x} & -l_{2x} & l_{3x} & 0 & 0 & 0 \\ -l_{1y} & -l_{2y} & l_{3y} & 0 & 0 & 0 \\ 0 & 0 & 0 & 1 & -\cos 60^\circ & -\cos 60^\circ \\ 0 & 0 & 0 & 0 & \cos 30^\circ & -\cos 30^\circ \\ 0 & 0 & 0 & l_{4z} & l_{5z} & l_{6z} \end{bmatrix} \begin{bmatrix} f_1 \\ f_2 \\ f_3 \\ f_4 \\ f_5 \\ f_6 \end{bmatrix}
\qquad (4.22)
$$

The zeros in the top right corner and bottom left corner reveal decoupling between vertical actuators and horizontal actuators which was intended in our design. Actually, since the horizontal actuators are not exactly located at the same plane of the CM, small coupling still exists. For a better controller design, we need to correct this coupling.

4.4 Control System Design

Several steps were taken to implement the six-axis control to our platen. They are:(1) Develop and implement controller to vertical translation in the Z axis. (2) Extend control to all three-axis motions in vertical direction. (3) Add three horizontal controller for translation in the X,Y axis and rotation around the Z axis.

4.4.1 Vertical Control

Initially, tapes are used to confine the other five axes motion. The horizontal actuator has zero output. The average of the measurement from the three capacitance sensors are used for the position in the Z axis.

As derived in section 4.1, the dynamic equation of the Z translation is:

$$0.2126\frac{d^2z}{dt^2} = f_z$$ (4.23)

f_z is the sum of forces in the Z axis which includes the forces from three vertical actuators and weight.

A continuous-time lead-lag controller is designed by using MATLAB root locus routines. The damping ratio ζ is chosen as 0.7 and phase margin is 50° at the crossover frequency $w_c = 48$ Hz. Equation (4.24) shows the lead-lag compensator for the desired damping and stiffness of the system:

$$G_z(s) = \frac{6.7897 \times 10^4 (s+130)(s+8)}{s(s+1130)}$$ (4.24)

The presence of a pole at the origin is to obtain zero steady-state error. By using zero-order hold method with a 5-kHz sampling rate, this continuous model is converted to a discrete-time model which is

$$G_z(z) = \frac{6.7897 \times 10^4 (z-0.9769)(z-0.9984)}{(z-1)(z-0.7977)}$$ (4.25)

Figure 4-3 shows the control diagram for z-axis motion. Figures 4-4 and 4-5 show the loop transmission and closed-loop Bode plot for the z-axis motion.
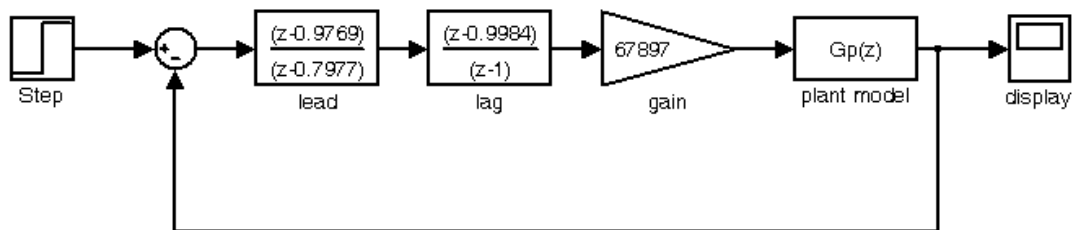

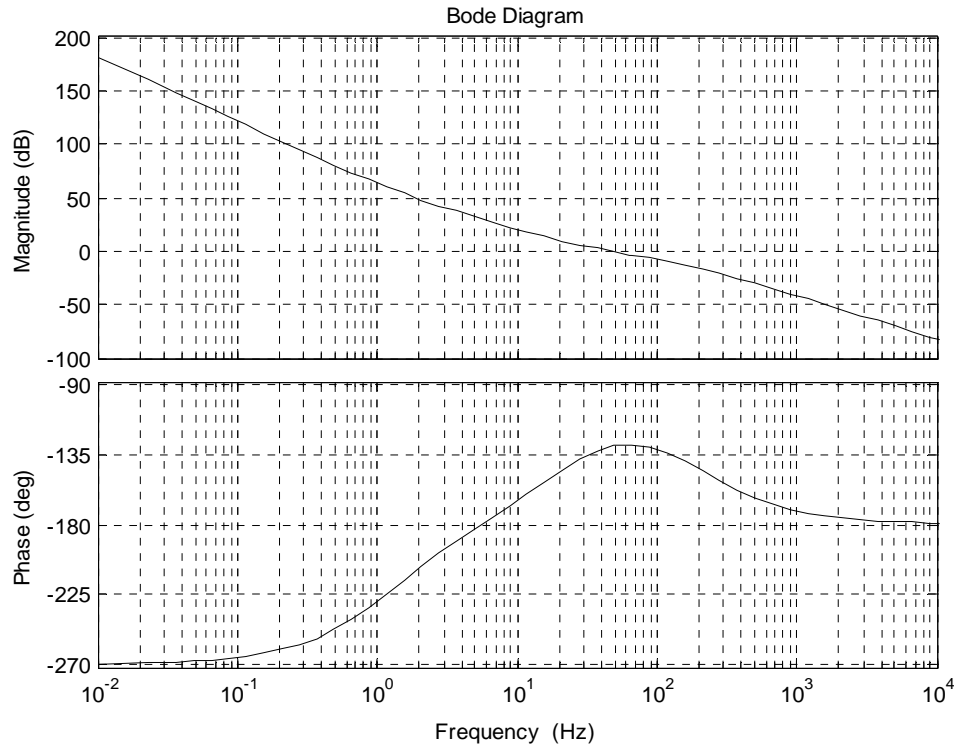Figure 4-3: Control diagram for z-axis motion

Figure 4-4: Loop transmission for z-axis motion
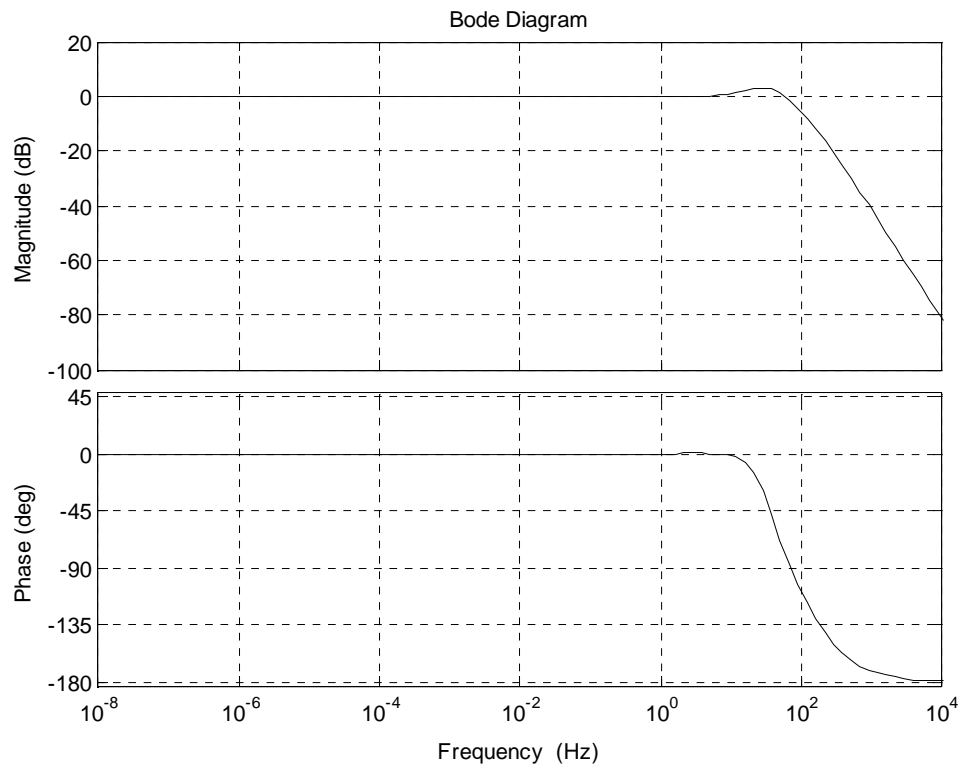
Figure 4-5: Closed-loop Bode plot

After closing the loop for z-axis motion, the other two control loops θ and ψ for vertical motions can be closed in the same way. The design of the controllers is similar to that of the z-axis except that the gain is changed according to the moments of inertia in the X axis and the Y axis ($I_{xx} = 0.00013288$ Kg·m^2 and $I_{yy} = 0.00012228$ Kg·m^2). The dynamic equations for θ and ψ are:

$$I_{xx} \frac{d^2\theta}{dt^2} = \tau_x \qquad (4.26)$$

and

$$I_{yy} \frac{d^2\psi}{dt^2} = \tau_y \qquad (4.27)$$

The desired model forces are resolved into the decomposed forces by equation (4-22). Then the controllers for θ and ψ are:

$$G_\theta(z) = \frac{42.4377(z - 0.9769)(z - 0.9984)}{(z - 1)(z - 0.7977)} \qquad (4.28)$$

and

$$G_\psi(z) = \frac{39.0524(z - 0.9769)(z - 0.9984)}{(z - 1)(z - 0.7977)} \qquad (4.29)$$

Figure 4-6 shows a 100-μm step response for z-axis motion with single controller only in the Z axis. Since there are no control in other axes, large disturbance exists. Figure 4-7 shows a step response with 3-DOF controllers in vertical motion, the disturbance has been greatly reduced.
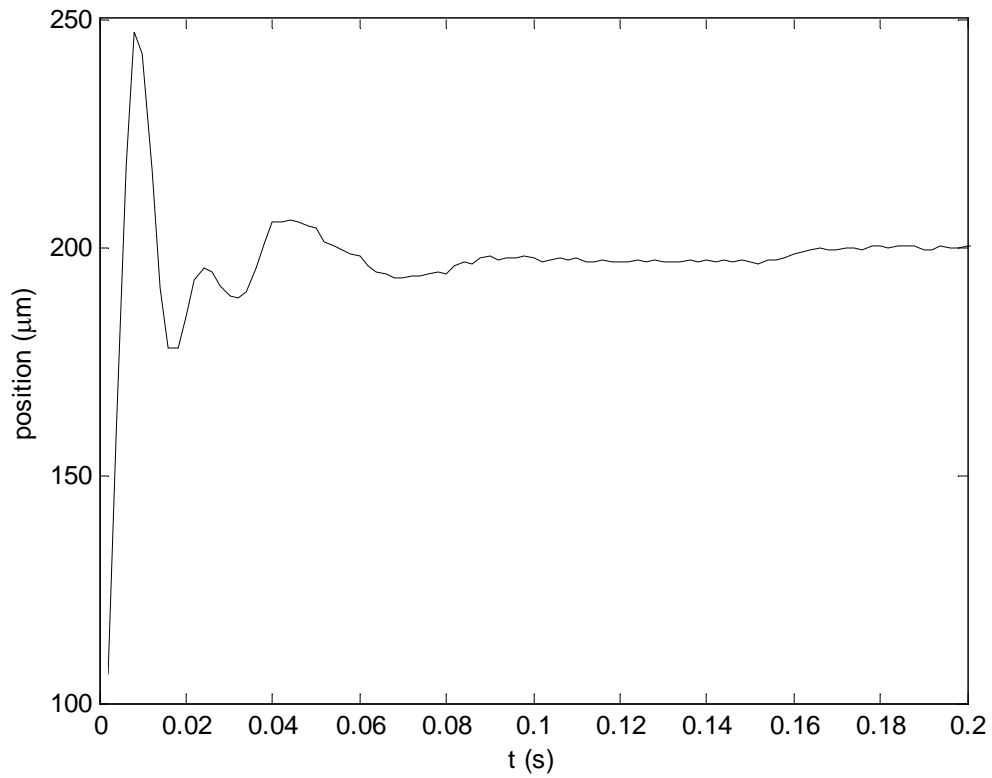
Figure 4-6: 100-micron step response in Z with controller in only Z

4.4.2 Lateral Control

Similarly to the vertical motion, the dynamics equations for the 3-DOF motions are:

$$0.2126\frac{d^2x}{dt^2} = f_x \tag{4.30}$$

$$0.2126\frac{d^2y}{dt^2} = f_y \tag{4.31}$$

$$I_{zz}\frac{d^2\phi}{dt^2} = \tau_z \tag{4.32}$$
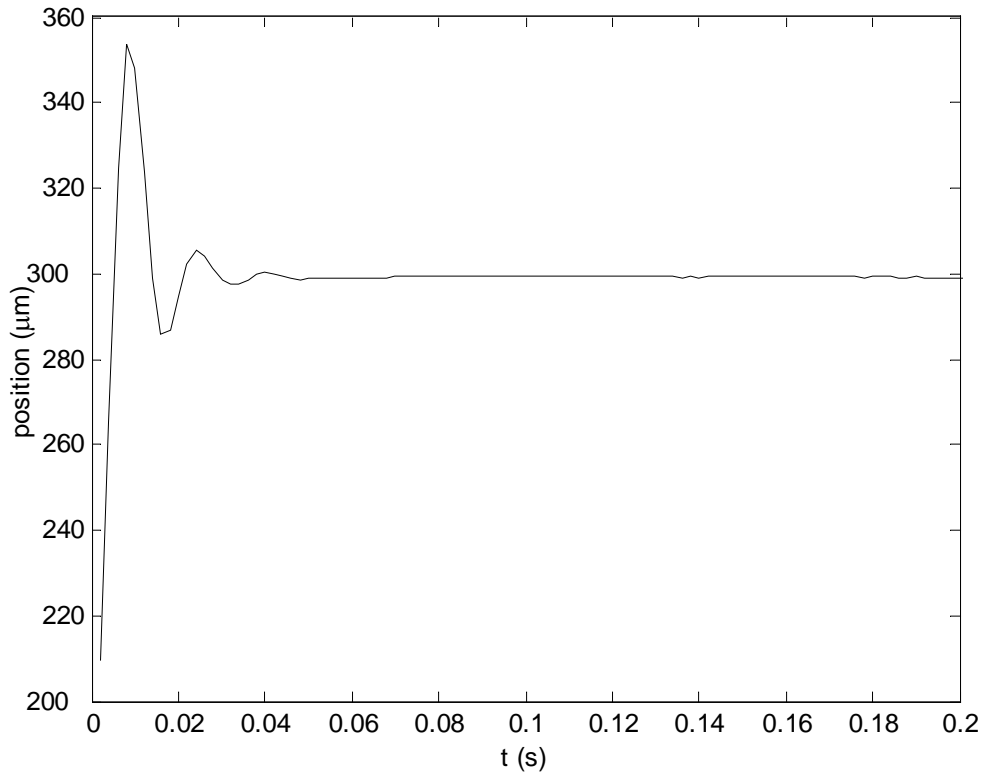
Figure 4-7: 100-micron step response in Z with controllers in three vertical axes

where $I_{zz} = 0.00023587 \quad \text{kg·m}^2$.

Similar controllers are designed for x, y and ф.

$$G_x(z) = \frac{6.7897 \times 10^4 (z - 0.9769)(z - 0.9984)}{(z - 1)(z - 0.7977)} \tag{4.33}$$

$$G_y(z) = \frac{6.7897 \times 10^4 (z - 0.9769)(z - 0.9984)}{(z - 1)(z - 0.7977)} \tag{4.34}$$

$$G_\phi(z) = \frac{75.329(z - 0.9769)(z - 0.9984)}{(z - 1)(z - 0.7977)} \tag{4.35}$$

The next section presents the test results of the 6-DOF motion under controllers in all six axes.

4.5 Test Results

Figures 4-8−4-13 shows the step responses in six axes. Figures 4-14−4-19 shows the position noise in six axes when the platen is levitated. The peak-to-peak noise in the X and Y axes is about 15 nm which corresponds to 2.5 nm rms. The peak-to-peak noise in the Z axis is about 150 nm which corresponds to 25 nm rms. This difference in noise level comes from the different sensors used in the lateral motion and the vertical motion. Detailed analysis to the noise propagation is given in the next chapter.

Figures 4-20−4-21 give the FFT of the noise in the X axis and noise in the Z axis. In FFT of the X axis, we see some peaks at 3 Hz and 18 Hz. We consider this noise as disturbance force from the floor vibration because the test by using accelerometer on the floor shows a strong 18-Hz noise from the lab floor. In FFT of the Z axis, we see some peaks at 18 Hz, 33 Hz, and 84 Hz. The 18-Hz noise comes from the floor vibration while the 33 Hz and 84 Hz may be electrical noise from sensors or power supply. We are currently designing a digital filter to get rid of the electrical noise in our system. As time is limited, the design of digital filter is not included in this thesis. A journal paper will be published to include our further research on the noise reduction.
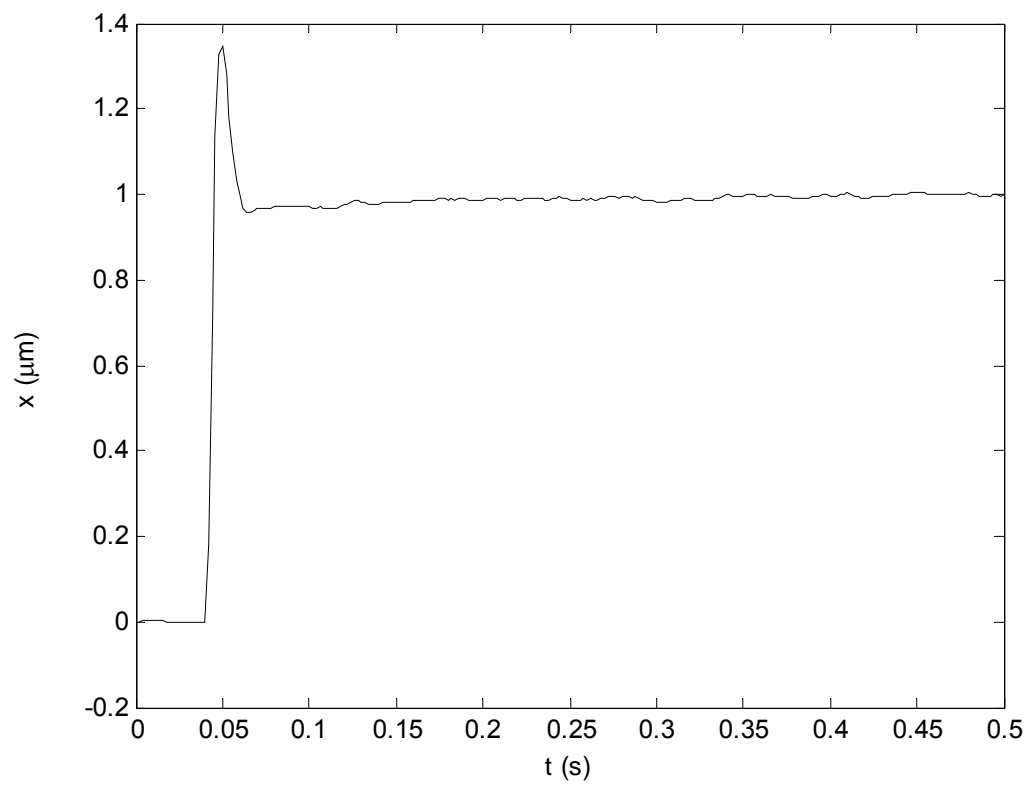
Figure 4-8: 1-μm step response in X
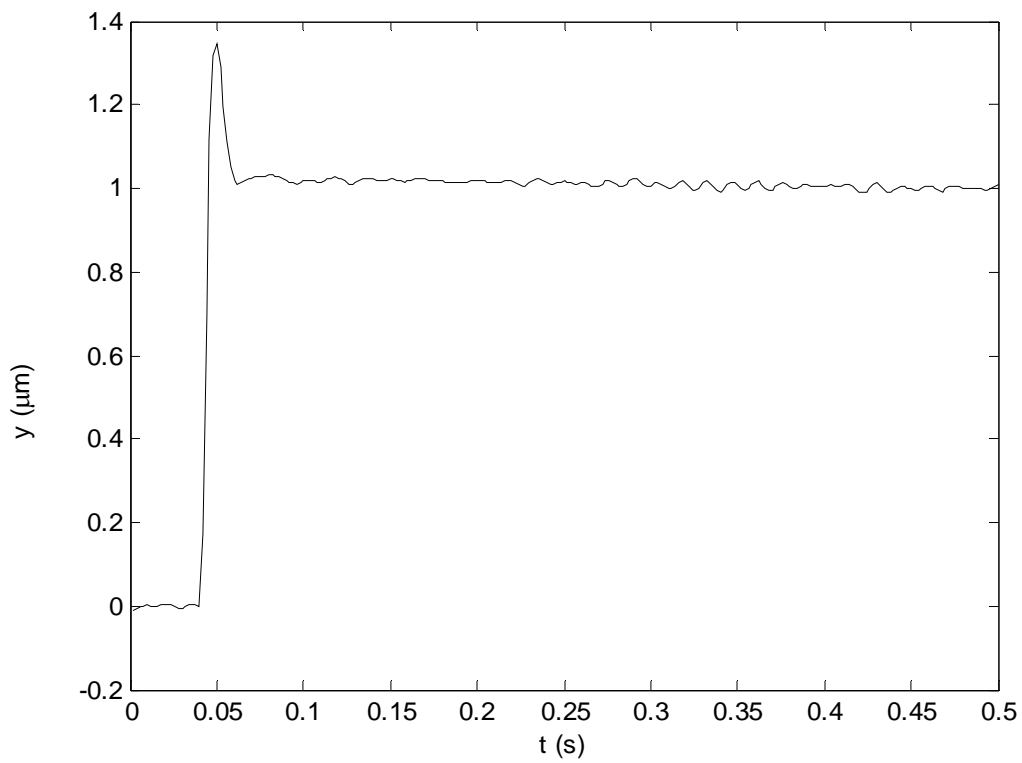
Figure 4-9: 1-μm step response in Y
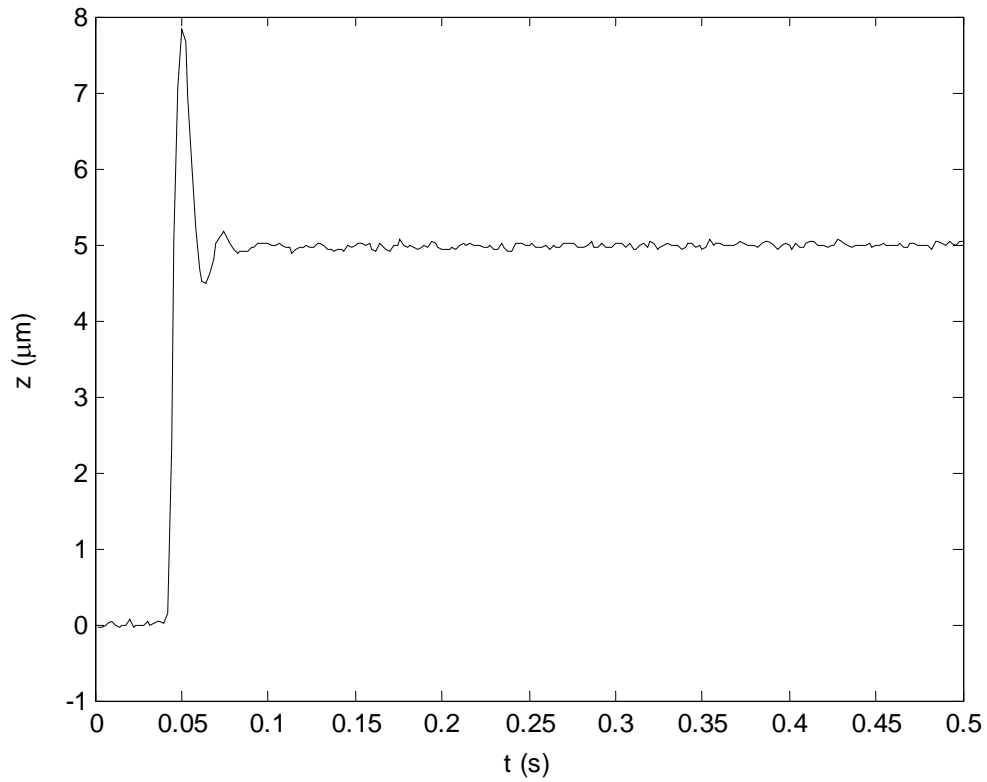
Figure 4-10: 5-µm step response in Z
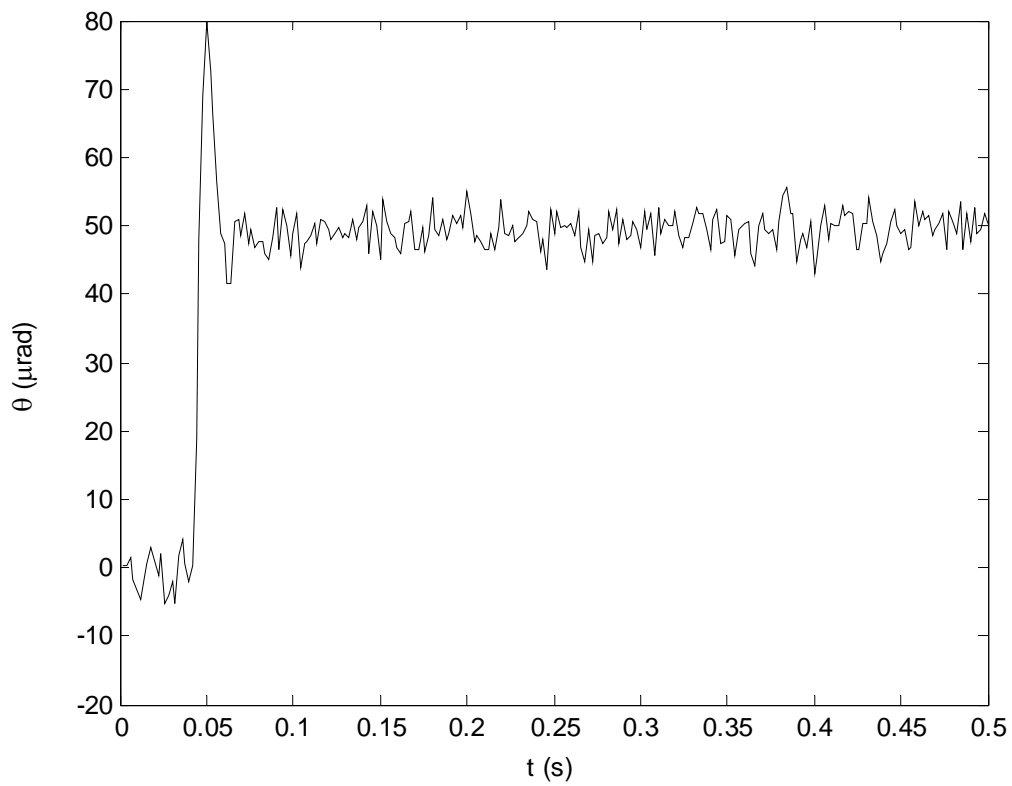
Figure 4-11: 50-µrad step response in θ
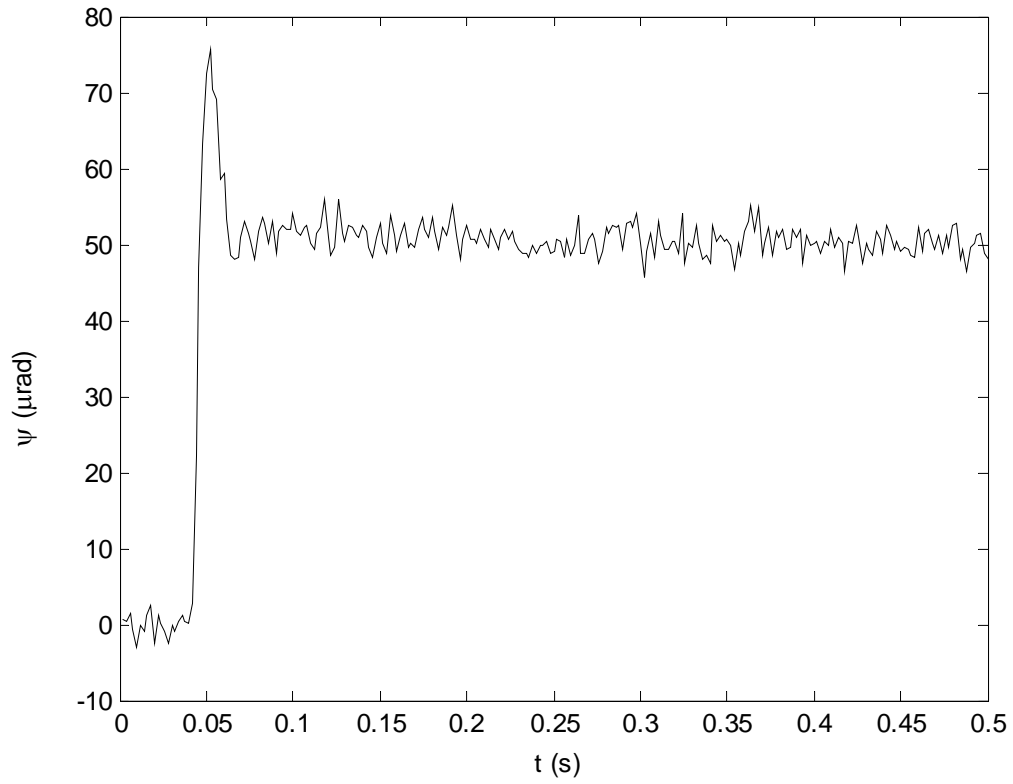
Figure 4-12: 50-μrad step response in ψ
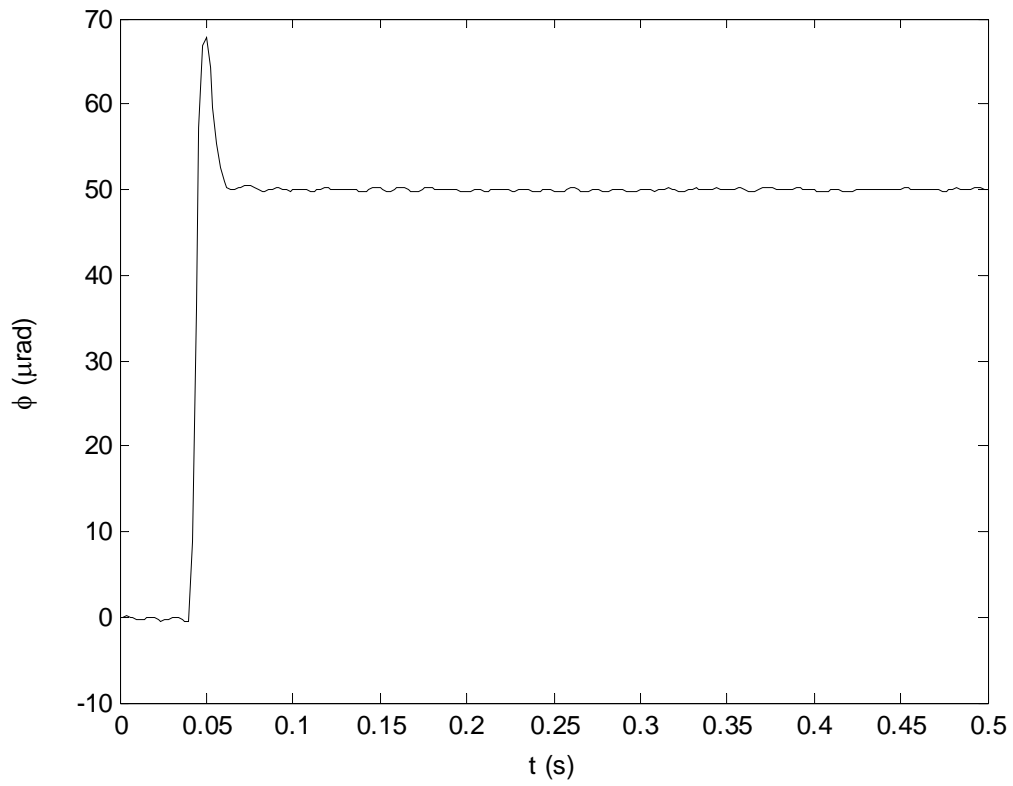
Figure 4-13: 50-μrad step response in φ
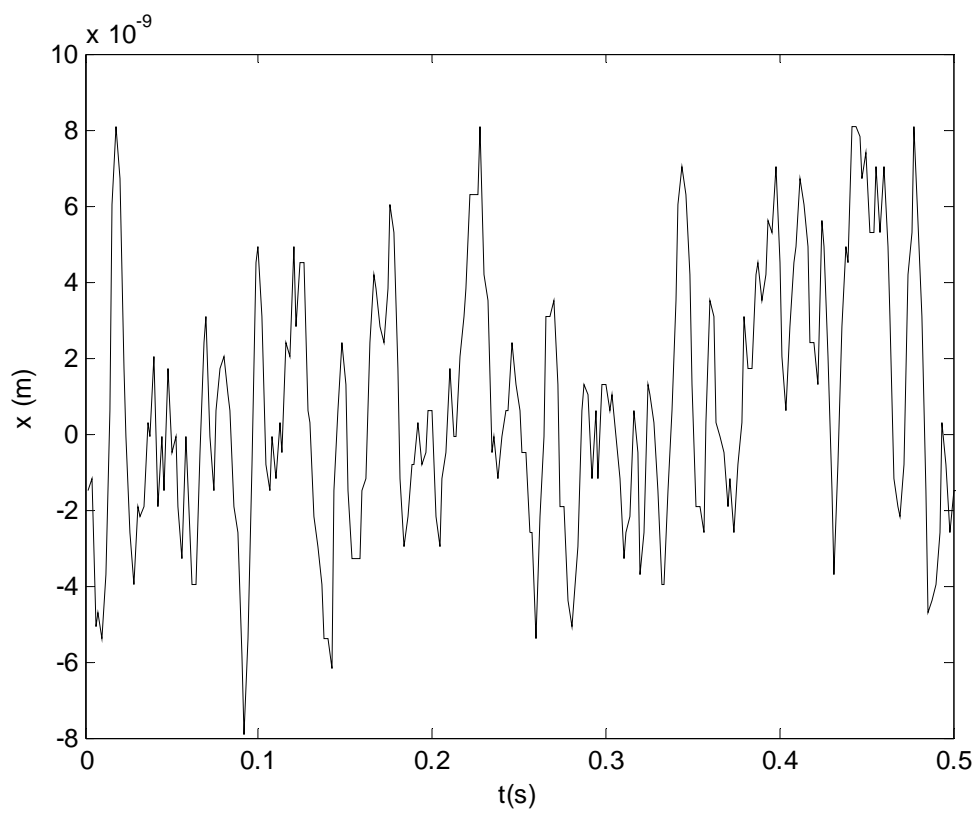
Figure 4-14: Noise level in X
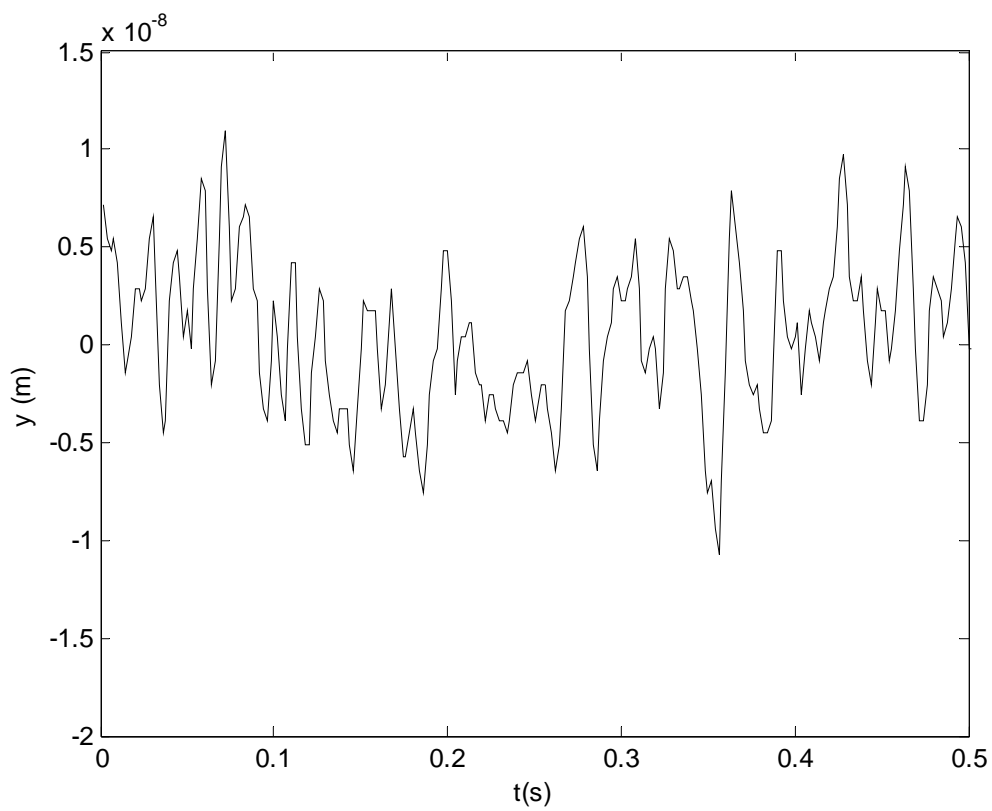
Figure 4-15: Noise level in Y
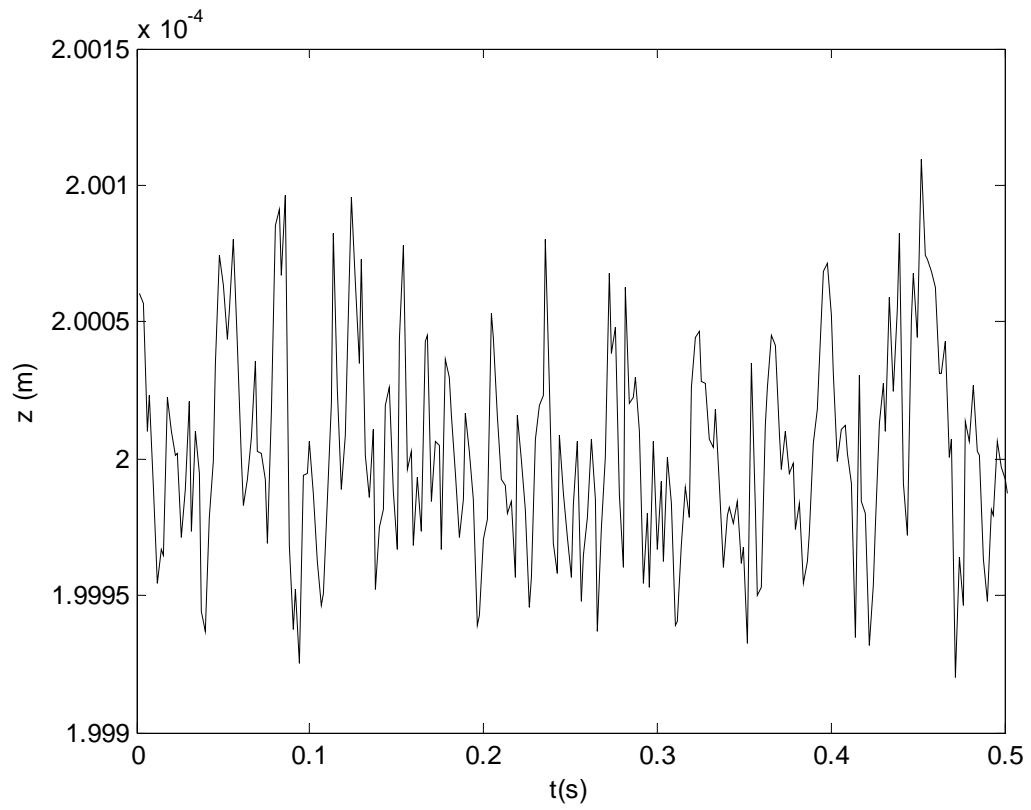
Figure 4-16: Noise level in Z
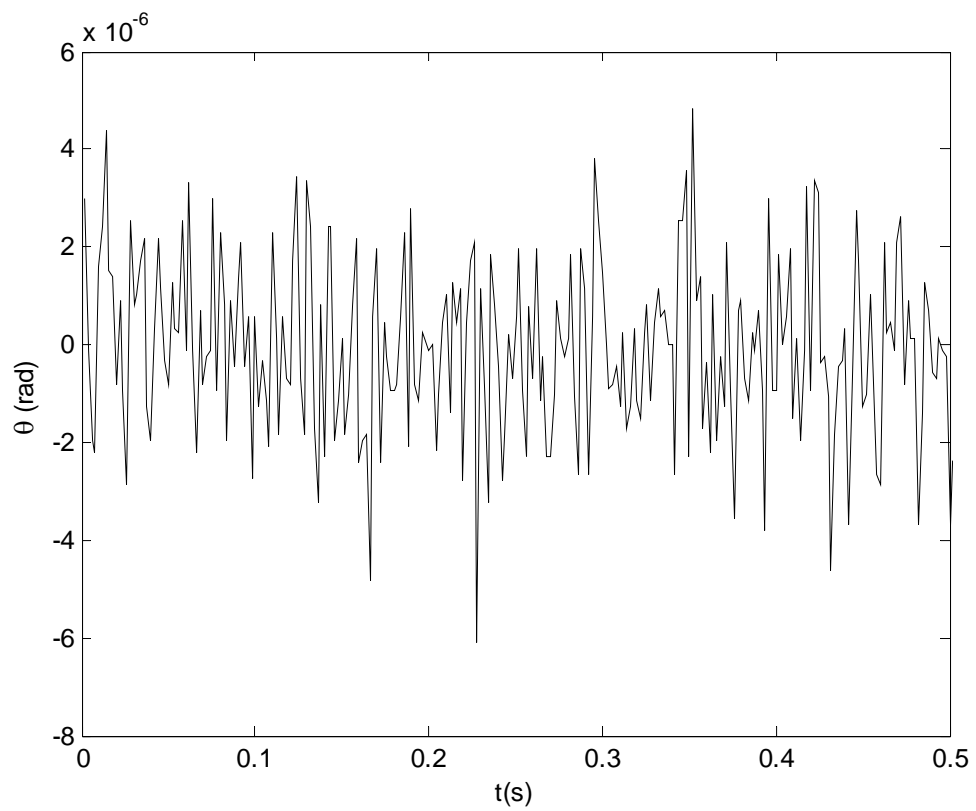
Figure 4-17: Noise level in θ
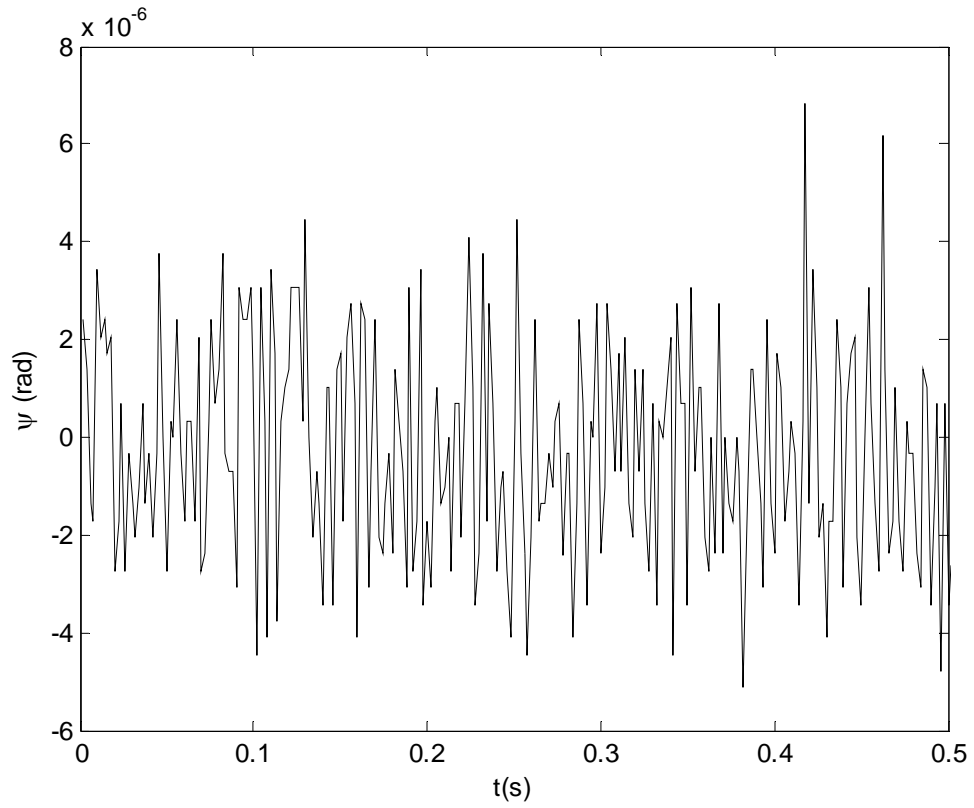
Figure 4-18: Noise level in ψ
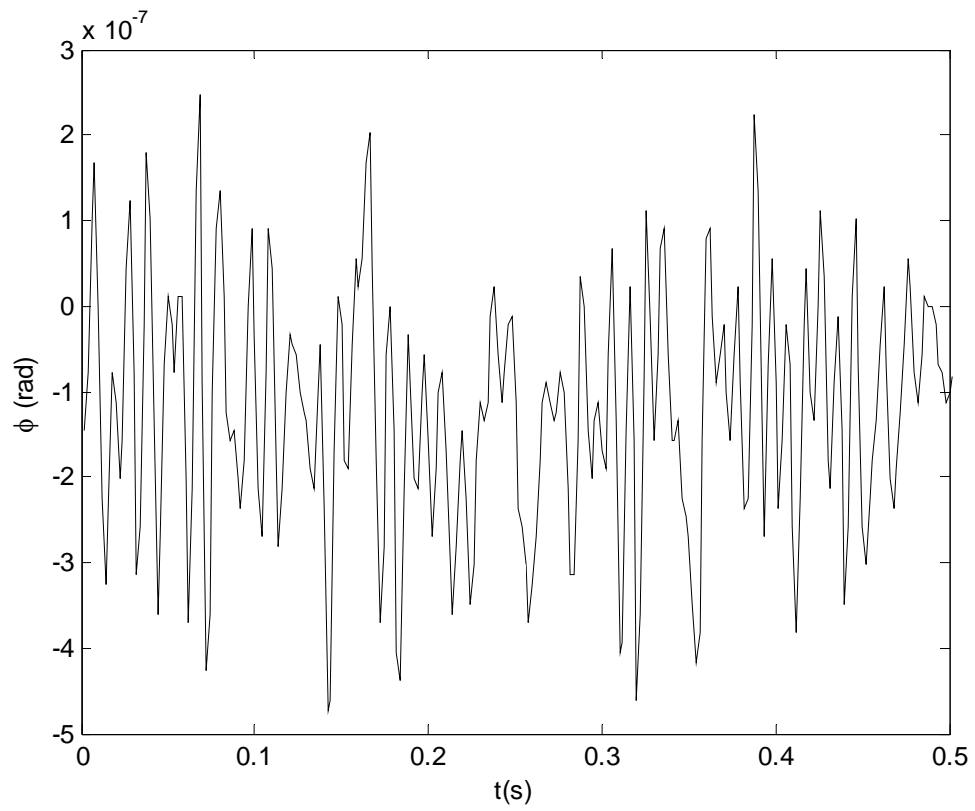
Figure 4-19: Noise level in φ
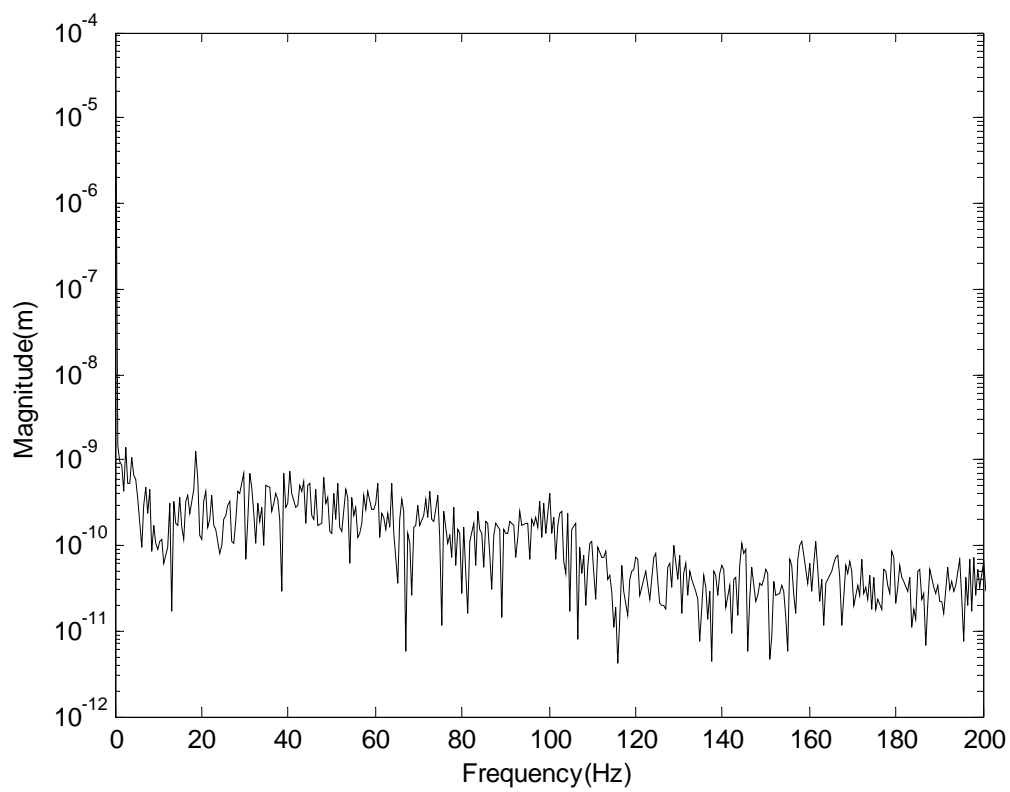
Figure 4-20: FFT of the noise in X
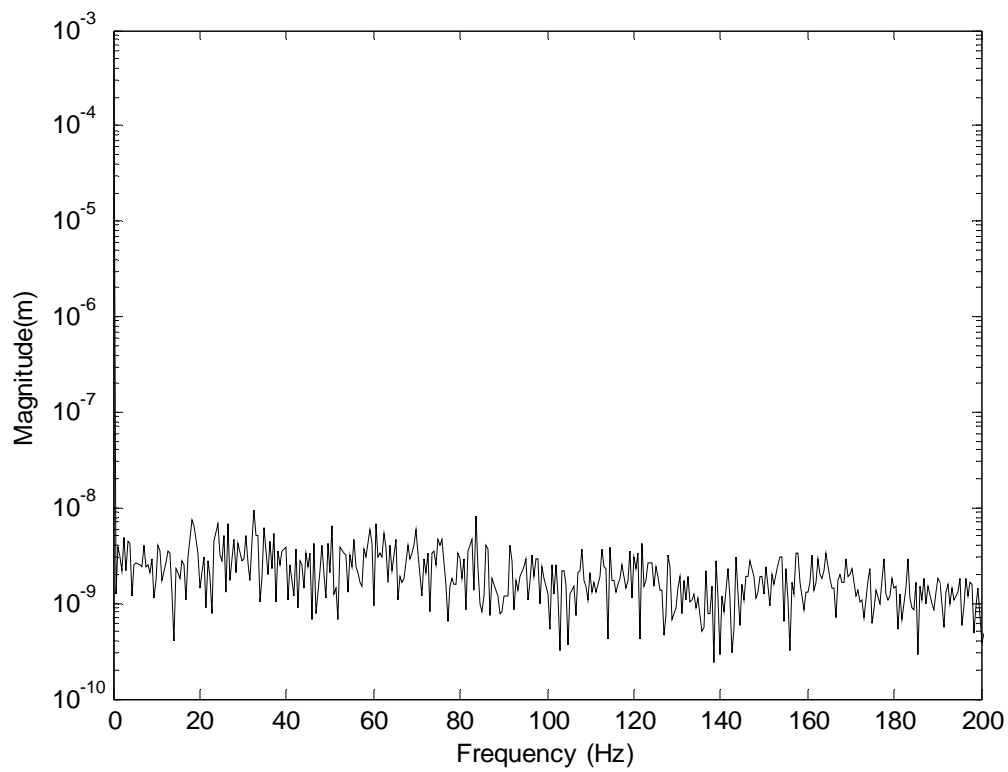
Figure 4-21: FFT of the noise in Z

CHAPTER V
SIGNAL ANALYSIS WITH STOCHASTIC NOISE/DISTURBANCE MODELING

The positioning capability is largely influenced by the noise performance of the mechatronics system. Generally, the noise sources include analog to digital quantization, electronics noise, floor vibration, etc. After amplified by the controller, each noise source has a different contribution to the final positioning noise level. Since all noises are considered as random signals, a stochastic method is used to model and predict the noise effects. Ludwick provides a very good reference for noise propagation and analysis for the precision positioning device [27].

In the first section of this chapter, an introduction of stochastic characteristics in random signal processing is provided. The noise propagation and analysis in X axis motion and Z axis motion is given in Section 5.2 and Section 5.3. Within these two sections, each noise source is analyzed by using stochastic noise modeling. Combination of each noise effects gives the final result of the noise distribution.

5.1 Introduction to Stochastics in Random Signal Processing

We first define the expected value of a waveform, or the mean value of a waveform,

$$\mu_x = \lim_{T \to \infty} \frac{1}{2T} \int_{-T}^{T} x(t) \; dt \, . \qquad (5.1)$$

Then we define the spread of the waveform about a mean value. It can be represented by variance, which is

$$\sigma_x^2 = \lim_{T \to \infty} \frac{1}{2T} \int_{-T}^{T} (x(t) - \mu_x)^2 \, dt. \tag{5.2}$$

Another measure for spread of the waveform is the mean squared value of a waveform, given by

$$<x^2(t)> = \lim_{T \to \infty} \int_{-T}^{T} x^2(t) \, dt. \tag{5.3}$$

It is easy to find that the mean square value is same as the variance if the mean of the waveform is zero.

The autocorrelation function is a measure of the relation of the samples at two different times. It is defined as

$$R_x(\tau) \equiv <x(t)x(t-\tau)> = \lim_{T \to \infty} \frac{1}{2T} \int_{-T}^{T} x(t)x(t-\tau) \, dt. \tag{5.4}$$

The value of autocorrelation function at $\tau = 0$ is the mean squared value of the waveform.

The Fourier transform of the autocorrelation function is known as the spectral density of the waveform

$$S_x(\omega) = \int_{-\infty}^{\infty} R_x(\tau) \, e^{-j\omega\tau} \, d\tau. \tag{5.5}$$

If a signal $x(t)$ is passed through a linear system with an impulse response $h(t)$, and the output waveform is $y(t)$, by taking the spectral density of the input signal and output signal, we can get the relationship,

$$S_y(\omega) = |H(\omega)|^2 S_x(\omega). \tag{5.6}$$

As a summary, if the spectral density of an input waveform $S_x(\omega)$ is measured by experiments or is obtained from instrument manuals, and the system transfer function is known, the spectral density of the output waveform can be predicted by using (5.6). Also in case of zero mean waveform, variance has the same value as autocorrelation function at $\tau = 0$. By taking the inverse Fourier transform of the waveform, we can obtain the autocorrelation. Therefore the variance of the output waveform can be obtained by using the inverse Fourier transform of output spectral density,

$$\sigma_y^2 = \frac{1}{2\pi} \int_{-\infty}^{\infty} S_y(\omega) d\omega. \tag{5.7}$$

These equations are very important relationships used in this stochastic noise model. Based on the relationships above, we will model the propagation and contribution of each noise source in the following sections.

5.2 Positioning Noise Modeling in the X Axis

5.2.1 Noise Propagation Model

Figure 5-1 shows the noise propagation model within the control loop for X-axis motion. W_d is the disturbance to the controller output. It includes disturbance from floor vibration and noise from D/A quantization. V_n is the noise from sensing feedback. It includes sensor noise, A/D quantization and A/D electronics noise. For measurement in X axis and Y axis, there is no A/D quantization and A/D electronics noise because the laser electronic board brings digital signal directly to the DSP so that no A/D converter is needed in these two axes.
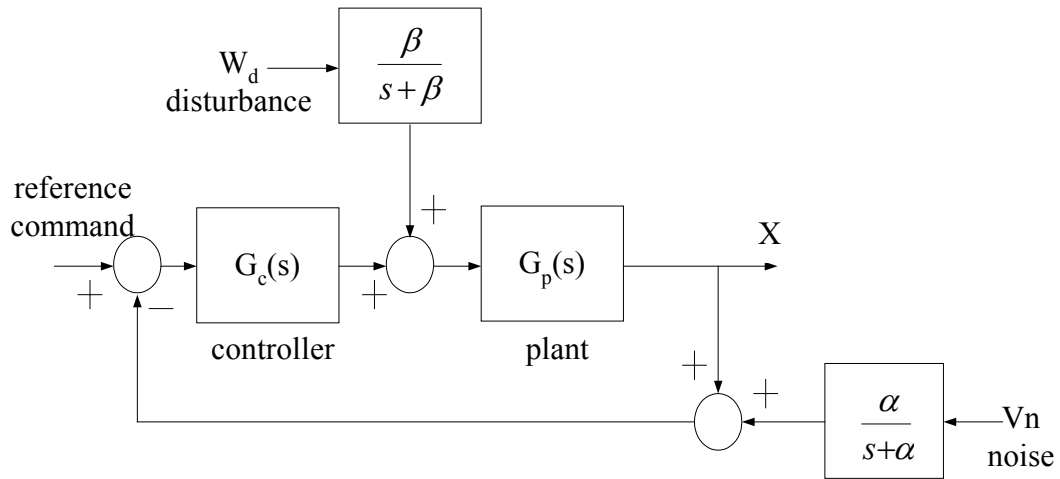
Figure 5-1: Noise/disturbance propagation model

We assume that all the noises in this model are white gaussian noises which have a constant spectral density. Each white gaussian noise passes through a low-pass filter before it enters the control loop. The cutoff frequencies α, β of the filters are determined empirically.

5.2.2 Propagation of Sensor Noise and Disturbance Forces

To get the effects of each noise source, the relationship between the original noise and its contribution to the platen positioning noise need to be obtained by transforming our control loop transfer function.

We first build the relationship between sensor noise $V_n(s)$ and final positioning noise $X(s)$ in s domain. The reference command and force disturbance $W_d(s)$ in Figure 5-1 are set to zero. By doing some transformation to the model in Figure 5-1, we get

$$\frac{X(s)}{V_n(s)} = \frac{G_c(s)G_p(s)}{1+G_c(s)G_p(s)}\frac{\alpha}{s+\alpha} \tag{5.8}$$

where $G_c(s)$ is the controller and $G_p(s)$ is the plant, modeled as

$$G_p(s) = \frac{1}{Ms^2} \tag{5.9}$$

with M as the mass. Then (5.8) becomes,

$$\frac{X(s)}{V_n(s)} = \frac{\dfrac{-\alpha G_c(s)}{Ms^2(s+\alpha)}}{1+\dfrac{G_c(s)}{Ms^2}} \tag{5.10}$$

which can be simplified to,

$$\frac{X(s)}{V_n(s)} = \frac{-\alpha G_c(s)/M}{(s+\alpha)(s^2+G_c(s)/M)}. \tag{5.11}$$

By finding the spectral densities to (5.11) and applying (5.6), we get the following relationship

$$S_x(\omega) = \left|\frac{-\alpha G_c(j\omega)/M}{(j\omega+\alpha)((j\omega)^2+G_c(j\omega)/M)}\right|^2 S_n(\omega). \tag{5.12}$$

As discussed in Section 5.2, the inverse Fourier transform of $S_x(\omega)$ is the autocorrelation of the position error. And when $\tau = 0$, autocorrelation is the same as mean squared value of the waveform. If the signal has zero mean, the mean square value and the variance are identical.

By integrating $S_x(\omega)$ over all frequencies, we get the noise variance. Finally, we have

$$\sigma^2_{x,n} = \frac{S_n}{2\pi} \int_{-\infty}^{\infty} \left| \frac{-\alpha G_c(j\omega)/M}{(j\omega + \alpha)((j\omega)^2 + G_c(j\omega)/M)} \right|^2 d\omega. \tag{5.13}$$

This is the equation that is used to determine the contribution of the sensor noise to the final position variance of the platen in X-axis motion.

Next, we build the relationship between force disturbance $W_d(s)$ and the final positioning noise $X(s)$. Similarly as for sensor noise, we can get the transfer function between $W_d(s)$ and $X(s)$,

$$\frac{X(s)}{W_d(s)} = \frac{\beta/M}{(s+\beta)(s^2 + G_c(s)/M)} \tag{5.14}$$

Then the corresponding relationship between the spectral densities is

$$S_x(\omega) = \left| \frac{\beta/M}{(j\omega + \beta)((j\omega)^2 + G_c(j\omega)/M)} \right|^2 S_w(\omega). \tag{5.15}$$

Finally, we have

$$\sigma^2_{x,w} = \frac{S_w}{2\pi} \int_{-\infty}^{\infty} \left| \frac{\beta/M}{(j\omega + \beta)((j\omega)^2 + G_c(j\omega)/M)} \right|^2 d\omega \tag{5.16}$$

which is the equation to determine the contribution of force disturbance to the final positioning variance in the X axis.

5.2.3 Sensor Noise from Laser Interferometer

The laser electronics board in laser interferometer system transfers measurement data to the DSP through VME bus. No A/D converter is needed in this case. Defining Δ to be the resolution of our laser interferometer system, the variance of the noise is given by

$$\sigma^2_{laser} = \frac{\Delta^2}{12} = \frac{0.6^2}{12} = 0.03\,\text{nm}^2 \tag{5.17}$$

where Δ=0.6 nm from the manual of Agilent's laser axis board.

Since the variance above is a discrete-time variance. We need to convert it to a continuous-time spectral density. With the assumption of white noise, the discrete-time spectral density is equal to the discrete time variance 0.03 nm^2. Then we convert this dicrete-time spectral density to continuous-time spectral density by doing unit conversion,

$$\left(\frac{0.03\,\text{nm}^2}{\text{rad/sample}}\right)\left(\frac{s}{5000\,\text{samples}}\right)\left(\frac{2\pi\,\text{rad/s}}{\text{Hz}}\right)\left(\frac{1\,\text{m}}{10^9\,\text{nm}}\right)^2 = 3.77\times10^{-23}\,\text{m}^2/\text{Hz} \tag{5.18}$$

So we get the spectral density for sensor noise from laser interferometer $S_{laser} = 3.77\times10^{-23}\,\text{m}^2/\text{Hz}$.

5.2.4 D/A Converter Quantization Noise

D/A quantization noise is one of disturbance forces presented in W_d. We first find the relationship between the actuator force and the output voltage. As mentioned in

Section 2-3, the theoretical relationship between force and current for horizontal actuator is

$$F = 1.678\ i \qquad (5.19)$$

With the gain of 0.5 from the power amplifier, we have

$$F = 0.839\ v \qquad (5.20)$$

If we define the voltage quantization as Δv, then the variance of the force is given by

$$\sigma^2_{D/A} = \frac{0.839^2\ \Delta v^2}{12} = 1.37 \times 10^{-9}\ \text{N}^2 \qquad (5.21)$$

where $\Delta v = \dfrac{10}{2^{16}} = 1.53 \times 10^{-4}$ V with 16-bit D/A and ± 5 V output range.

The discrete-time spectral density is equal to the variance, i.e. $1.37 \times 10^{-9}\ \text{N}^2/(\text{rad/sample})$. By doing the unit conversion, we get the continuous-time spectral density due to D/A quantization,

$$S_{D/A} = \left(\frac{1.37 \times 10^{-9}\ \text{N}^2}{\text{rad/sample}} \right) \left(\frac{s}{5000\ \text{samples}} \right) \left(\frac{2\pi\ \text{rad/s}}{\text{Hz}} \right) = 1.72 \times 10^{-12}\ \text{N}^2/\text{Hz} \qquad (5.22)$$

5.2.5 Horizontal Floor Force Disturbance

The noise from the optical table can be measured by using accelerometer. PCB[14] seismic accelerometer[15] along with an Agilent 54624A storage oscilloscope are used to measure and record the data.
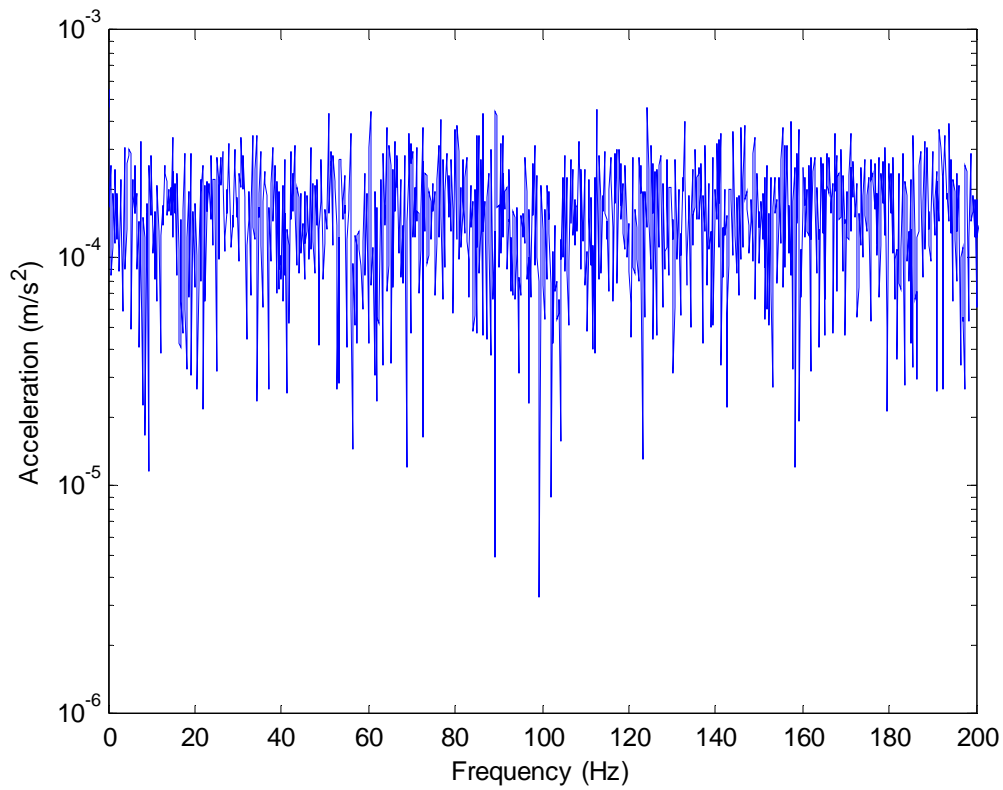
Figure 5-2: FFT of disturbance force on optical table in the X axis

---

[14] PCB Piezotronics, Inc. 3425 Walden Ave., Depew, NY 14043-2495

[15] Model No. 393C, Serial No. 9703, Sensitivity = 946 mV/g

Figure 5-2 shows the FFT of vibration on the optical table in the X axis. The spectral density of the disturbance force from optical table is shown in Figure 5-3. We model the disturbance force as a white noise with the power spectral density $S_v = 2.0 \times 10^{-12}$ N²/Hz.

5.2.6 Final Noise in the X Axis

Now, with spectral densities of all the noise components, we can get the contribution of each noise source to the final noise. As shown in Section 5.2.2, the relationship between the sensor noise and the final noise in the X axis is:
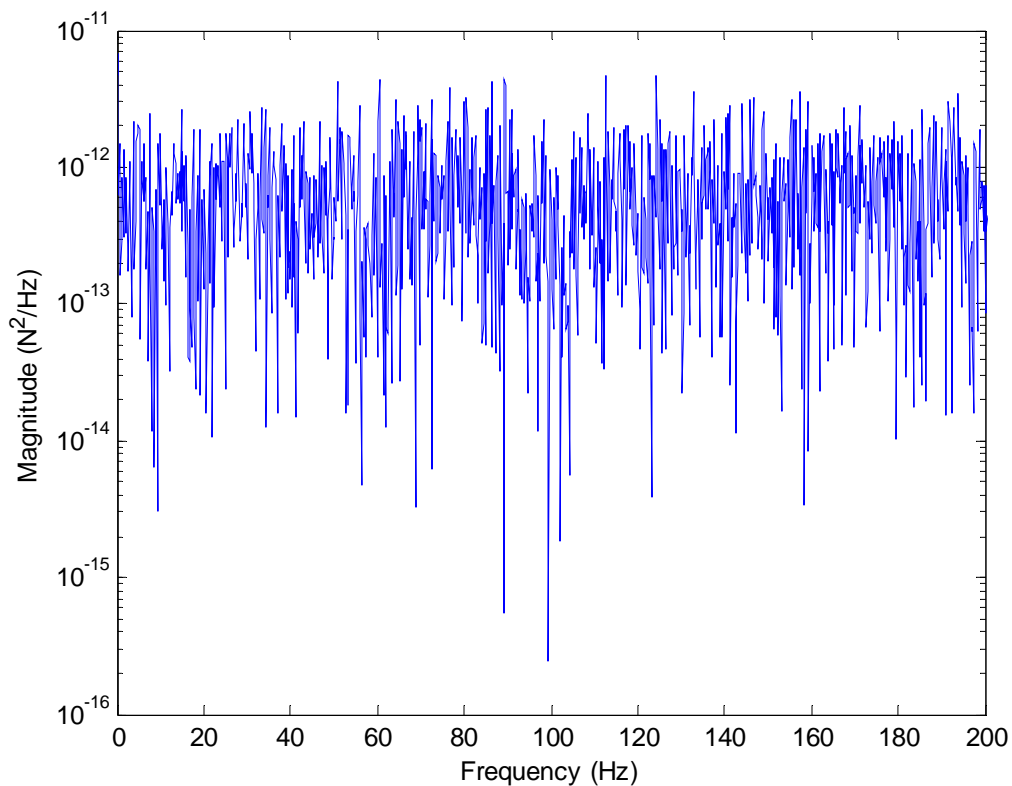
Figure 5-3: Power spectral density of disturbance force in the X axis

$$\sigma^2_{x,n} = \frac{S_n}{2\pi} \int\limits_{-\infty}^{\infty} \left| \frac{-\alpha G_c(j\omega)/M}{(j\omega + \alpha)((j\omega)^2 + G_c(j\omega)/M)} \right|^2 d\omega$$

where $S_n = S_{laser} = 3.77 \times 10^{-23}$ m^2/Hz. The value of α is chosen to 500 Hz which is an order of magnitude above the controller bandwidth.

And the relationship between the disturbance force and the final noise in X axis is:

$$\sigma^2_{x,w} = \frac{S_w}{2\pi} \int\limits_{-\infty}^{\infty} \left| \frac{\beta/M}{(j\omega + \beta)((j\omega)^2 + G_c(j\omega)/M)} \right|^2 d\omega.$$

where $S_w = S_{D/A} + S_v = 3.72 \times 10^{12}$ N^2/Hz and β is also chosen to 500 Hz which is an order of magnitude above the controller bandwidth.

By using MathCad to calculate the above integration, we get $\sigma^2_{x,n} = 2.379 \times 10^2 S_n$ and $\sigma^2_{x,w} = 9.527 \times 10^{-7} S_w$. Substituting the value of S_n and S_w, we get $\sigma^2_{x,n} = 8.97 \times 10^{-21}$ m^2 and $\sigma^2_{x,w} = 3.54 \times 10^{-18}$ m^2. Then the final noise is

$$\sigma^2_z = \sigma^2_n + \sigma^2_w = 3.55 \times 10^{-18} \text{ m}^2 \qquad . \tag{5.23}$$

which corresponds to a peak-to-peak (6σ) value of 11.30 nm. Because of the coupling from vertical motion, our experiment gives about 15-nm peak-to-peak noise which is a little higher than this predicted value. Figure 5-4 shows the contribution of each noise source to the final positioning noise in the X axis.
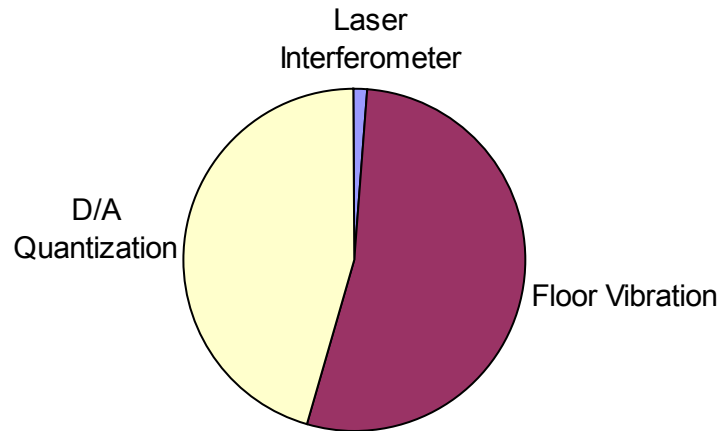
$$\sigma_x^2 = 3.55 \ \text{nm}^2$$

Figure 5-4: Pie chart showing noise contribution of each noise source

5.3 Positioning Noise Model in the Z Axis

We use the same way shown above to do the noise analysis in the Z axis. The same model is used as shown in Figure 5-1. In the Z axis, the disturbance force W_d includes disturbance from floor vibration and noise from D/A quantization. And the sensor noise V_n includes electronics noise from capacitance sensor, A/D quantization and A/D electronics noise.

We can use the same equation derived in Section 5.2.2. The relationship between the spectral density of sensor noise S_n and the positioning noise S_z is given by

$$S_z(\omega) = \left| \frac{-\alpha G_c(j\omega)/M}{(j\omega + \alpha)((j\omega)^2 + G_c(j\omega)/M)} \right|^2 S_n(\omega). \qquad (5.24)$$

And we have

$$\sigma_{z,n}^2 = \frac{S_n}{2\pi} \int_{-\infty}^{\infty} \left| \frac{-\alpha G_c(j\omega)/M}{(j\omega + \alpha)((j\omega)^2 + G_c(j\omega)/M)} \right|^2 d\omega \qquad (5.25)$$

which gives the contribution of the sensor noise to the final position variance in Z-axis motion.

Similarly, we can get the relationship between the spectral densities of disturbance force and final positioning noise as

$$S_z(\omega) = \left| \frac{\beta/M}{(j\omega + \beta)((j\omega)^2 + G_c(j\omega)/M)} \right|^2 S_w(\omega). \qquad (5.26)$$

Then the contribution of force disturbance to the final positioning variance in Z axis is

$$\sigma_{z,w}^2 = \frac{S_w}{2\pi} \int_{-\infty}^{\infty} \left| \frac{\beta/M}{(j\omega + \beta)((j\omega)^2 + G_c(j\omega)/M)} \right|^2 d\omega. \qquad (5.27)$$

5.3.1 A/D Quantization

The A/D converters in Pentek's 6102 board has 16-bit resolution to represent the sensor range of 500 μm. This leads to a least-significant bit of 7.629 nm (500 μm/2^{16}).

The quantization noise is modeled as being uniformly distributed between any two consecutive discrete values. We define Δ to be the minimum resolution of the quantizer. Then the variance of the noise is given by

$$\sigma^2_{A/D\ quantization} = \frac{\Delta^2}{12} = 4.851\ \text{nm}^2 \tag{5.28}$$

where $\Delta = 7.629$ nm.

If signals are assumed to be zero mean white noise, the autocorrelation of the signal is same as the variance. The autocorrelation of a waveform is equal to the area under the spectral density over the bounds of $\pm\pi$ rad/sample, divided by 2π. Therefore, the discrete time spectral density is simply 4.851 nm^2/(rad/sample). Then we transfer this spectral density from digital to continuous signal:

$$\left(\frac{4.851\ \text{nm}^2}{\text{rad}/\text{sample}}\right)\left(\frac{\text{s}}{5000\ \text{samples}}\right)\left(\frac{2\pi\ \text{rad}/\text{s}}{\text{Hz}}\right)\left(\frac{1\ \text{m}}{10^9\ \text{nm}}\right)^2 = 6.09\times10^{-21}\,\text{m}^2/\text{Hz} \tag{5.29}$$

This method gives a spectral density for the A/D converter quantization noise of $S_{A/D\ quant} = 6.09 \times 10^{-21}$ m^2/Hz.

5.3.2 A/D Electronics Noise

The A/D converter electronics noise is added into the noise of the measurement signals from the capacitance sensors. To measure this electronics noise, we shorted the input from A/D input channel on Pentek's 6102. The reading from A/D converter was recorded by the DSP and saved into hard disk of the PC. Ideally the reading should be exactly zero counts for all the time. But because of the electronics noise the reading becomes quite noisy. Figure 5-5 shows a histogram of the data taken from this A/D converter. The converter noise shown here is normally distributed with a standard deviation of 4.958 counts with an offset of −10.367 counts. Considering the conversion factor of 0.15 mV/count from the A/D channel and 25 nm/mV from the capacitance sensors, this offset corresponds to −38.876 nm and the standard deviation of noise is

18.593 nm. The discrete-time variance of the waveform is equal to 345.70 nm^2/(rad/sample). Again, this discrete time spectral density need to be transformed to its continuous time equivalent. We find that

$$S_{A/D\ elec} = \left(\frac{345.70\ nm^2}{rad/sample} \right) \left(\frac{2\pi\ rad/sec}{Hz} \right) \left(\frac{s}{5000\ samples} \right) \left(\frac{1\ m}{10^9\ nm} \right)^2 = 4.34 \times 10^{-19}\ m^2/Hz \quad (5.30)$$

which is the continuous spectral density for the A/D electronics noise.
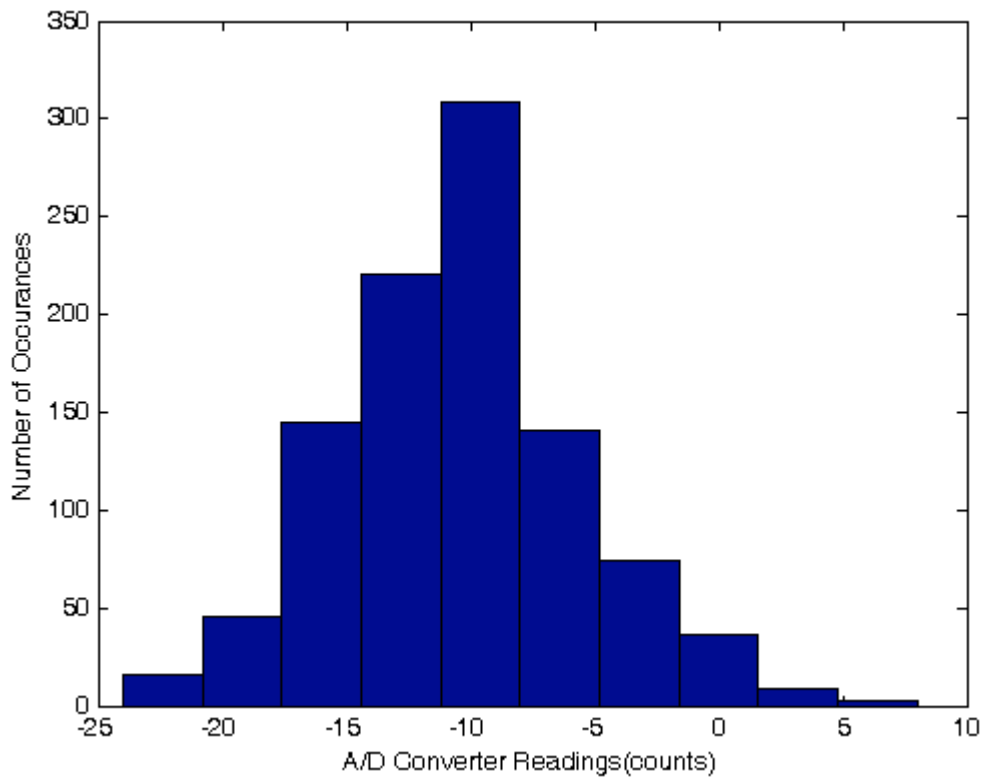
Figure 5-5: Histogram of the reading from A/D converter in 0.2 second

5.3.3 Capacitance Sensor Noise

By keeping the platen still, we can measure the noise from the capacitance sensor by using Agilent 54624A storage oscilloscope. The noise standard deviation is experimentally found at round 15.1 nm which corresponds to a position variance of 228.01 nm^2. By inspecting the data, we assume the measured probe spectral density is bandlimited by a bandwidth of 500 Hz corresponding to the sampling rate of our experiment to capacitance sensors. Then its spectral density and the position variance are related through

$$\sigma^2_{prob} = \frac{S_{prob}}{2\pi} \int_{-\infty}^{\infty} \frac{(100 \times 2\pi)^2}{\omega^2 + (100 \times 2\pi)^2} d\omega.$$

(5.31)

From the above value, we found the spectral density of the capacitance sensor electrical noise S_{prob} is 7.25×10^{-19} m^2/Hz.
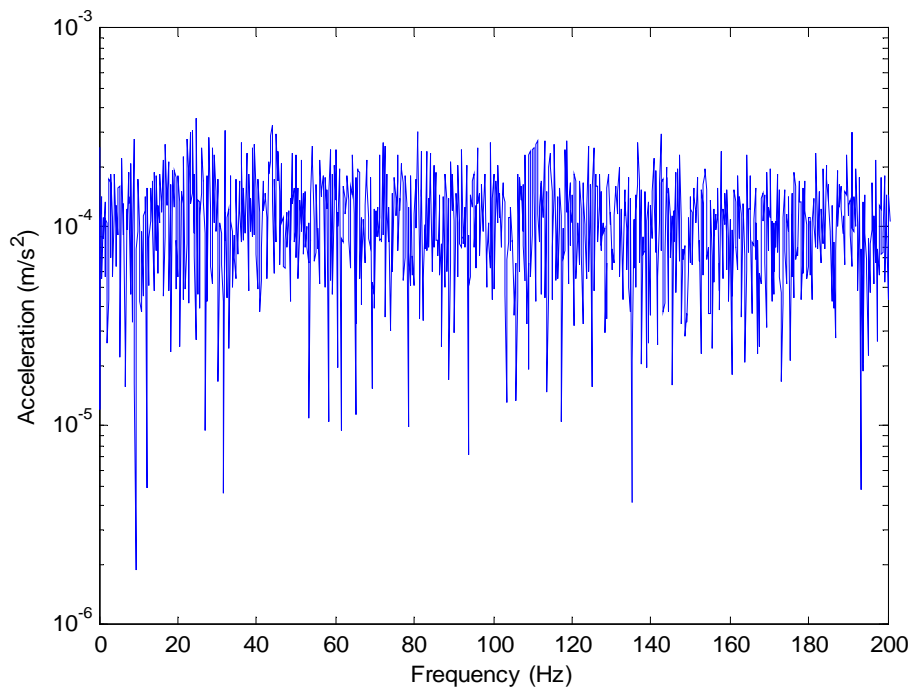
Figure 5-6: FFT of vertical vibration on top of optical table
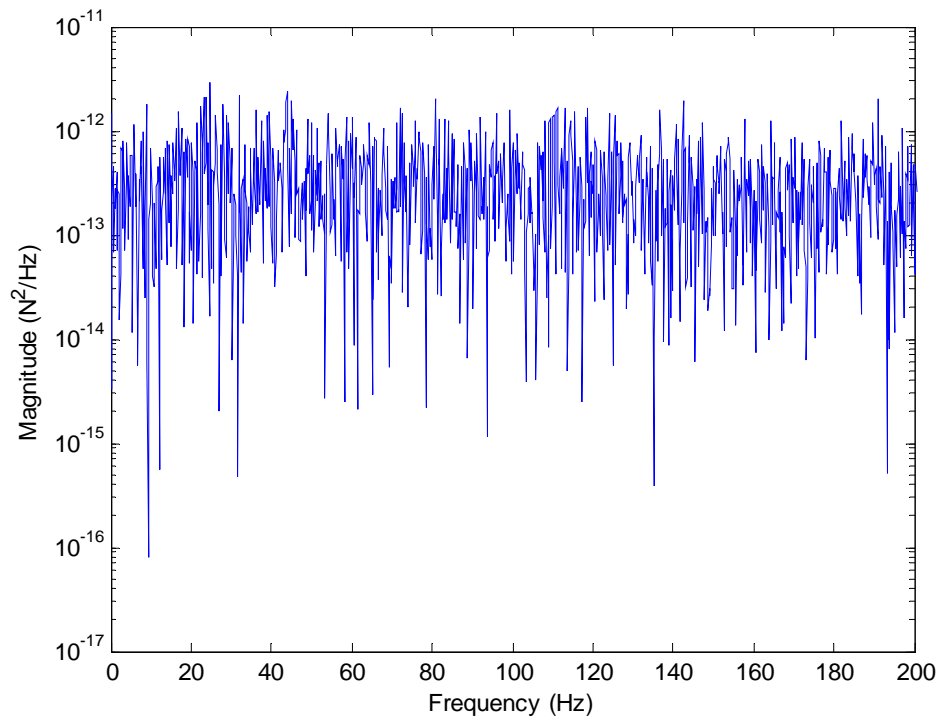
Figure 5-7: Power spectral density of vertical disturbance force

5.3.4 Vertical Floor Disturbance

Again, the noise from the optical table in vertical direction can be measured by using PCB seismic accelerometer along with an Agilent 54624A oscilloscope. Figure 5-6 shows the FFT of vibration on the optical table in vertical direction.

As we did to horizontal noise, we model this disturbance force as a white noise. The spectral density of the disturbance force is shown in Figure 5-7. The power spectral density of this disturbance force from the floor S_v is approximately 1.0×10^{-12} N^2/Hz.

5.3.5 Final Noise in the Z Axis

We use the same way as the previous analysis to get the contribution of each noise source in the Z axis. From equation (5.13), the relationship between the sensor noise and the final noise is:

$$\sigma_{z,n}^2 = \frac{S_n}{2\pi} \int_{-\infty}^{\infty} \left| \frac{-\alpha G_c(j\omega)/M}{(j\omega + \alpha)((j\omega)^2 + G_c(j\omega)/M)} \right|^2 d\omega \tag{5.32}$$

where $S_n = S_{prob} + S_{A/Dquant} + S_{A/Delec} = 1.17 \times 10^{-18}$ m^2/Hz. The value of α is chosen to 500 Hz which is an order of magnitude above the controller bandwidth.

And the relationship between the disturbance force to the final noise in the Z axis is:

$$\sigma_{z,w}^2 = \frac{S_w}{2\pi} \int_{-\infty}^{\infty} \left| \frac{\beta/M}{(j\omega + \beta)((j\omega)^2 + G_c(j\omega)/M)} \right|^2 d\omega. \tag{5.33}$$

where $S_w = S_{D/A} + S_v = 2.72 \times 10^{-12}$ N^2/Hz and β is also chosen to 500 Hz which is an order of magnitude above the controller bandwidth. The value of $S_{D/A}$ is the same as the value in the X axis which is 1.72×10^{-12} N^2/Hz.

Again, by using MathCad, we get $\sigma_{z,n}^2 = 2.379 \times 10^2 S_n$ and $\sigma_{z,w}^2 = 9.527 \times 10^{-7} S_w$. Substituting the value of S_n and S_w, we get $\sigma_{z,n}^2 = 2.78 \times 10^{-16}$ m^2 and $\sigma_{z,w}^2 = 2.59 \times 10^{-18}$ m^2. Then the final noise is

$$\sigma_z^2 = \sigma_n^2 + \sigma_w^2 = 2.81 \times 10^{-16} \text{ m}^2 \tag{5.34}$$

which corresponds to a peak-to-peak (6σ) value of 100.6 nm. Experimentally, we get around 150-nm peak-to-peak noise in the Z axis as shown in Chapter IV. The difference between predicted value and experimental value may come from the error on our dynamic model, the coupling between vertical and horizontal motion and some unpredictable experiment condition such as the disturbance from electrical wires. Figure 5-8 shows the contribution of each noise source to positioning noise in the Z axis.

$$\sigma_z^2 = 281 \ \mathrm{nm}^2$$
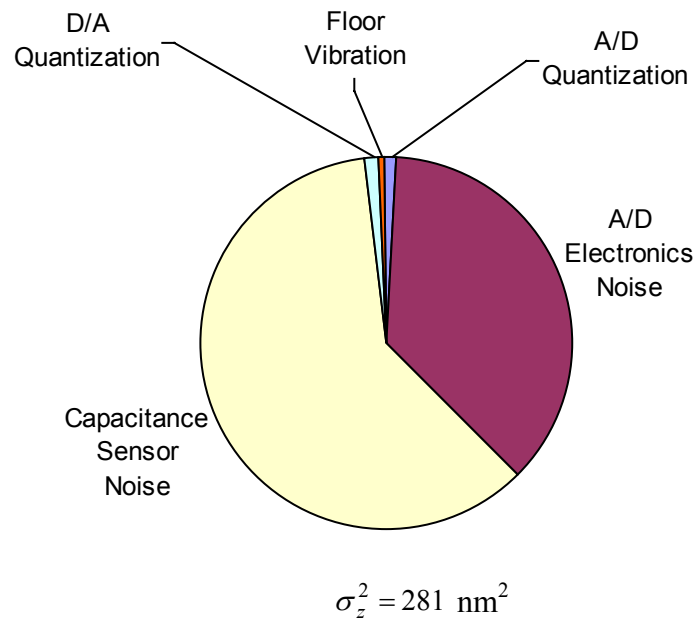
Figure 5-8: Pie chart showing noise contribution of each noise source

CHAPTER VI
CONCLUSIONS

This final chapter contains the discussion about the achieved objectives of the project. It also suggests some further improvement for our maglev device.

6.1 Conclusions

This thesis presents a design of a novel 6-DOF maglev device with nanopositioning capability. This maglev device has the application in semiconductor manufacturing, nanomanipulation, robotics, telesurgery, etc. Since no lubricant is needed, this device is suitable for clean-room or vacuum environment in IC industry. Moreover, the simplicity of the mechanical structure without friction in the mechanical system can reduce the manufacturing cost and improve the system dynamic performance. For example, the lack of backlash in the maglev system increases the positioning accuracy. The single-moving part contributes to the high natural frequency of the mechanical structure.

As presented in this thesis, the single-moving stage and other supporting parts have been successfully designed and fabricated. Six single-axis maglev actuators were developed and precisely assembled to satisfy the force requirement of the 6-DOF motion. The characteristics of the mechanical design include (1) a compact structure with actuators close to the center of mass, which effectively reduces the coupling between the vertical motion and the lateral motion, (2) light weight (only 0.2126 kg of the whole moving part) which result in a low power consumption in the actuators, and (3) utilization of the damping layer to reduce the system resonance. With the maximum current of 2.5 A in each actuator, the device has the capability of 1-g acceleration in vertical motion and 3.5-g acceleration in lateral motion.

The electrical system including the VME PC, DSP, A/D and D/A board, power amplifers, and anti-aliasing filters was built. The sampling rate was 5 kHz. Capacitance sensors and laser interferometers were arranged to precisely measure all the six-axis motion of the maglev stage. Software was successfully developed to realize the DSP-based real-time control, VME bus communications and user interface. The software has a friendly user-interface developed in Windows environment and can achieve the tasks of byte-swapping and data format conversion.

A simple dynamic model was used for the control system design. Force allocation and sensor equations were built to generate the 6-axis force and measure the 6-axis motion of the device. Six independent lead-lag controllers were designed and implemented on the DSP. The control loop was closed at 48 Hz. Tests were performed to examine the performance of our device. Important experimental achievements include 2.5-nm rms position noise in the X and Y axis and 25-nm rms position noise in the Z axis. The test results also showed nice step responses in all six axes. As a conclusion, this maglev device has achieved the capability of nanopositioning in 6-DOF motion.

Because the noise performance is very important for nanopositioning, a further analysis of the noise propagation within the electromechanical system was presented at the last chapter of this thesis. A stochastic model for the random signal was used to predict the contributions by each potential noise source to our final positioning noise. The analysis showed the major noise component in the lateral motion was the floor vibration and the major noise components in the vertical motion were the capacitance sensor noise and A/D electronic noise. As a result, for further improvement we need isolate the floor vibration more effectively in lateral axes and choose quieter electronics, i.e. A/D converters and sensors in vertical axes.

6.2 Suggestions for Future Work

There is still much work to be done after the initial setup and testing presented in this thesis. Some suggestions for further work are:

- Digital notch filters should be implemented to get rid of the noise in a particular frequency such as the 18-Hz floor vibration noise as shown in our test results.

- A new precise dynamic model needs to be developed for the maglev device. It will model the platen as a mass-spring-dashpot, and will treat the magnetic force as a nonlinear force as a function of position. An improved dynamic model can reduce the coupling between the vertical motion and the horizontal motion.

- Several advanced control methods such as multivariable control, and time-optimal control can be designed and implemented for the 6-DOF device. This maglev device will be a good example for the research of modern control theory.

- A contribution to the nanotechnology, e.g. nanomanipulation is the final objective of this research. A scanner or a micromanipulator can be installed on the moving part of this device and the nanofabrication and nanomaniplulation can be realized with the help of an AFM or a 3D digital inspection measurement system. To achieve this objective, further tests such as the load, velocity, and acceleration capabillities need to be completed.

REFERENCES

[1] "Nanotechnology Definition," *Nanoscale Science, Engineering and Technology* (NSET), Online: www.nano.gov, Feb. 2000.

[2] M. Sitti, "Survey of Nanomanipulation Systems," in *IEEE-NANO 2001*, Maui, HI, Aug. 2001, pp. 75−80.

[3] M. Sitti and H. Hashimoto*,* "Controlled Pushing of Nanoparticles: Modeling and Experiments," *IEEE/ASME Transactions on Mechatronics*, vol. 5, no. 2, pp. 199−211, Jun. 2000.

[4] C. Bauer, A. Bugacov, B. E. Koel, A. Madhukar, N. Montoya, T. R. Ramachandran, A. A. G. Requicha, R. Resch, and P. Will, "Nanoparticle Manipulation by Mechanical Pushing: Underlying Phenomena and Real-Time Monitoring," *Nanotechnology*, vol. 9, pp. 360−364, Dec. 1999.

[5] R. M. Talor II, "The Nanomanipulator: A Virtual-Reality Interface to a Scanning Tunneling Microscope," Ph.D. Dissertation, University of North Carolina at Chapel Hill, May 1994.

[6] M. F. Yu, M. J. Dyer, H. W. Rohrs, X. K. Lu, K. D. Ausman, J. V. Her, and R. S. Ruoff, "Three-Dimensional Manipulation of Carbon Nanotubes under a Scanning Electron Microscope," *Nanotechnology*, vol. 10, pp. 244−252, Sept. 1999.

[7] A. A. G. Requicha, S. Meltzer, F. P. Terán Arce, J. H. Makaliwe, H. Sikén, S. Hsieh, D. Lewis, B. E. Koel, and M. E. Thompson, "Manipulation of Nanoscale Components with the AFM: Principles and Applications," in *IEEE-NANO 2001*, Maui, HI, Aug. 2001, pp. 81−86.

[8] Zyvex Corporation, "Molecular Nanotechnology," Richardson, TX, Online: www.zyvex.com, Jan. 2000.

[9] Y. Egshira, K. Kosaka, S. Takada, T. Iwabuchi, T. Baba, S. Moriyama, T. Harada, K. Nagamoto, A. Nakada, H. Kubota, and T. Ohmi, "0.69 nm Resolution Ultrasonic Motor for Large Stroke Precision Stage," in *IEEE-NANO 2001*, Maui, HI, Aug. 2001, pp. 397−402.

[10] "IC Probing Stage: Special Design for IC Test System Retrofit," Heason Technologies Group Limited, Chichester, West Sussex, United Kingdom, Online: http://www.heason.com/, 2001.

[11] "Magnetic Levitation" Encyclopedia.com, Online: www.encyclopedia.com, 2002.

[12] R.G. Rhodes and B.E. Mulhall, *Magnetic Levitation for Rail Transport.* Oxford, United Kingdom: Oxford University Press, 1981.

[13] J. W. Fischer, "Maglev as a High Speed Ground Transportation Alternative: Background and Developments," Congressional Research Service Reports RS20613, Online: http://www.ncseonline.org/NLE/CRS/, Jun. 2000

[14] A. E. Hajjaji and M. Ouladsine, "Modeling and Nonlinear Control of Magnetic Levitation Systems," *IEEE Transactions on Industrial Electronics*, vol. 48, pp. 831−838, Aug. 2001.

[15] R. L. Hollis and S. E. Salcudean, "Lorentz Levitation Technology: A New Approach to Fine Motion Robotics, Teleoperation, Haptic Interface, and Vibration Isolation," in *Proc. of 5th International Symposium on Robotics Research*, Hidden Valley, PA, Oct. 1993, pp. 1−18.

[16] W.-J. Kim, "High-Precision Planar Magnetic Levitation," Ph.D. Dissertation, Massachusetts Institute of Technology, Cambridge, MA, Jun. 1997.

[17] W.-J. Kim and D. L. Trumper, "High-Precision Magnetic Levitation Stage for Photolithography," *Precision Engineering*, vol. 22, pp. 66−77, Apr. 1998.

[18] X. Shan, S.-K. Kuo, J. Zhang, and C.-H. Menq, "Ultra Precision Motion Control of a Multiple Degrees of Freedom Magnetic Suspension Stage," *IEEE/ASME Transactions on Mechatronics*, vol. 7, pp. 67−78, Mar. 2002.

[19] M. L. Holmes, "Analysis and Design of a Magnetically Suspended Precision Motion Control Stage," M.S. Thesis, University of North Carolina at Charlotte, Jun. 1994.

[20] M. L. Holmes, R. Hocken, and D. Trumper, "The Long Range Scanning Stage: A Novel Platform for Scanned Probe Microscopy," *Precision Engineering*, vol. 24, no. 3, pp. 191−209, Jul. 2000.

[21] E. H. Brandt, "Levitation in Physics," *Science*, vol. 243, pp. 349−355, Jan. 1989.

[22] W.-J. Kim, "Method and Apparatus for Magnetically Generating Motion with High Precision," US Patent and Trademark Office (PTO), Patent Application Serial No. 10/232,626, Aug. 30, 2002.

[23] W.-J. Kim, "MRI: Development of a Six-Axis, Magnetically Levitated Instrument for Nanoscale Science and Engineering," NSF, Arlington, VA, Grant Number: CMS-0116642, Sept. 2001−Aug. 2004.

[24] H. Maheshwari, "Design and Fabrication of a Maglev Linear Actuator Capable of Nanopositioning," M.S. Thesis, Texas A&M University, College Station, TX, Dec. 2002.

[25] S. Heath, *VMEbus-A Practical Companion*. Oxford, United Kingdom: Butterworth-Heinemann Ltd, 1993.

[26] W. D. Peterson, *The VMEbus Handbook Third Edition*, Scottsdale, AZ: VFEA International Trade Association, 1993.

[27] S. J. Ludwick, "Modeling and Control of a Six Degree of Freedom Magnetic/Fluidic Motion Control Stage," M.S. Thesis, Massachusetts Institute of Technology, Cambridge, 1996.

APPENDIX A
REAL-TIME CONTROL CODE

The real-time control code is processed by 320C40 digital signal processor. The function c_int01() is called every 200 μs by interrupt signal which is generated by channel D1 in the Pentek 6102 A/D, D/A converter board.

```c
#include "dsp.h"
void c_int01()
{
unsigned long D1reading;
long ADreading;
float z_mea;


tr_low();



D1reading=*(unsigned long )AD_FIFO_D1;   /* clear D1 channel for the next interrupt */


/* read laser interferometers  */
*(unsigned long int *)0xb0300003=0x0041;
raw_x_pos= (*(long int *)0xb0300048 << 16) & 0xffff0000;
raw_y1_pos = (*(long int *)0xb0310048 << 16) & 0xffff0000;
raw_y2_pos = (*(long int *)0xb0320048 << 16) & 0xffff0000;
tr_high();
raw_x_pos |= ((*(long int *)0xb0300048 >>16) & 0x0000ffff);
raw_y1_pos |= ((*(long int *)0xb0310048 >> 16) & 0x0000ffff);
raw_y2_pos |= ((*(long int *)0xb0320048 >> 16) & 0x0000ffff);
```

```c
x_pos=raw_x_pos*6.1815119987e-10;
y1_pos=raw_y1_pos*6.1815119987e-10;
y2_pos=raw_y2_pos*6.1815119987e-10;
tr_low();

/* read capacitance sensors */
ADreading=*(unsigned long int *)AD_FIFO_A1 & 0xffff;
if(ADreading & 0x8000)
ADreading = ADreading | 0xffff0000;
AD_A1=ADreading;
z_pos1=ADreading*7.629627369e-9+250e-6;


ADreading=*(unsigned long int *)AD_FIFO_B1 & 0xffff;
if(ADreading & 0x8000)
ADreading = ADreading | 0xffff0000;
z_pos2=ADreading*7.629627369e-9+250e-6;


ADreading=*(unsigned long int *)AD_FIFO_C1 & 0xffff;
if(ADreading & 0x8000)
ADreading = ADreading | 0xffff0000;
z_pos3=ADreading*7.629627369e-9+250e-6;


/* calculate the position of center of mass */
yr=y1_pos;
xr=-0.5774*y1_pos-1.1547*x_pos;
rr=18.1818*y2_pos;
zr=z_pos1*0.323352+z_pos2*0.411875+z_pos3*0.264773;
sr=z_pos1*-45.230449+z_pos2*14.963808+z_pos3*30.266641;
tr=z_pos2*-44.883303+z_pos3*44.883303;
```

```
/* controller */
if (controller_flag == 1)     /* if controller is enabled, process the controller */


{
er0x=xc-xr;
er0y=yc-yr;
er0r=rc-rr;
er0z=zc-zr;
er0s=sc-sr;
er0t=tc-tr;


u0z=1.7977*u1z-0.7977*u2z+67897*er0z-134117*er1z+66222*er2z;
u0s=1.7977*u1s-0.7977*u2s+42.4377*er0s-83.8272*er1s+41.3911*er2s;
u0t=1.7977*u1t-0.7977*u2t+39.0524*er0t-77.1402*er1t+38.0892*er2t;
u0x=1.7977*u1x-0.7977*u2x+67897*er0x-134117*er1x+66222*er2x;
u0y=1.7977*u1y-0.7977*u2y+67897*er0y-134117*er1y+66222*er2y;
u0r=1.7977*u1r-0.7977*u2r+75.329*er0r-148.79736*er1r+73.471*er2r;


/* get the output force from controller */
f1=u0z*0.333248+u0s*-10.495753+u0t*18.181818;
f2=u0z*0.348465+u0s*-10.499418+u0t*-18.181818;
f3=u0z*0.318287+u0s*20.995171;
f4=0.6705*u0x+0.0033*u0y+8.1619*u0r;
f5=-0.3295*u0x+0.5807*u0y+8.1619*u0r;
f6=-0.3295*u0x-0.5740*u0y+8.1619*u0r;


/* get the output current */
```

```
i1=f1*f2iv;
i2=f2*f2iv;
i3=f3*f2iv;
i4=f4*f2ih;
i5=f5*f2ih;
i6=f6*f2ih;


/* get the output value and set limits to ±5 V */
v1=i1*i2v;
if ((v1+vn1)>=5.0) v1=4.9-vn1;
if ((v1+vn1)<=-5.0) v1=-4.9-vn1;
v2=i2*i2v;
if ((v2+vn2)>=5.0) v2=4.9-vn2;
if ((v2+vn2)<=-5.0) v2=-4.9-vn2;
v3=i3*i2v;
if ((v3+vn3)>=5.0) v3=4.9-vn3;
if ((v3+vn3)<=-5.0) v3=-4.9-vn3;
v4=i4*i2v;
if (v4>=5) v4=5;
if (v4<=-5) v4=-5;
v5=i5*i2v;
if (v5>=5) v5=5;
if (v5<=-5) v5=-5;
v6=i6*i2v;
if (v6>=5) v6=5;
if (v6<=-5) v6=-5;


}
```

```
/* D/A output */
if(flag_d2a==1)        /* if D/A is enabled, output voltage */
{
*(unsigned   int  *)DA_FIFO_A1=(((unsigned   int)((v1+vn1)*6553.4))   <<16)   &
0xffff0000 ;
*(unsigned   int  *)DA_FIFO_B1=(((unsigned   int)((v2+vn2)*6553.4))   <<16)   &
0xffff0000;
*(unsigned   int  *)DA_FIFO_C1=(((unsigned   int)((v3+vn3)*6553.4))   <<16)   &
0xffff0000;
*(unsigned int *)DA_FIFO_A2=(((unsigned int)((prevA2+v5*hstart)*-6553.4)) <<16)
& 0xffff0000;
*(unsigned int *)DA_FIFO_B2=(((unsigned int)((prevB2+v6*hstart)*-6553.4)) <<16)
& 0xffff0000;
*(unsigned int *)DA_FIFO_C2=(((unsigned int)((prevC2+v4*hstart)*-6553.4)) <<16)
& 0xffff0000;
}


/* Set int_count for snap function */
if ((snap_begin==1) & (snap_enable==1))
{
int_count++;
}


/* save the old data for controller */
u2z=u1z;
u1z=u0z;
er2z=er1z;
er1z=er0z;
u2s=u1s;
```

```
u1s=u0s;
er2s=er1s;
er1s=er0s;
u2t=u1t;
u1t=u0t;
er2t=er1t;
er1t=er0t;
u2x=u1x;
u1x=u0x;
er2x=er1x;
er1x=er0x;
u2y=u1y;
u1y=u0y;
er2y=er1y;
er1y=er0y;
u2r=u1r;
u1r=u0r;
er2r=er1r;
er1r=er0r;

display=1;
/* clear pending interrupt */
MX_Int_Clr= 0x20000029;
*(unsigned int *)MX_Int_Clr=0x0;
}
```

APPENDIX B
ENGINEERING DRAWINGS

This appendix contains the detailed engineering drawings of some mechanical parts. The drawings were produced with Solidworks.
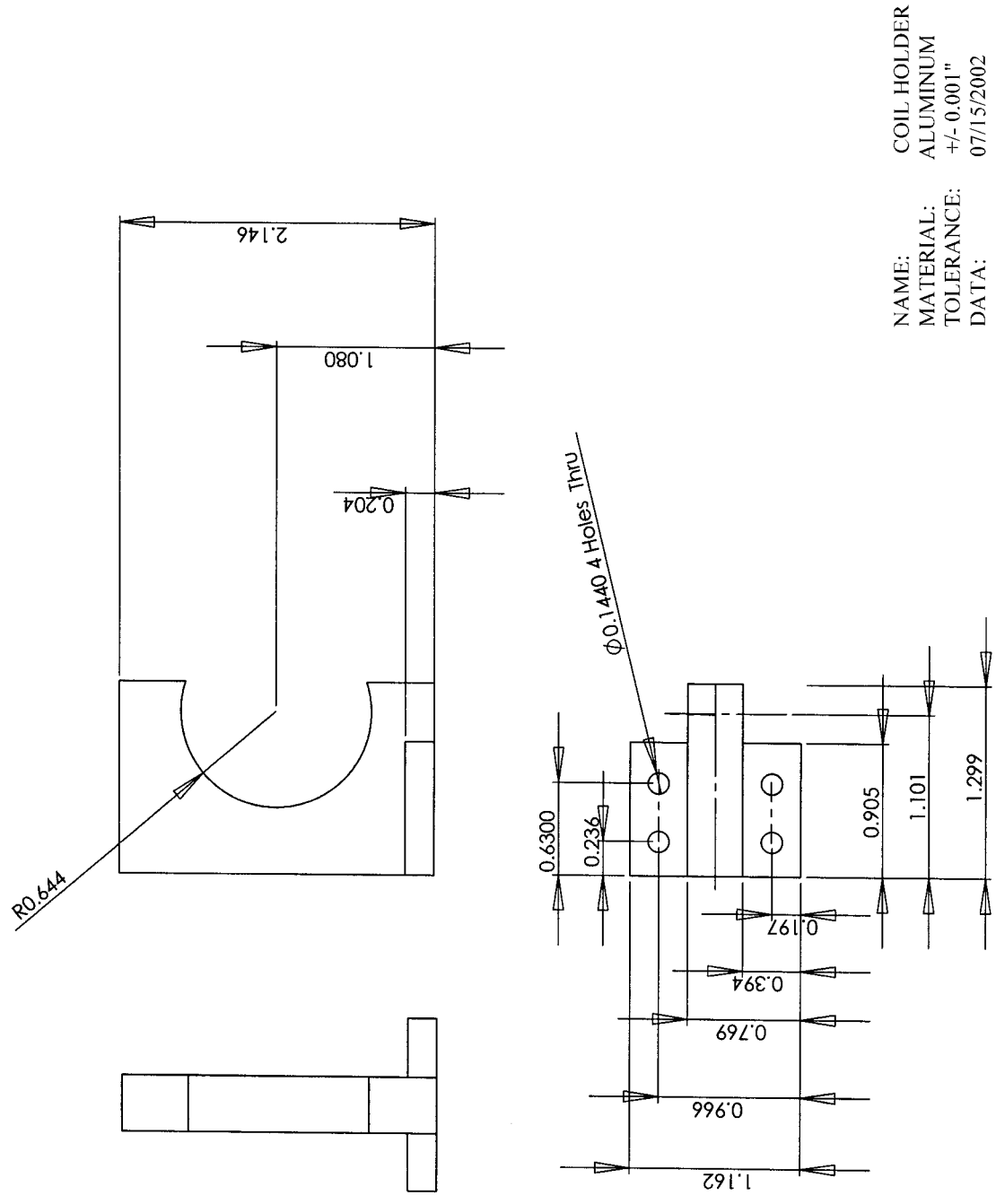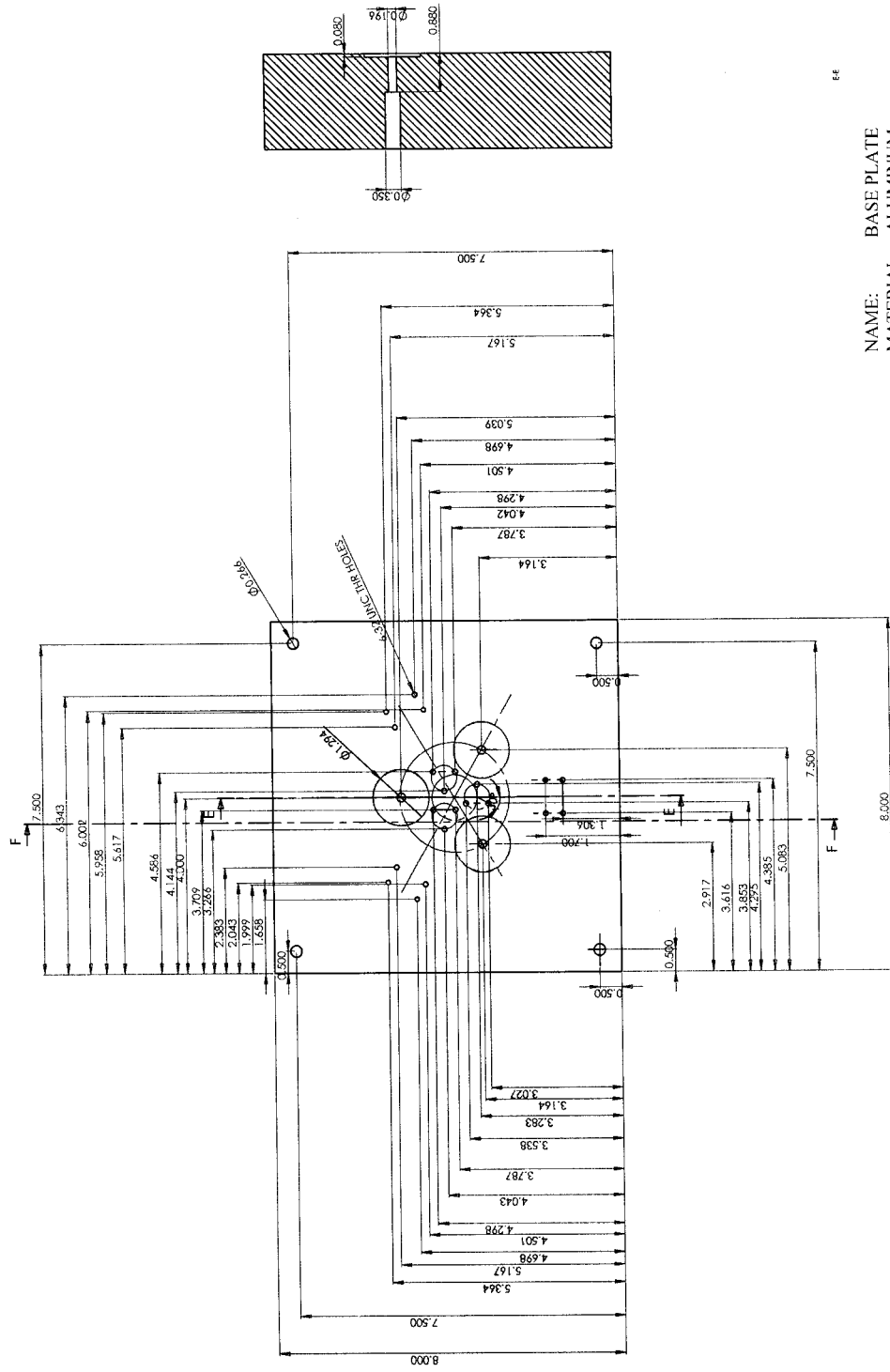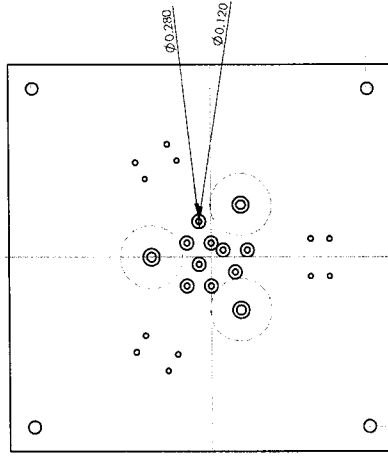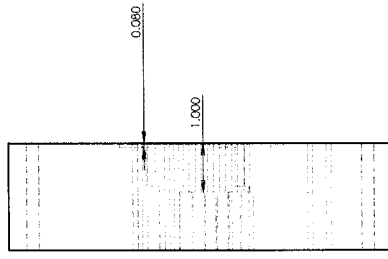
Figure B-1: Engineering drawing of platen

Figure B-2: Engineering drawing of coil holder

2.146

1.080

0.204

R0.644

Ø0.1440 4 Holes Thru

0.6300

0.236

0.905

1.101

1.299

0.197

0.394

0.769

0.966

1.162

NAME:　　　　　COIL HOLDER
MATERIAL:　　　ALUMINUM
TOLERANCE:　　+/- 0.001"
DATA:　　　　　07/15/2002

NAME: BASE PLATE
MATERIAL: ALUMINUM
TOLERANCE: +/- 0.001"
DATA: 09/13/2002

Figure B-3: Top view and section view of base plate

0.060

1.000

BASE PLATE
NAME:
MATERIAL: ALUMINUM
TOLERANCE: +/- 0.001"
DATA: 09/13/2002

Φ0.280

Φ0.120

Figure B-4: Bottom view and section view of base plate

VITA

The author, Jie Gu, was born on February 16, 1979 in Beijing, China. He graduated from Department of Precision Instruments, Tsinghua University, Beijing, China with the Bachelor of Engineering degree (Precision Instruments) in July 2001. After that, he began work on his master's degree in mechanical engineering at Texas A&M University in August 2001.

His permanent address is:

Hui Xin Li 216 # 903

Chaoyang District,

Beijing, 100029,

P.R.China

His e-mail address is:

gujie0216@hotmail.com.